

The Pennsylvania State University
The Graduate School
Department of Materials Science and Engineering

**PERFORMANCE OF PZT BASED MEMS DEVICES WITH INTEGRATED ZnO
ELECTRONICS**

A Dissertation in
Materials Science and Engineering
by
Margeaux Wallace

© 2016 Margeaux Wallace

Submitted in Partial Fulfillment
of the Requirements
for the Degree of
Doctor of Philosophy

May 2016

The dissertation of Margeaux Wallace was reviewed and approved* by the following:

Susan Trolier-McKinstry

Professor of Ceramic Science and Engineering and Electrical Engineering

Dissertation Adviser

Chair of Committee

Clive Randall

Professor of Materials Science and Engineering

Joshua Robinson

Assistant Professor of Materials Science and Engineering

Thomas N. Jackson

Robert E. Kirby Chair Professor of Electrical Engineering

Raegan Johnson-Wilke

Special Member

Sandia National Laboratory

Susan Sinnott

Professor of Materials Science and Engineering

Department Head, Materials Science and Engineering

*Signatures are on file in the Graduate School

ABSTRACT

This thesis describes routes to enable increased understanding and performance of lead zirconate titanate-based microelectromechanical systems (MEMS). Emphasis was placed on monolithic integration with interposer electronics, and in understanding the role of mechanical boundary conditions on the ferroelectric/ferroelastic response.

Co-processing of ZnO thin film transistors (TFTs) with $\text{Pb}(\text{Zr}_{0.52}\text{Ti}_{0.48})_{0.98}\text{Nb}_{0.02}\text{O}_3$ (PZT)-based piezoelectrics was investigated to assess whether interposer electronics on PZT can serve as a control scheme for large area arrays of sensors or actuators. ZnO TFT processing produced no measured changes in remanent polarization, dielectric constant, loss tangent, or aging rates. The TFT performance also did not degrade when fabricated on top of the PZT, the mobility (> 24 cm/Vs) remaining comparable to TFTs deposited on glass. To show ZnO array integration, a 5×5 array of PZT capacitors on glass was fabricated as a prototype for an adjustable X-ray mirror, where the ZnO TFT were used for row-column addressing of the actuators. $1.5 \mu\text{m}$ thick sputter deposited PZT on glass patterned with large area (cm^2) electrodes had a dielectric constant of >1200 , $\tan\delta \sim 2\%$ and an average remanent polarization $>23 \mu\text{C}/\text{cm}^2$. Photoreactive benzocyclobutene (BCB) electrically isolated the ZnO TFTs from the top electrodes of the piezoelectric. Flex cables were bonded to the wafer using anisotropic conductive film (ACF) to connect the gates (row control) and the drains (column control) in the TFT array to a control box. It was found that when actuating the PZT cells through the TFT array, the glass mirror experienced approximately $1.5 \mu\text{m}$ of deflection for a 10 V application.

Studies on ferroelectric/ferroelastic domain reorientation were also performed on $1.9 \mu\text{m}$ thick tetragonal $\{001\}$ oriented $\text{PbZr}_{0.3}\text{Ti}_{0.7}\text{O}_3$ films doped with 1% Mn. Different mechanical boundary constraints were investigated and domain reorientation was quantified through the

intensity changes in the 002/200 Bragg reflections as a function of applied electric field. As the silicon substrate was systematically removed from beneath the electrode film and the mechanical boundary constraints of the substrate are relaxed, it was found that domains have an increased ability to reorient under applied fields. When 75% of the substrate was removed, more than a six fold increase in domain reorientation was observed. This approaches values for bulk ceramics and suggests that the piezoelectric coefficients should be enhanced upon declamping.

The geometry of the released structures was also found to influence the domain reorientation. An untextured 1.77 μm thick $\text{PbZr}_{0.3}\text{Ti}_{0.7}\text{O}_3$ thin film doped with 1% Mn was fabricated with electrodes which were 75% released in two different geometries, a circular diaphragm and an elongated beam diaphragm. It was found that when the electrodes were locally released (unable to freely deform and curl upon actuation) the amount of domain reorientation observed in clamped electrodes and the electrodes with circularly released diaphragms was approximately the same. Two times more domain reorientation was seen in locally released electrodes with elongated diaphragms for the same field excursion. This disparity between the two types of release state was shown to be due to the presence of in-plane stress which was not fully relieved upon the removal of the Si substrate. In release geometries where the perimeter of the free boundary is small, such as the case with the hole geometry, the in-plane stress suppresses domain reorientation. To further investigate the role of the substrate, *in situ* synchrotron X-ray diffraction was used to study intensity exchanges on 101/110 reflections in unoriented 950 nm thick $\text{PbZr}_{0.3}\text{Ti}_{0.7}\text{O}_3$ thin film doped with 1% Mn on two substrates with different elastic properties: silicon and a borosilicate glass. The film on glass showed 32.1% domain reorientation at 3 Vc while the film on silicon showed 28.7%. Moreover, the amount of backswitching the films experienced upon release in field was shown to occur in a similar ratio to the difference in

substrate elastic moduli. Films on glass which showed better saturated domain alignment (from less backswitching after poling), had smaller irreversible Rayleigh coefficients, α . Additionally, while the films were untextured, there was a higher $\{001\}$ texture in the film on silicon. While this might have predisposed the film on silicon to have a higher $e_{31,f}$ than the film on glass, it was found that due to the higher remanence in the film on glass, the measured piezoelectric coefficients between the two films were within error ($e_{31,f}^{glass} \sim -5.9 \text{ C/m}^2$, $e_{31,f}^{silicon} \sim -5.7 \text{ C/m}^2$).

Finally, a process is presented for transferring a 850 nm thick $\text{Pb}(\text{Zr}_{0.52}\text{Ti}_{0.48})_{0.98}\text{Nb}_{0.02}\text{O}_3$ thin film from a silicon substrate, where it was grown, to a polymer substrate using a ZnO sacrificial layer. The developed process enabled measurements of PZT thin films with only 5 μm of polyimide as the substrate. Released electrodes were tested and compared to the response of a clamped film deposited concurrently. It was found that the film on polymer shows a slight increase in maximum and average remanent polarization as a result of imprint produced during the release process. Therefore, the films on polymer had a more saturated domain alignment after poling. When the films were electrically deaged, the Rayleigh behavior of both the clamped and released films was similar.

TABLE OF CONTENTS

List of Figures	ix
List of Tables	xvi
Acknowledgements	xvii
Chapter 1. Introduction and Goals	1
1.1 Statement of Purpose	1
1.2 Introduction to PZT Deposition	3
1.3 Solution Deposition	3
1.3.1 Background on Solution Deposition of PZT	4
1.3.2 Solution Deposition Processes	5
1.4 Sputter Deposition	11
1.4.1 Introduction to RF Magnetron Sputtering	12
1.4.2 Pb Control During the Sputtering Process	14
1.4.3 PZT Sputtering at PSU	17
1.4.4 Porosity Control in Sputtered PZT	22
1.5 References	31
Chapter 2. Integrated Thin Film Electronics with Piezoelectrics	36
2.1 Introduction and Motivation to ZnO Integration	36
2.2 Demonstration of Co-Processing and PZT Capacitor Charging Tests	39
2.3 Introduction to SMART-X	49
2.4 Mirror Fabrication Process Flow for SMART-X	51
2.4.1 Electrostatic Discharge Protection Circuit	58
2.5 Influence Function Measurements	59
2.6 Conclusions	65
2.7 References	66
Chapter 3. Direct Measurements of 90° Domain Reorientation in Thin Film PZT as a Function of the Substrate	70
3.1 Measurement of Domain Wall Motion in Declamped PZT Thin Films	70
3.1.1 Introduction to Clamping of Domain Walls in Thin Films	70
3.1.2 Processing Declamped Films	74
3.1.3 Measurement Process at 11-ID-C	80

3.1.4 Processing Raw Data	81
3.1.5 Volume Fraction Calculations	85
3.1.6 Quantification of Domain Reorientation	86
3.1.7 Summary of Effect of Substrate on Clamping Domain Wall Motion	90
3.2 Investigating the Role of Geometry of Release.....	91
3.2.1 Motivation.....	91
3.2.2 Processing of Thin Films with Hole and Beam Geometries.....	93
3.2.3 Investigation of 112/211 Reflections.....	96
3.2.4 Volume Fraction Calculations for 112/211 Peaks	98
3.2.5 Quantification of Domain Reorientation for Different Geometries.....	100
3.2.6 Summary of Effect of the Geometry on Clamping.....	106
3.3 Effect of the Elastic Properties on the Substrate on Domain Reorientation	107
3.3.1 Motivation to Investigate Domain Reorientation on Alternate Substrates	107
3.3.2 Solution Processing on Silicon and Glass Substrates	109
3.3.3 Processing Raw Data for Films on Silicon and Glass Substrates	112
3.3.4 Domain Reorientation in Films on Different Substrates.....	114
3.3.5 Summary of the Role of Elastic Properties of the Substrate.....	119
3.4 References	120
Chapter 4. Measurements of PZT Thin Film on a Polymer Substrate.....	126
4.1 Introduction to Flexible Piezoelectrics.....	126
4.2 Process Transfer of PZT onto Polymer	130
4.3 Characterization of Clamped and Released Films	136
4.4 Summary of the Behavior of Films on Polymer.....	144
4.5 References	145
Chapter 5. Conclusions and Future Work.....	148
5.1 Conclusions	148
5.2 Future Work	152
5.2.1 <i>In Situ</i> X-Ray Diffraction Studies on Elastic Layers	152
5.2.2 Released Film Process Development.....	154
5.2.3 Integrating TFTs onto PZT on Curved Substrates	157
5.3 References	161

Appendix. Photoresist Recipes	162
-------------------------------------	-----

LIST OF FIGURES

- Figure 1.1.** The process for preparing the CSD solution is shown (left) with the deposition process to grow the PZT thin film (right). This process is shown for a PZT 52/48 film with 2% Nb as a dopant. This process is only slightly modified for PZT of other compositions and dopants or for LNO films. The modifications for the different solution compositions are addressed in the pertinent thesis chapters.8
- Figure 1.2.** Cross-sectional microstructures of films prepared from the same solution with and without adding acetic acid. Without acetic acid, porosity is observed. When 1mL acetic acid is added to 15 mL of 0.4 M PZT solution, increased density is observed9
- Figure 1.3.** Cross-sectional FESEM micrographs showing films fabricated with 2 minute pyrolysis steps (left) and five minute pyrolysis steps (right). The shorter pyrolysis steps show high levels of porosity between solution layers, while the increased pyrolysis times enable film densification10
- Figure 1.4.** Porosity developing in a sputtered PZT film as it undergoes a post-deposition anneal. A Pb-rich film is deposited (left). As thermal energy is added, PbO will preferentially segregate into pockets both within the film and at grain boundaries (right). As the temperature is increased to crystallization temperatures, the PbO volatilizes, diffusing out of the film and leaving behind voids15
- Figure 1.5.** A schematic of the PZT sputtering chamber. The load lock system allows for one wafer to be processed at a time. The target is tilted at 15° and the target to substrate distance is about 15 cm18
- Figure 1.6.** Top down FESEM micrograph of PZT 52/48 films with 1% Nb deposited at 3 mTorr (left), 4 mTorr (middle) and 5 mTorr (right). All samples were half a micron thick and underwent the same thermal cycle post deposition (crystallization at 585 °C for 18 hours in air in a box furnace). As the pressure is increased, the amount of pyrochlore was reduced and phase pure perovskite films were achieved19
- Figure 1.7.** Top down FESEM micrographs of PZT films crystallized at 585 °C for 18 hours (left) and films crystallized at 650 °C for 1 minute (right). The 0.5 μm thick films were deposited at room temperature on silicon substrates at 4 mTorr in the same sputter run. It is apparent from the micrographs that more porosity is seen for the lower temperature crystallization21
- Figure 1.8.** Tropel 9000 interferometer image of a glass wafer heat-treated in an RTA at 650 °C for 1 minute. The fringes are concentric, indicating no appreciable deformation from the RTA thermal cycle. The red outline indicates an approximate position of the wafer. Image taken courtesy of Z. Prieskorn of the Burrows Lab at PSU21

- Figure 1.9.** Low field P – E loop from a cm^2 electrode of a $1.5 \mu\text{m}$ sputtered PZT thin film. The film was sputtered with a 5% excess PbO target at 5 mTorr and crystallized for 1 minute in an RTA at $650 \text{ }^\circ\text{C}$ while flowing oxygen22
- Figure 1.10.** Cross sectional micrographs of amorphous, as-deposited, sputtered PZT (left) and PZT that had been crystallized at $700 \text{ }^\circ\text{C}$ in an RTA for 1 minute. While no evidence of porosity is present in the as-deposited film, the crystallized film shows both large and small pores. It is likely that the large pores exist at the grain boundaries where PbO can easily segregate and diffuse out of the film23
- Figure 1.11.** A cross sectional micrograph for a sputtered PZT thin film, deposited at 4 mTorr and crystallized in the box furnace at $585 \text{ }^\circ\text{C}$ for 18 hours, showing a bimodal distribution of pore sizes. The larger porosity appears to occur between grains24
- Figure 1.12.** Cross sectional FESEM micrographs of PZT sputtered at room temperature and annealed in oxygen, nitrogen, and with a Pt top electrode. While the structure of the porosity changes slightly in the film annealed in nitrogen, there is not a significant reduction in porosity for any of the annealing conditions26
- Figure 1.13.** Cross sectional FESEM of PZT films deposited at room temperature which were crystallized at $585 \text{ }^\circ\text{C}$ for 18 hours, 12 hours, 5 hours and 1 hour. As the time at temperature is reduced, so is the residual porosity26
- Figure 1.14.** The cross-sectional FESEM of a film deposited at three different pressures without breaking vacuum. The film was crystallized at $585 \text{ }^\circ\text{C}$ for 18 hours. As the pressure increases, there is also an increase in the cross sectional porosity. Due to charging, the interface between the sol-gel seed layer and the 2 mTorr sputtered PZT appears blurred.....28
- Figure 1.15.** The top down (left) FESEM of a film shows high levels of pyrochlore. The cross sectional micrograph, however, shows predominately perovskite PZT with only surface pyrochlore.....28
- Figure 1.16.** Cross section of a film grown on a CSD deposited PZT sol gel seed layer at high temperature. The film is dense and columnar29
- Figure 1.17.** Top down FESEM of a film deposited with 0 V substrate bias (left) and -100 V substrate bias (right). Both $0.5 \mu\text{m}$ thick samples were deposited at $670 \text{ }^\circ\text{C}$ with an oxygen to argon ratio of 3.2% at 10 mTorr. The large negative bias resulted in a smoother surface30
- Figure 2.1.** A side-view schematic of the PZT capacitor fabricated alongside the ZnO TFT. The source of the TFT is connected to the PZT via a lead to the top electrode41
- Figure 2.2.** Top down (of a TFT on glass) and side view schematic of a typical ZnO based TFT. The ZnO channel is outlined in black41

- Figure 2.3.** a) P-E loops of a PZT capacitor before (black) and after (red) TFT deposition. There is no appreciable change in the remanent polarization or the shape of the loop. b) The leakage current density remains approximately the same as well. c) I_{DS} versus V_{GS} of a discrete ZnO TFT with $W/L = 200/20 \mu\text{m}$ co-fabricated with PZT capacitors44
- Figure 2.4.** Side view of the structure highlighting the area where a short is likely to occur. Also shown are several top down views of the sidewalls of etched PZT. The first generation samples showed sidewalls characterized by large non-uniformities. This was mitigated through careful processing as described in the text, and the second generation side walls are shown here as well45
- Figure 2.5.** Examples of excess photoresist left on the wafer after RIE removal of PZT46
- Figure 2.6.** Films with improved processing and thicker alumina layers can be taken to higher fields before breakdown enabling the measurement of improved properties47
- Figure 2.7.** A circuit diagram showing the set up for the charging/discharging measurement. The PZT capacitor and TFT are highlighted in blue.....48
- Figure 2.8.** A plot of the capacitor voltage, indicating the charging/discharging of the capacitor, versus time as the TFT is turned on and off. Assuming a single time constant for either charging or discharging, a fast charge time (3 ms) was observed and a comparatively long self-discharge time ($> 70 \text{ s}$) was observed49
- Figure 2.9.** X-ray images of the Crab Nebula from (left) ROSAT and (right) Chandra. (ROSAT Credit: S.L. Snowden, NASA/GSFC. Chandra Credit: NASA/CXC/SAO)50
- Figure 2.10.** (a) Top down view of the proposed wafer structure including a close-up of a completed array TFT. (b) Shows the side view of the materials stack on the backside of the mirror52
- Figure 2.11.** The first generation (room temperature deposition of bottom electrode) and second generation (150 °C deposition of bottom electrode) mirror pieces. While the first generation saw delamination of piezoelectric cells upon the final lift off lithography step, by increasing the temperature of deposition, better adhesion was achieved53
- Figure 2.12.** Shown here are the polarization versus field loops for films on glass used for these studies. The figure on the left was crystallized under low temperature (585 °C, 18 hours) conditions and the figure on the right was crystallized at higher temperature (650 °C, 1 min). While the low temperature conditions produced P-E loops with wider tips, both films show accepted low field remanent polarizations55
- Figure 2.13.** Shows (left) a schematic of and ACF bond (middle) a close up of an ACF bond on one of the SMART-X wafers and (right) a picture of the flex cables bonded to the wafer using ACF58

- Figure 2.14.** The influence function of the wafer with no PZT cells actuated. The PZT cells are outlined in black and numbered according to how they are referenced in the text.....61
- Figure 2.15.** The influence functions of the wafer as different PZT cells are actuated at 5 V. While the deflection of the wafer is not limited to the region directly adjacent to the actuated cell, it is clear that different areas of the wafer are successfully deflected. The actuated cells are outlined in black62
- Figure 2.16.** The influence functions for the cell actuated directly (left) and through the TFT (right). The actuated cell is outlined in black63
- Figure 2.17.** Shape change as the voltage is modulated from 2 V to 10 V for a single cell (cell 1)64
- Figure 2.18.** The deflection of the actuated cell as a function of voltage. The slope indicates a $\sim 1.5 \mu\text{m}$ deflection for every 10 V applied65
- Figure 3.1.** (a) Diffraction pattern of the film demonstrating strong $\{001\}$ preferred orientation (b) Top-down micrograph of the PZT film showing grains with no evidence of secondary phases or cracking. (c) Cross-sectional micrograph of the film indicating columnar growth of dense PZT on LNO76
- Figure 3.2.** The electrode release schematic is shown. (a) Electrodes were deposited in groups of four with a small contact pad to the side for the electrical probes during the *in situ* X-ray measurements. Different degrees of release were achieved by changing the spacing between the etch pits on each electrode. (b) Approximately 100 μm width trenches were then undercut into the silicon using a XeF_2 etch79
- Figure 3.3.** A schematic of the voltage applied to the sample during the *in situ* poling study. The voltage was first increased in steps of $0.25 V_c$ up to $1.5 V_c$. It was then decreased in steps of $0.5 V_c$ back to 0 V. The second voltage sweep took the sample up to $3 V_c$ in steps of $0.5 V_c$ and then back down to zero in steps of V_c 81
- Figure 3.4.** (a) An example of a 2D diffraction pattern with the integrated sector to create a 1D diffraction pattern outlined. Also shown in the schematic are the radial distances for the PZT and Pt peaks. (b) and (c) show the processed data of the peak intensity changes of the 200/002 peaks for the clamped (b) and 75% released (c) data. The error bars are well outside of the observed changes for both release states. The direction of increasing voltage is shown with an arrow; the lines correspond to 0 V, 12 V, 24 V and 36 V (0 kV/cm, 63 kV/cm, 126 kV/cm and 189 kV/cm, respectively).....82
- Figure 3.5.** An example of a selection of a 1D pattern taken at the highest voltage (36 V, 189 kV/cm) on a clamped sample. The dotted black line represents the processed data from the 2D diffraction pattern while the grey line shows the fit with an asymmetric Pearson VII function. The grey line is the summation of the two individual peak fits which represent the PZT 200 and PZT 002 peaks. The center positions of each peak

(indicated by a short line intersecting the middle of the peak) are used to determine how wide the window of integration should be. The width of the window is defined by assigning 2δ as the distance between the two peak centers. The integration is then performed with limits of $-\delta$ to $+\delta$ where δ is the distance away from the center of the peak. The background is not included in the integrated intensity.....84

Figure 3.6. (a) The volume fraction of 002 domains for the first cycle for different release states. (b) The volume fraction of reoriented domains for the first cycle up to $1.5 V_c$ (black) with the second cycle up to $3 V_c$ (red) in the 75% release sample. (c) The volume fraction changed (η_{002}) of the 002 peak as a function of voltage for the 4 films under different release states. Voltages as high as $3 V_c$ were applied to the films87

Figure 3.7. Volume fraction of domain reorientation at the maximum voltage ($3V_c$) applied for clamped, 25%, 50% and 75% released samples. A best fit line (R^2 value > 0.96) was used to extrapolate the volume fraction changed in a fully released sample; this corresponds to approximately 32% volume fraction reorientation.....90

Figure 3.8. X-ray diffraction pattern taken from the incompletely oriented film at the synchrotron ($\lambda=0.10801 \text{ \AA}$).....94

Figure 3.9. (a) top down and (b) cross-sectional FESEM micrographs. A small amount of pyrochlore exist on the surface but it is evenly distributed. The cross section shows good density. (c) leakage current density and (d) polarization versus field (P-E) loops. The P-E loop was taken at 10 Hz.95

Figure 3.10. Schematic showing the two different geometries of release investigated in this study. Circular shaped etch pits (holes) with resulting circular diaphragms (the diameter is indicated with the dashed line) and beam shaped etch pits (beams) with elongated diaphragms96

Figure 3.11. An example of a 2D diffraction pattern for the incompletely oriented sample with 130 nm of TiO_2 beneath the bottom electrode. The integrated sector to create a 1D diffraction pattern is outlined and PZT/Pt peaks are labeled.96

Figure 3.12. Line profiles extracted from the 2D diffraction patterns for clamped, hole released, and beam released PZT films. While clamped and hole released electrodes show similar amounts of domain reorientation between 0 V and 36 V, there is a noticeable increase in domain reorientation in the beam release geometry.....97

Figure 3.13. An example of the data fitted with two Lorentzian functions for the sample released via beam geometry at $3 V_c$98

Figure 3.14. The volume fraction of 211/112 domains as a function of voltage. The clamped electrode and the electrode released via the beam geometry (beams) show similar initial domains volume fraction, while the electrode released via the hole geometry show a different volume fraction.99

Figure 3.15. The volume fraction of 112 domains reoriented with applied field for the first voltage cycle where the structures are locally released	100
Figure 3.16. Finite element models of the z-displacement of the released areas of the circular and elongated beam diaphragms. The maximum displacement seen in the beam diaphragm is an order of magnitude larger than the displacement due to strain relaxation seen in the circular diaphragm	102
Figure 3.17. Reorientation of the 112 domains for three different geometry release states upon the second voltage sweep up to $3 V_c$	103
Figure 3.18. A schematic showing possible symmetrical breakage patterns of the circular diaphragms. The schematic shows (from left to right) a fully intact membrane and then ones with two, three and four splits	104
Figure 3.19. Integrated data from clamped and 75% released, 640 nm thick {001} oriented gradient free PZT 30/70 films. The 75% released electrode was released using a circular geometry. Both clamped and released films show comparable amounts of domain reorientation	106
Figure 3.20. FESEM micrographs of the film on glass (a, b) and on silicon (c, d)	110
Figure 3.21. XRD plots of the films on silicon and glass (top, $\lambda=0.11798 \text{ \AA}$) and the P–E loops for both films showing slightly higher P_r and P_{max} for the film on glass	111
Figure 3.22. Voltage sequence experienced by the films used for investigating the role of the elastic properties of the substrate on domain reorientation with applied field	112
Figure 3.23. A 2D diffraction patterns for the films on glass (left) and on silicon (right). There is a larger intensity in the center of the 2D pattern for the film on glass because of the amorphous substrate. The integrated sector to create a 1D diffraction pattern is outlined and the PZT/Pt peaks are labeled.....	113
Figure 3.24. Line profiles extracted from the 2D diffraction patterns at 0 V and $3 V_c$ for the films on both substrates	113
Figure 3.25. Example fitted data for the 110/101 peaks for the film on silicon measured at $3 V_c$ using two pseudo-Voigt functions where the FWHM is constrained to be the same	114
Figure 3.26. The volume fraction of 101 domains as a function of field for the films on silicon and on glass	115
Figure 3.27. Volume fraction of reoriented 101 domains as a function of field for the films on glass and on silicon	117

- Figure 4.1.** A schematic showing the transfer of a thin film of PZT from a silicon substrate to a thin polymer. The metal/PZT/metal stack is deposited on a sacrificial ZnO layer. After fabrication the ZnO is removed via wet etching, freeing the film onto the polymer ...131
- Figure 4.2.** Schematic showing the Pt pattern (in blue) for these samples. The center of the wafer has a top electrode pattern, accessible after release, for measurements of the PZT on polymer (Region A). The edges of the wafer has blanket Pt for a common bottom electrode for measurements of clamped PZT (Region B).132
- Figure 4.3.** Top down and cross sectional FESEM micrographs of the as-deposited film on a silicon substrate. PZT from the regions to be released and from the regions which remained clamped are both phase-pure and crack free. The cross-sectional micrograph, representative of both regions, shows good density and columnar grains. The subtle mottling observed in the top down FESEM is likely the result of small PZT grain boundaries. What appears as more defined grain boundaries in the top-down view is likely to be cluster boundaries133
- Figure 4.4.** Optical microscope pictures of cracking observed on the released film134
- Figure 4.5.** Pictures showing the evolution of the film as it is released from the silicon substrate in an acetic acid bath.....135
- Figure 4.6.** FESEM micrograph of an electrode showing cracking. The dark area to the left of the electrode (outlined in blue) is a result of charging from the electron beam. The excessive cracking near the boundary of the backside polymer is highlighted with a red dashed line.136
- Figure 4.7.** Polarization versus field loops for the clamped and released states of the film. The P–E loop on the left represents unaltered data while the released data in the P–E loop on the right has been shifted by the difference in imprint between the two films. The shifted loops shows similar remanant polarizations and coercive fields137
- Figure 4.8.** P–E loops of an unpoled released electrode and a released electrode which was poled at $3 V_c$ for 20 minutes at $75\text{ }^\circ\text{C}$. The imprint in the released film does not change with poling139
- Figure 5.1.** Pictures showing the evolution of the film as it is released from the silicon substrate in an acetic acid bath.....155
- Figure 5.2.** Schematic showing the process of releasing a film from its substrate through the use of an exfoliation layer. The exfoliation layer interface is modified with XeCl laser irradiation causing a weaker connection to the substrate.....156
- Figure A.1.** The photoresist profile of AZ4999 when developed using a surface inhibition layer.....165

LIST OF TABLES

Table 2.1. Etch Parameters of PZT and Pt.....	40
Table 2.2 Sputter Parameters of PZT on Glass.....	53
Table 2.3 Oxygen Plasma Etch Parameters	56
Table 3.1 Etch Conditions Utilized for Sample Processing.....	78
Table 3.2 Effect of Geometry on Rayleigh Coefficients in Previous Work	93
Table 3.3. Materials Properties Used for COMSOL Models.....	101
Table 3.4 Material Properties of the Substrates	116
Table 3.5 Rayleigh Behavior of Films Measured at 1 kHz.....	118
Table 3.6 $e_{31,f}$ and Lotgering Values for PZT on Silicon and Glass	119
Table 4.1. P-E Characteristics for Clamped and Released Films	138
Table 4.2. Rayleigh Characteristics for Clamped and Released States	140
Table 4.3. Rayleigh Characteristics for Unpoled Clamped and Released Samples.....	141
Table 4.4. Rayleigh Parameters Reported in Previous Work	142
Table A.1 Shipley SPR 955 2.1	162
Table A.2 Shipley SPR 3012	163
Table A.3 LOR 5A.....	163
Table A.4 Microposit S1813.....	163
Table A.5 Double layer lithography with PMMA 950 A3	164

ACKNOWLEDGEMENTS

I cannot begin to find words to express how fortunate I have been to have Dr. Susan Trolier-McKinstry as my adviser during my time here at Penn State. During the PhD process, it can be hard to have perspective on how you are growing, but when I think back to my time as an unpolished first-year, fresh from my undergraduate studies, I have come a long way. This is due largely to the guidance of Dr. McKinstry, who has had an enormous impact on my professional development. I am so thankful for the amount of time, patience, and kindness that I have been shown by her. At so many times during my PhD I have looked back and been thankful that she took me on as a student. I owe her so much more than can be conveyed in a paragraph.

A tremendous thanks also goes out to Dr. Jackson, who has contributed so much time to help me navigate a challenging process development. His guidance shed light on even the most befuddling situations. Beyond this, I know how fortunate I am to have had so much of his time and attention at biweekly meetings. These meetings have trained me to be able to speak extemporaneously about my work, hypotheses, and future plans. This is a priceless skill that I consider myself incredibly lucky to have been able to hone with Dr. Jackson.

While many people go through the PhD process without ever finding a mentor, I was lucky enough to find two. Thank you to Raegan and Israel, for showing me the ropes of PZT and ZnO processing. Raegan is an outstanding scientist and I am beyond fortunate to have overlapped with her on so many projects. I'll always remember our conversations in the nanofab, the beamline, or our long drives to NCSU and Argonne National Lab. Raegan has been a mentor and friend to me over the years, and I am so thankful that she agreed to serve as a committee member so I could continue to benefit from her years of experience and knowledge. In a similar vein, I owe so much to Israel Ramirez from the Jackson group. During his own PhD, he has been

so generous with his time, energy, and knowledge. An incredibly pleasant person to work with, he always had time to meet with me, answer emails or texts, and help me out when I got stuck on something with the processing. I attribute much of my knowledge and success to his guidance and can't think of a better graduate student to have collaborated on this project with.

I would also like to thank Dr. Jacob Jones, from NCSU and his group. I have learned so much about X-ray diffraction from Dr. Jones who has always been helpful and encouraging in all interactions. He is a gifted teacher whose excitement about the experiments is infectious. I have been so fortunate to collaborate with him and the rest of his group.

Trips to the Advanced Photon Source entail long stressful hours of high-stakes work. So it might seem strange that I have some of my fondest memories of graduate school from those trips. For that, credit is largely due to the outstanding group of people we had: Raegan Johnson-Wilke, Derek Wilke, Giovanni Esteves, and Chris Fancher, Ryan Keech, and many others who came to a beamtime. I remember time at APS full of hard work and countless experiments, but also many laughs and discussions of all aspects of science. I forged great friendships there and am so thankful for how much I also learned. I hope that the students of the STM group continue the tradition of having a party sized bag of peanut M&Ms at every beamtime for many years.

I would also like to thank professors Clive Randall and Josh Robinson for participating in my thesis committee and providing an incredibly useful outside perspective. I am so appreciative for the time and energy spent contributing thoughtful suggestions to help my thesis be the best it can be. I would also like to thank Dr. Randall for being a friendly and fun travel companion and karaoke partner.

Most of the projects that I worked on in graduate school have been collaborative. I am often surprised by how lucky I have been to exclusively work with people I have a profound

respect for both personally and professionally. As such there are an enormous amount of people whose help I would like to acknowledge. I would like to thank Zach Preiskorn who, despite his busy schedule, has been a wonderful resource who is always cheerful, helpful and thoughtful. I would also like to thank the staff members of the MRI, without whom I would not have been able to complete this thesis. Particularly, I would like to thank Derek Wilke, Beth Jones, Guy Lavalle, Bill Drawl, and Mike Labella. Every one of these people goes above and beyond when help is needed. They are teachers as well as problems solvers. Often they have the knowledge to fix any problem you come to them with and they are so giving with their time and energy to explain it to you. If it's an issue that they haven't seen before, they are just as generous in helping you come up with a plan for finding a solution. The MRI staff in general is an amazing network of people who make sure you are never floundering by yourself. I am so thankful that I have never been afraid to ask for help or advice.

I would also like to thank the members of the STM group for always being helpful and providing me with a group of lifelong friends who have supported me through my entire PhD. Thanks also goes out to the members Jackson group who have helped me in countless pinches and provided resources for processing which were otherwise not accessible for me.

Finally, I would like to thank my friends and family. It is hard to find the words to thank the people who have spent the entire 26 years of my life supporting me and making me into the person I am today. My appreciation for my parents goes so far beyond what they have done for me during my thesis work, but I would never have made it here without them. They have taken my calls at all hours, dealt with the entire range of human emotions, and offered countless advice I have always taken, to my direct benefit. I also want to thank Emily Redston, for being by my side throughout it all, always having my back and being the best friend ever.

Last but certainly not least, I am so grateful for my fiancé, Charley Yeager. Even after his own graduation and starting his career beyond grad school, he has always been there to offer me his support, advice, and time. He's played a great devil's advocate to many of my ideas, which has helped me to flesh them out. I can always count on him to remind me of the big picture perspective; he has had an immensely positive impact on my time here.

The funding for this work was provided by a National Security Science and Engineering Faculty Fellowship (NSSEFF), the U. S. National Science Foundation (DMR-1410907 and DMR-1409399), NASA (NNX13AC84G and NNX13AD46G), and the Center for Dielectrics and Piezoelectrics (NSF IIP-1361571). Additionally, use of the Advanced Photon Source at Argonne National Lab (supported by the U.S. DOE under contract No. DE-AC02-06CH11357) and the technical assistance of Guy Jennings, Rick Spence and Yang Ren at beamline 11-ID-C is gratefully acknowledged.

Chapter 1. Thesis Outline and Introduction

1.1 Statement of Purpose

Piezoelectric thin films are of great interest for applications such as transducers, energy harvesters, actuators, switches, and more [1], [2]. For devices that require low drive voltages or high sensitivity, ferroelectric films with larger piezoelectric coefficients are preferred.

Ferroelectrics have two contributions to the piezoelectric coefficient – an intrinsic contribution (lattice response) and an extrinsic contribution (predominantly due to domain wall motion) [3]. The material $\text{Pb}(\text{Zr},\text{Ti})\text{O}_3$, or PZT, has high piezoelectric coefficients, which have driven its use in both bulk and thin film sensors and actuators [1], [3]. However, PZT films are challenging to integrate with complementary metal-oxide-semiconductor (CMOS) circuits.

This thesis focuses on increasing performance of PZT based microelectromechanical systems (MEMS). Work focused on increasing understanding and performance of piezoelectric MEMS devices through two means: a fundamental study exploring the clamping effect on domain wall motion of thin films, and applied work investigating the integration of thin film transistor (TFT) electronics with PZT based actuators.

There are many ways in which monolithically integrating electronics with piezoelectrics can improve the performance of MEMS devices. These include, for example, decreased noise due to adjacency of the electronics, voltage amplification of small signals, and more generally, control electronics where silicon or organic semiconductors do not provide either the required functional properties or process compatibility. The focus of Chapter 2 of this thesis is using oxide based (ZnO) thin film transistors (TFTs) in a row/column addressing scheme to reduce the number of connections needed for adjustable optics. This entailed developing a procedure for integrating the ZnO TFTs with PZT MEMS. While this technology is presented for a single

application, it could benefit numerous devices such as thin film transducer arrays or piezoelectric energy harvesters.

While developing methods to increase functionality of thin film piezoelectrics is important, it is useful to simultaneously gain a deeper fundamental understanding of their limitations. It is well known that clamping by the substrate is a significant contributor to the reduced piezoelectric coefficients seen in thin films compared to their bulk counterparts [4]. Increased understanding of the role of the substrate in determining thin film piezoelectric coefficients should result in the ability to design piezoelectric MEMS devices with increased functionality. This motivated two studies. The first sought to make quantitative measurements, using synchrotron X-ray diffraction, of how the substrate restricted domain reorientation in films which were partially released from the substrate. Reduction in 90° domain reorientation due to mechanical boundary constraints, geometry of release, and the elastic properties of the substrate are explored in Chapter 3. The second study focused on developing a process flow for transfer of a thin film of PZT from silicon to a polymer layer. The aim of this study, presented in Chapter 4, was to develop a process to transfer the film to a flexible substrate and investigate how this modified the dielectric characteristics of the film.

The general background of integration of electronics with piezoelectrics and clamping of domain wall motion on the ferroelectric response will be presented in Chapters 2 and 3, respectively. Both of these topics require high quality PZT thin films fabricated under a variety of different processing constraints. In this section, a general background on the PZT thin film processing methods used is presented. Additionally, the development of the necessary processes utilized elsewhere in this thesis is covered.

1.2 Introduction to PZT Deposition

Integrating electronics with piezoelectrics requires establishing process flows compatible with all materials in the stack. For large area array devices, high yield pieces are needed. Additionally, in order to gain an understanding of how domain wall motion is influenced by boundary conditions of the substrate, optimized processing is required to ensure that the observed effects result from controlled variables and not variations in the film due to, for example, porosity or second phases. As a result, appropriate processing conditions are essential to producing high quality samples.

The balance of this chapter focuses on the different deposition processes used for the samples fabricated for this thesis. In the following sections, background on the deposition techniques of chemical solution deposition and sputtering is presented. Additionally, details on the deposition of PZT thin films for this thesis are discussed, highlighting important parameters and non-trivial aspects of processing.

1.3 Solution Deposition

PZT thin films with excellent properties have been deposited using a variety of methods, including, but not limited to, chemical solution deposition (CSD)[5]–[7], sputtering [8]–[10], pulsed laser deposition (PLD) [11], and metal organic chemical vapor deposition (MOCVD) [12]. Of these methods, CSD and sputtering are widely employed and both were utilized for the fabrication of films in this thesis. In the following sections, the advantages and disadvantages to these techniques are discussed. Additionally, information on the deposition processes of perovskite PZT by both methods for films used in this thesis is presented.

1.3.1 Background on Solution Deposition of PZT

Chemical solution deposition of complex oxides, which includes sol-gel processing, is primarily attractive for its low cost, its flexibility, and the ease of its deposition. Furthermore, the process is easily modified to accommodate different compositions or dopants, allowing flexibility in the materials probed [5], [7].

The general process to deposit a perovskite film using CSD is to prepare a solution, apply a uniform coating of the solution on the substrate, dry and/or pyrolyze the deposited layer, and finally crystallize the film with a high temperature heat treatment. Solutions of PZT are often prepared using a 2-methoxyethanol (2-MOE) solvent; 2-MOE dissolves lead acetate, a widely-used precursor for lead, and the 2-MOE can act as both a solvent and a modifier [6], [7]. To deposit the solution on the substrate, spin coating is most commonly used, however dip-coating and spraying are also employed [5]. For spin coating, the appropriate spin speed used to deposit one layer of the solution will vary depending on the solution molarity, solution viscosity, and the desired thickness of the layer. Thinner coatings are often preferred as a tensile stress will develop upon drying. If the deposited layer is too thick, it leads to cracking [5]. While CSD can be performed both with and without pyrolysis steps, generally it works best to have at least one pyrolysis step between 200 °C and 400 °C before crystallization when using a 2-MOE based solution [7]. A typical process includes a drying step (250 °C) in order to eliminate the organics from the solvents prior to a pyrolysis step (400 °C). It is during the pyrolysis step that residual organics are removed, the structural rearrangements necessary for crystallization begin, and the film adopts short range order [7]. Following pyrolysis, the material is amorphous [13]. The perovskite phase is formed during the crystallization step via a nucleation and growth process. At the beginning of crystallization, there is not enough thermal energy provided to nucleate the

perovskite structure and, as a result, fluorite (sometimes referred to as a low temperature pyrochlore) develops first, even though it is metastable [7], [13]–[15]. After the formation of the fluorite, the driving force for PZT nucleation is decreased. This is evidenced in studies comparing nucleation density of PbTiO_3 , PbZrO_3 , and $\text{Pb}(\text{Zr}_{0.45}\text{Ti}_{0.55})\text{O}_3$. It was found that in PbTiO_3 , where no intermediate phase develops, nucleation densities were higher compared to the Zr containing compounds, which favor development of metastable fluorite phases [13]. With the reduced driving force as a result of the fluorite structure, heterogeneous nucleation is favored. In cases where nucleation from the bottom interface is favored, a characteristic columnar structure for the PZT thin films results [7], [14]. While most solution-based routes to deposit PZT follow a similar outline, it should be noted that the specifics of processing will influence the characteristics of the resulting film [5].

1.3.2 Solution Deposition Processes

Solution Preparation

For samples deposited on silicon substrates, chemical solution deposition (CSD) of PZT was the primary deposition method. The CSD process to deposit oxide thin films has been widely studied and is well documented in the literature [6], [7]. In this thesis, CSD was used to deposit several different compositions of PZT (some including dopants) as well as LaNiO_3 (LNO), a conducting oxide perovskite material which was occasionally used as a bottom electrode to promote $\{100\}$ orientation of PZT. A typical process to make solution is shown in Figure 1.1. For the CSD deposited films for this thesis, a 2-methoxyethanol (2-MOE)-based solution chemistry was used. The lead precursor (lead acetate trihydrate) was weighed and dissolved in 2-MOE. Any other solid precursors for dopants, such as manganese acetate tetrahydrate were also added along with the lead. The solution was then dehydrated to a powder

under an Ar atmosphere to remove water from the precursors. It is necessary to remove excess water as the titanium precursor is especially sensitive to hydrolysis. This sensitivity was also combatted with the use of the 2-MOE solvent which facilitates an alcohol exchange, substituting a less reactive side group into the structure [7].

During the Pb dehydration, titanium and zirconium precursors (titanium isopropoxide and zirconium *n*-propoxide) and any liquid precursors for dopants, such as niobium ethoxide, were mixed with 2-MOE in a second container. This was then combined with the dehydrated Pb and more 2-MOE and the entire solution was refluxed at 120 °C for 2 hours under flowing Ar. During the reflux process, hydrolysis and condensation reactions take place to form metal-oxide-metal bonds. Finally, the solution was distilled to approximately half the total volume to remove reaction products such as water from the condensation reactions which occur during the reflux. The chelating agent, acetylacetone, was then added to make up 22.5% of the total volume. Fresh 2-MOE was then added to bring the solution to the final volume and correct molarity. It was found that it was best to use the solution as soon as possible after preparation since the solution aged over time, changing the optimized processing conditions.

The process for making LaNiO₃ solution is similar, though the lack of moisture-sensitive compounds eliminated the need for a dehydration step. The precursors were mixed together in 2-MOE and refluxed for three hours at 120 °C. As with the PZT process, the solution was distilled before the addition of the chelating agent and fresh solvent.

Solution Deposition

Following solution preparation, the solution is spun onto a substrate, pyrolyzed and finally crystallized in an RTA. The thickness of each layer depends on the molarity of the solution and the spin speed used in spin coating. Typically, solutions of 0.4 M were used as they

have a good balance between depositing thick enough layers to make generation of 1 μm thick films reasonable, but not being so thick that the film cracks. Generally, the 0.4 M PZT films used in this thesis produced a layer thickness of ~ 80 nm/layer for a spin speed of 1500 rpm. In other cases, 0.55 M solutions were used (~ 115 nm/layer) for depositing films up to 2 μm to reduce the overall time for the process. Often during the deposition particularly of thicker films, excess solution from the edge bead of the wafer was removed with a Q-tip soaked in 2-MOE. This helps prevent thickness build up and crack initiation at the edges. The deposited film was dried at 250 $^{\circ}\text{C}$ and pyrolyzed at 400 $^{\circ}\text{C}$. The length of these steps was changed depending on the material and composition, but in many cases, 5 minute steps were used to ensure dense PZT films. The final step in the process, the crystallization step, was carried out in a rapid thermal annealer (RTA). Films were crystallized at temperatures between 650 and 700 $^{\circ}\text{C}$ for 1 minute with ramp rates of 3 $^{\circ}\text{C}$ or greater. For films where orientation control was important, 650 $^{\circ}\text{C}$ crystallization temperatures with a one minute hold at 520 $^{\circ}\text{C}$ was used. The solution deposition and thermal cycles were repeated until the desired thickness was reached. A process flow for the solution preparation and deposition is shown in Figure 1.1.

Finished films were investigated using X-ray diffraction (XRD) and field emission scanning electron microscopy (FESEM) to determine the orientation and phase purity, respectively.

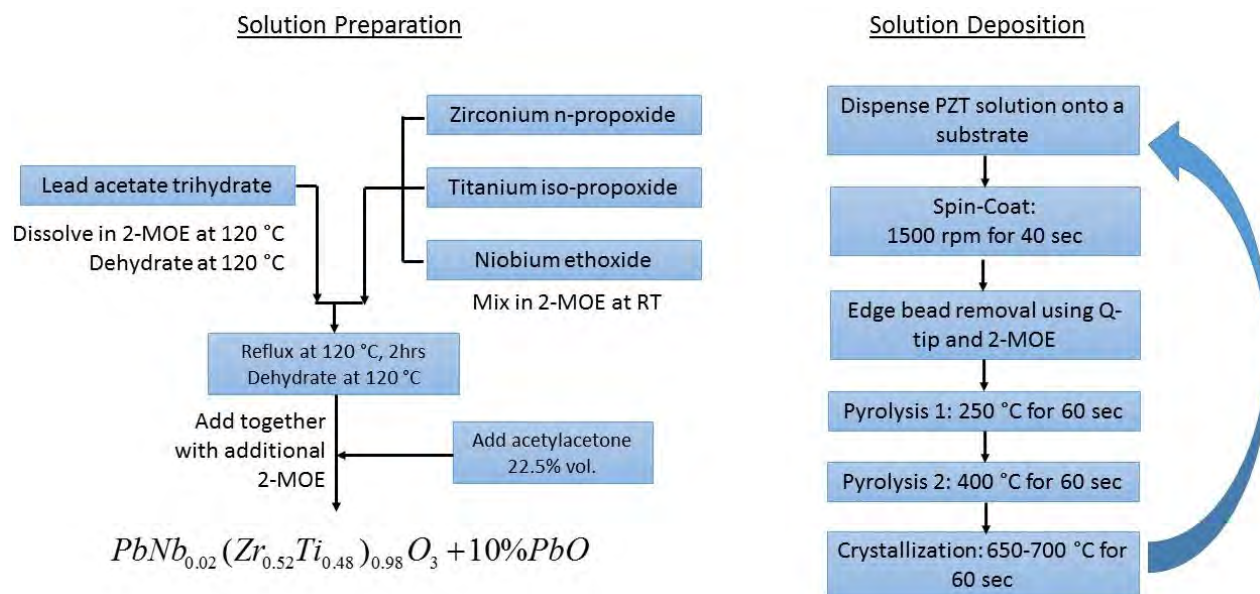


Figure 1.1. The process for preparing the CSD solution is shown (left) with the deposition process to grow the PZT thin film (right). This process is shown for a PZT 52/48 film with 2% Nb as a dopant. This process is only slightly modified for PZT of other compositions and dopants or for LNO films. The modifications for the different solution compositions are addressed in the pertinent thesis chapters.

Densification of the Films

The densification of the PZT is a very important aspect of the processing. Porosity in the film introduces volumes with low dielectric constants. These degrade the net film dielectric constants and create field concentrations in the area surrounding pores that could reduce the lifetime of the material. Additionally, residual porosity will change the elastic compliance and stress state of the film, complicating experiments investigating the role of the substrate [16].

Porosity is a function of both the solution and the film deposition processing. It typically formed between sol-gel layers. The pores are typically several nm in diameter and were detected both by ellipsometry and FESEM.

Solution chemistry plays a role in the densification of the PZT films. Generally, by modifying the solution so that the polymeric network is less stiff, higher density can be achieved. After the solution is made, it begins to age. During the aging process, condensation reactions continue to take place, creating stiffer bonds between polymer chains [17]. As a result, it was

seen that solutions used soon after preparation produced less residual porosity than aged solutions.

Additionally, it was found that adding a small amount of acetic acid (1 mL acetic acid: 15 mL PZT solution) just prior to film deposition benefits the final microstructure, as discussed below. The acetic acid is thought to reduce the number of particles in a deposited film as the acid can substitute for the side groups for the Ti and Zr [18] which helps keep the titanium from hydrolyzing. Additionally, during drying, polymeric gels collapse and cross link. As this occurs, the structure becomes stiff, making it more difficult for the network to continue to collapse, promoting residual porosity. In acid-catalyzed gels, the polymers are more weakly crosslinked than in gels with higher pH. This allows the structure to become denser as the network can collapse more during pyrolysis [17]. Adding glacial acetic acid will encourage acid-catalyzed reactions, resulting in denser films. Figure 1.2 shows that when acetic acid is added to the solution, increased density is observed.

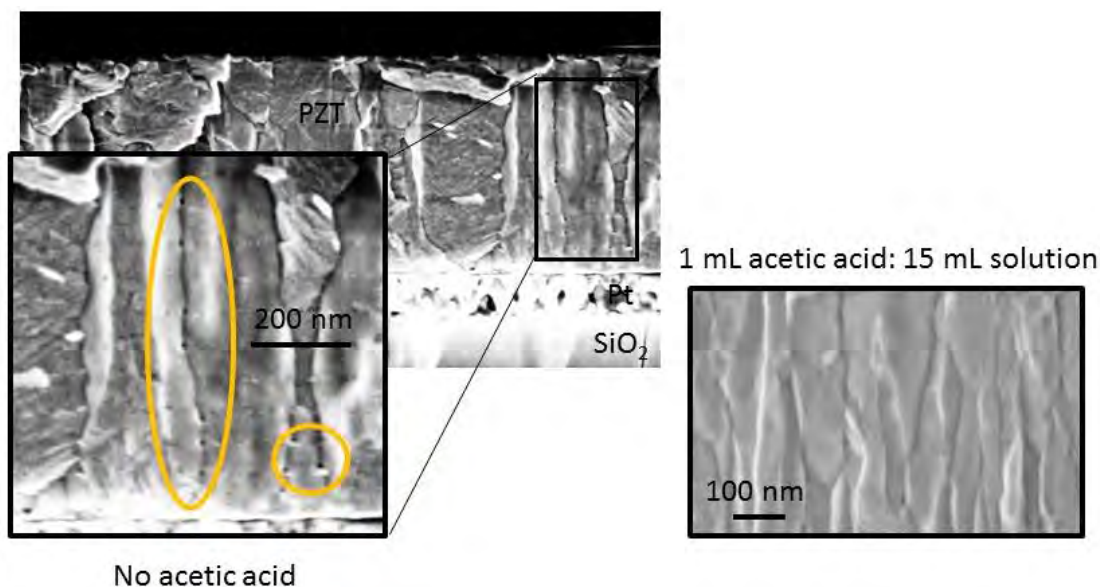


Figure 1.2. Cross-sectional microstructures of films prepared from the same solution with and without adding acetic acid. Without acetic acid, porosity is observed. When 1 mL acetic acid is added to 15 mL of 0.4 M PZT solution, increased density is observed.

Porosity can also be mitigated by modifying the film deposition conditions. A major contributor to film densification is the high temperature pyrolysis step [17]. Specifically, the time at higher temperature is important to allow the film to structurally relax and densify. Cross sectional FESEM micrographs are shown in Figure 1.3, demonstrating the difference in porosity between $\text{PbZr}_{0.30}\text{Ti}_{0.70}\text{O}_3$ films deposited with two minute pyrolysis steps compared to five minute pyrolysis steps.

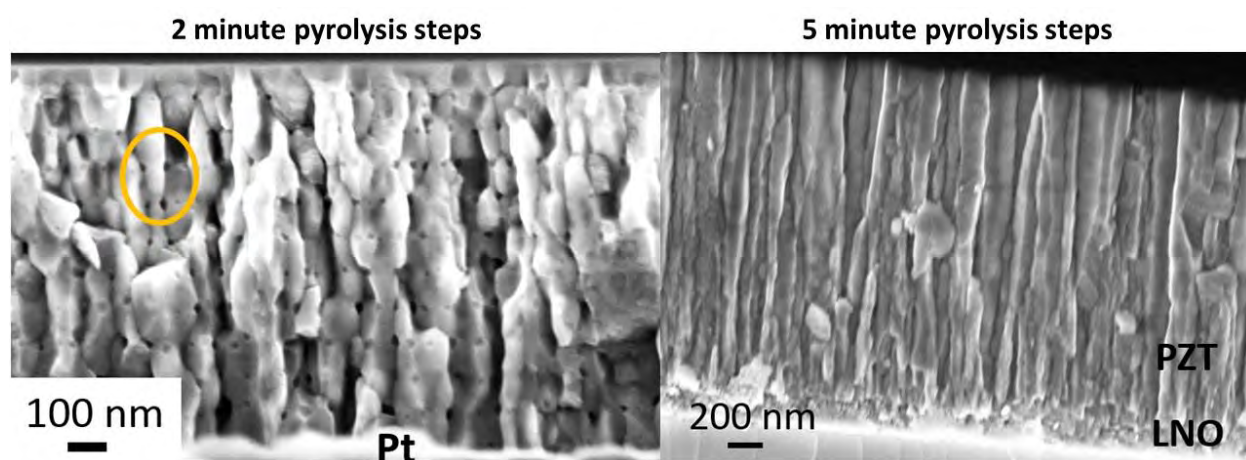


Figure 1.3. Cross-sectional FESEM micrographs showing films fabricated with 2 minute pyrolysis steps (left) and five minute pyrolysis steps (right). The shorter pyrolysis steps show high levels of porosity between solution layers, while the increased pyrolysis times enable film densification.

Pb Control in Solution Deposited Films

In order to account for lead volatility during the crystallization steps, PZT solutions were always batched with excess Pb [7]. Typically, for films grown at PSU, 10% PbO excess is added. Solutions with higher amounts of excess PbO can be used, but films grown from solutions with 12% PbO excess often had increased leakage currents as a result of the residual PbO.

However, it is not uncommon to observe nanocrystalline pyrochlore, a dielectric second phase, due to lead deficiency, on the surface of the film. Pyrochlore degrades the film properties such as remanent polarization and dielectric constant. Surface pyrochlore can be reconverted

back to perovskite with the addition of more PbO and a subsequent crystallization [19].

Typically, for all crystallization steps except the last, there is enough excess PbO in the solution to reconvert any pyrochlore on the layer below. However, if upon completion of the film, surface pyrochlore is detected in the top down FESEM, then a PbO solution capping layer was applied to convert the Pb-poor region into the perovskite phase. The PbO solution was typically low in molarity (0.08 M) as a thick layer was not needed. The solution was spun on at 3000 rpm and then dried at 150 °C for 1 minute and 250 °C for 1 minute. It was then crystallized at 700 °C for 1 minute. If any excess PbO was detected on the surface of the film after the capping layer was applied, the wafer was rinsed in 99% pure acetic acid for 1 minute to remove it.

As the properties of the films are a strong function of both the composition and doping, the electrical response of solution deposited PZT will be discussed in the relevant sections.

1.4 Sputter Deposition

CSD intrinsically presents several advantages (discussed above) compared to alternate deposition techniques. However, the process can be cumbersome for deposition of thicker films and the effects of drying stresses and non-uniform thicknesses complicate fabrication on flexible substrates such as thin glass [20]. As an aside, it is also unsuitable for applications where thin, conformal coatings of PZT on a wafer with large step heights is needed, such as for ferroelectric memories [5],[7]. In some of these cases, RF magnetron sputtering is used instead [21]. As opposed to CSD, with sputtering it is relatively easy to get both a high deposition rate as well as reasonable conformal coverage [22]. One of the main drawbacks to sputtering PZT is that stoichiometry control, especially of the volatile Pb atoms, is difficult [8], [22], [23]. Additionally, the high vacuum systems necessary for deposition are costly and the tool will likely need to be dedicated to sputtering Pb-based materials, as residual lead in the chamber

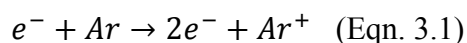
could contaminate any other materials deposited in the same chamber. As the development of the sputtering process at PSU represented a substantial development effort in this thesis, more attention will be given to it in this section.

1.4.1 Introduction to RF Magnetron Sputtering

RF magnetron sputtering of complex oxides is complicated and as such, a good understanding of the deposition process is helpful in optimizing the important parameters. Therefore, prior to discussion of PZT sputtering, a brief introduction on RF magnetron sputtering will be presented.

Generation of the plasma

The deposition chamber is comprised of both a cathode (target material) and an anode (grounded substrate and chamber). A key component to RF sputtering is the generation of a plasma, an ionized gas which will respond to electromagnetic fields [24]–[27]. The plasma is generated by accelerating electrons, using the potential difference between the cathode and the anode. An electron will eventually collide with the neutrally charged working gas atoms, typically argon, and the interaction will create a charged ion, Ar^+ , and two electrons, as shown in Equation 3.1 [24].



The resulting Ar^+ ions are accelerated towards the target/cathode and, upon collision, free atoms of the target material which eventually condense on the substrate surface [25].

Additionally, sometimes secondary electrons are also released. These electrons then contribute to further ionization of Ar atoms and are an important component in reaching deposition plasma densities [24], [25]. The plasma will be self-sustaining if the conditions within the chamber stay favorable, namely, the pressure remains in a good working window where enough collisions

occur to continue the plasma but not so many that atoms can't be ionized. Plasmas with ion densities between 10^8 cm^{-3} and 10^{14} cm^{-3} are typical for depositions [24].

Generation of sputtered material

RF power, as opposed to DC sputtering, is needed when the target material is insulating [24]–[27]. The voltage needed for sputtering is directly dependent on the resistivity of the target. Since the impedance of a dielectric is inversely proportional to frequency, a high frequency, generally 13.56 MHz, is used [24], [26]. RF power enables the use of ceramic targets like those in this thesis. However, ceramic targets are brittle. Lower powers are typically employed to keep the material from over-heating and cracking [28].

Most sputtering tools, whether RF or DC power is used, also incorporate magnetic fields near the region of the cathode [25]. Magnetron sputtering keeps secondary electrons, ejected from the target, trapped in a circular trajectory, preventing them from drifting into the chamber [24]–[26]. The confined electrons thus have a higher probability of creating ionizing collisions near the cathode. Additionally, atoms which are ionized in this region are more likely to collide with the target and, having experienced fewer collisions, will reach the target with higher energies. The increased bombardment of the target will result in more secondary electrons being ejected and ultimately trapped in the magnetic field, creating a very dense plasma [25]. By magnetically confining the dense plasma near the cathode, lower pressures can be used in magnetron sputtering systems [24].

One concern when utilizing RF magnetron sputtering is that as the direction of applied voltage switches, etching of the film can occur. The plasma itself will remain at a constant potential; the difference between the potential of the plasma and the potential that develops at the substrate, the floating potential, can accelerate the positive ions to the substrate during some

parts of the AC cycle when RF power is used [29]. A large substrate and smaller target area reduces the sheath thickness next to the anode and decreases sputtering at the substrate [24]. This is one of the reasons why the substrate is typically grounded to the chamber itself, to create an even larger area.

1.4.2 Pb Control During the Sputtering Process

One common challenge with sputtering materials where one or more of the cation have high volatility is achieving the desired stoichiometry. In particular, sputtering Pb-based compounds is complicated by the high vapor pressure of Pb species, which are easily resputtered from the growing film or evaporated during a post-deposition anneal [30], [31]. As such, excess Pb targets are used to correct for the loss of PbO and prevent the Pb-deficient pyrochlore phase from forming [23]. However, if there is too much PbO, at high temperature the excess PbO will segregate in the grown film. In some cases, it will remain in the grain boundaries, creating a more electrically conductive pathway; if the temperature is high enough, it will volatilize, creating a porous film. Figure 1.4 shows a schematic illuminating how porosity can develop during the post-deposition crystallization step in a Pb-rich as-deposited film. This is especially problematic for films which are deposited at lower temperatures and converted to the perovskite phase with a post-deposition anneal [8]. However, porosity due to excess PbO is also known to develop in films grown at high temperatures and *in situ* crystallized films [32], [33]. Thus, the amount of PbO in the as-deposited film must be carefully controlled to achieve high density sputtered PZT.

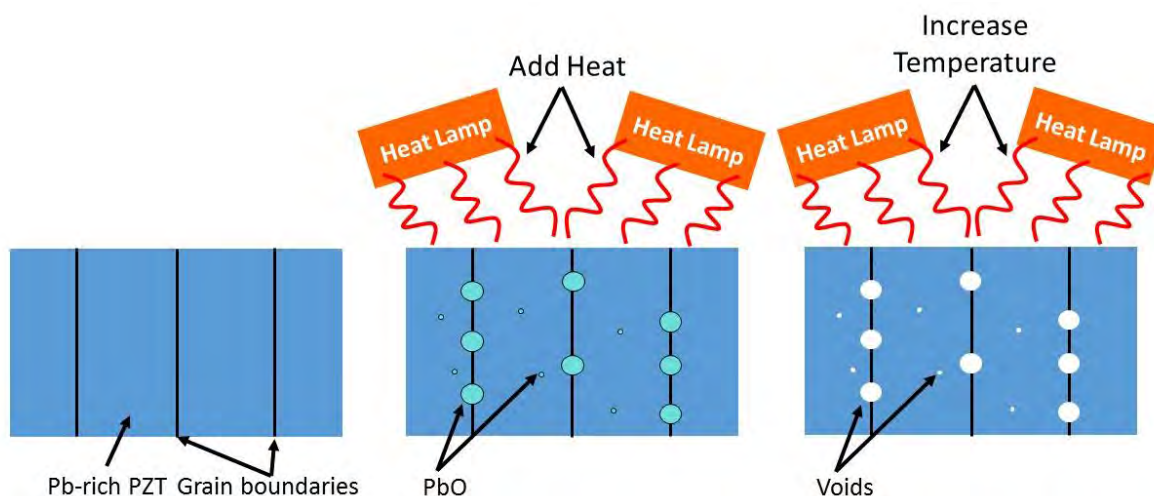


Figure 1.4. Porosity developing in a sputtered PZT film as it undergoes a post-deposition anneal. A Pb-rich film is deposited (left). As thermal energy is added, PbO will preferentially segregate into pockets both within the film and at grain boundaries (right). As the temperature is increased to crystallization temperatures, the PbO volatilizes, diffusing out of the film and leaving behind voids.

The problem of Pb control in Pb-based sputtered films is extensively documented in the literature; many solutions have been proposed to control the amount of excess PbO by modifying processing parameters for deposition of PZT, PbTiO_3 , or the Pb-La-Ti-O system (PLT) [8], [22], [23], [30], [34], [35]. While an exact process transfer isn't possible, typical conditions are available in the literature. As La^{3+} is often present in minor amounts, and Zr^{4+} is similar in size and charge to Ti^{4+} , the general processing trends are expected to be comparable between these compositions. The lead content and design of the target [36], [37], DC bias on the substrate [36], temperature of the substrate during deposition [30], amount of oxygen in the sputter gas [38], the conditions of the post-deposition anneal [8], and the sputtering gas pressure [39], for example, are all variables which can be tuned to adjust the Pb/PbO-content of the growing films. While the general concepts governing Pb control and density in sputtered films are the same, it is difficult to transfer sputtering processes between different research groups utilizing different sputtering tools, as the final film will depend on a large number of variables.

One relatively straightforward method for controlling the Pb content of the sputtered film is by varying the chamber pressure during deposition. At lower growth pressures (e.g. 2 mTorr) the ions make fewer collisions, resulting in higher energy ions impacting the surface of the growing film. As PbO is the most volatile species in the compound, this bombardment can favor the Pb deficient pyrochlore phase [34]. As the pressure is increased, the collisions in the chamber also increase. Therefore, the ions will have a lower energy available to bombard the film and resputter the PbO.

Previous reports on PLT have shown that the gas flow and gas chemistry can also have a large effect on whether or not the sputtered film will crystallize into the perovskite phase [31]. The presence of oxygen during the deposition will affect the Pb oxidation state; this influences whether the perovskite phase forms instead of pyrochlore. At the initial stages of growth, it was found that an oxygen-deficient pyrochlore phase is formed [31]. This oxygen-deficient phase is less stable than the lead-deficient phase and so the film easily converted to the perovskite phase during the post deposition anneal. It was also reported that partially oxidized Pb (or partially reduced PbO) can aid in the crystallization of the perovskite phase. As metallic Pb is oxidized to Pb^{2+} , it releases 220 kJ/mol of energy into the system [31]. Likewise, incompletely oxidized Pb also converts to PbO; the energy release depends on how much Pb needs to be reoxidized [31]. If the exotherm occurs during the crystallization step, that energy can go towards the conversion to the perovskite phase [31]. Thus, the amount of oxygen in the system during both growth and the post deposition anneal step is important for forming the correct phase.

Another deposition variable often modified to control the amount of PbO in the system is the growth temperature. Deposition at elevated temperatures is attractive because *in situ* crystallization of PZT is favored at temperatures of at least 500 °C [40]. If the film is deposited

at lower temperatures, a post deposition anneal is required to form well-crystallized material. Post deposition annealing has a large effect on the resultant microstructure and introduces even more variables into an already complicated process [8]. Additionally, the PbO stoichiometry can be self-limiting to the stoichiometric amount in high temperature depositions [30]. However, on increasing the substrate temperature, there is a concurrent increase in PbO volatilization. Therefore, when higher temperatures are used, higher Pb excess targets or fluxes must be utilized [30].

Biasing the substrate can preferentially accelerate certain charged ions towards the growing film; this in turn will affect the PbO stoichiometry via bombardment. It has been reported that a negative bias voltage produces the best results [36]. This is thought to be due to the suppression of bombardment due to negative ions, such as oxygen. The improvement in microstructure reported with negative biases may be, in part, to a more oxygen deficient growing film which aids in the crystallization of the perovskite phase.

Other methods of Pb control, such as modifying RF power [36], gas flow rates [41], [42], and the composition of the target [23], [36], [42] also affect the stoichiometry of the film although they will not be discussed in this thesis. Generally, as the amount/energy of bombardment at the surface of the film is increased, the PbO concentration in the film decreases.

1.4.3 PZT Sputtering at PSU

For PZT deposition on flexible glass, sputtering allowed films of 1.5 – 2 μm thickness to be deposited without distorting the wafer markedly [43]. Additionally, sputtering was shown to be faster, and better suited to deposition on curved substrates.

The sputter system used at PSU is a Kurt J. Lesker CMS 18. For this work, RF sputtering was chosen to enable use of ceramic oxide targets. Three inch $\text{PbNb}_{0.01}(\text{Zr}_{0.52}\text{Ti}_{0.48})_{0.99}\text{O}_3$ targets

(manufacturer: Kurt J. Lesker) with 5% excess PbO were used for this work. A schematic of the tool is shown in Figure 1.5. The process described below represents the conditions used for sputtered films in this thesis and the starting point for optimization of PZT film quality.

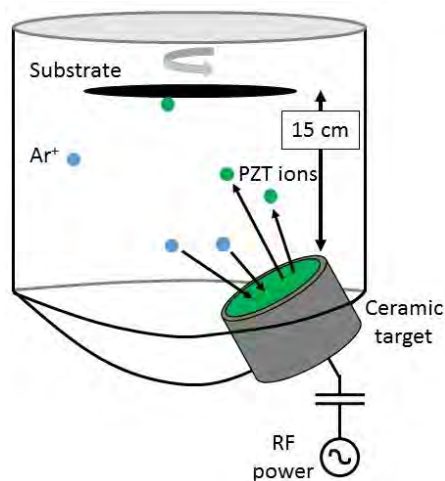


Figure 1.5. A schematic of the PZT sputtering chamber. The load lock system allows for one wafer to be loaded or processed at a time. The target is tilted at 15° and the target to substrate distance is about 15 cm.

Sputtered films for the adaptive optics work in this thesis were deposited at room temperature in an argon ambient with an RF power density of 2 W/cm^2 . Each $1.5 \mu\text{m}$ thick film was deposited in three 0.5 micron steps with crystallization anneals performed after each deposition. Half micron thick layers were used to prevent cracking which occurred on crystallization of thicker amorphous films.

As a consequence of the smaller target area (3"), targets were replaced after approximately every 30 microns deposited. Due to this, an extended pre-sputter to condition the target before every run is not feasible. As mentioned previously, the ideal working pressure during the deposition is related to the stoichiometry of the target. Therefore, a calibration study was performed on each new target to determine the optimal pressure for the perovskite phase. Figure 1.6 shows top down FESEM micrographs of PZT deposited at three different pressures. It is easy to distinguish the perovskite phase from the pyrochlore phase due to the large difference

in grain size. Perovskite PZT grains are much larger in size (typically ~ 100 nm) compared with the pyrochlore grains. It is noted that there is also some amount of bimodal distribution in the grain size for the perovskite grains of these sputtered films. The larger grains seen in the top down view were nucleated from the surface of the film, rather than the bottom electrode. This is hypothesized to be due to excess PbO remaining in the film, facilitating nucleation on the top surface. In separate work, not shown here, excess PbO on the surface of the film was shown to create secondary nucleation sites even in much thinner films deposited by chemical solution deposition. Typical working pressures for this thesis were in the range between 4-5 mTorr.

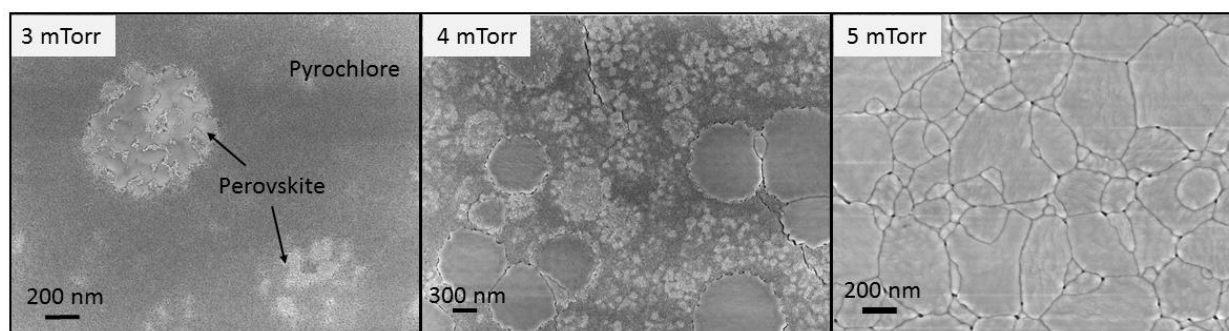


Figure 1.6. Top down FESEM micrograph of PZT 52/48 films with 1% Nb deposited at 3 mTorr (left), 4 mTorr (middle) and 5 mTorr (right). All samples were half a micron thick and underwent the same thermal cycle post deposition (crystallization at 585 °C for 18 hours in air in a box furnace). As the pressure is increased, the amount of pyrochlore was reduced and phase pure perovskite films were achieved.

Post-deposition anneal

As described previously, films were crystallized post deposition. Typical crystallization temperatures for PZT thin films are 650 °C, very close to the strain point of the Corning Eagle glass (669 °C) [44]. Two different approaches were considered for crystallization of the sputtered films on glass. The first approach was performed in a box furnace for long times (18 hours) with low process temperatures (585 °C) to ensure no deformation of the films would take place. The second approach investigated using a higher crystallization temperature (650 °C) in an RTA based on the hypothesis that shorter times (1 minute) at temperature would prevent deformation.

It was reported that a crystallization temperature of 585 °C for 18 hours with a ramp rate of 10 °C/sec was suitable for forming phase pure perovskite films [20]. While annealing the films for shorter periods of time helped reduce the porosity seen in cross sectional micrographs, heat treating films grown under the same conditions for less than 12 hours generally produced films with low breakdown strengths, indicating that there might be excess PbO still trapped.

Crystallization in the box furnace was found to produce films with increased porosity in the top down view and cross sectional field effect scanning electron (FESEM) micrographs, shown in Figure 1.7 relative to films crystallized in the rapid thermal annealer (RTA). It was found that the 400 micron thick Corning Eagle glass wafers did not shatter, nor appreciably deform, when heat-treated in an RTA with a ramp rate of 3 °C/sec and holds at 520 °C for 1 minute and 650 °C for 1 minute. A large scale interferometer measurement of a glass wafer with 1.6 μm of PZT deposited and crystallized in the RTA is shown in Figure 1.8. Due to the lack of reflective coating on the wafer, the image generated from the interferometer has weak contrast. However, concentric fringes can be observed. These appear to be similar to Newton's rings. It is expected that stress imposed by the PZT thin film will introduce a bow to the wafer. However, this indicates that the glass is not severely deformed by annealing. Because of the lack of good contrast between the fringes in some areas, it is difficult to be precise about the level of bow in the wafer although for this set-up the depth/fringe should be approximately 1.6 μm.

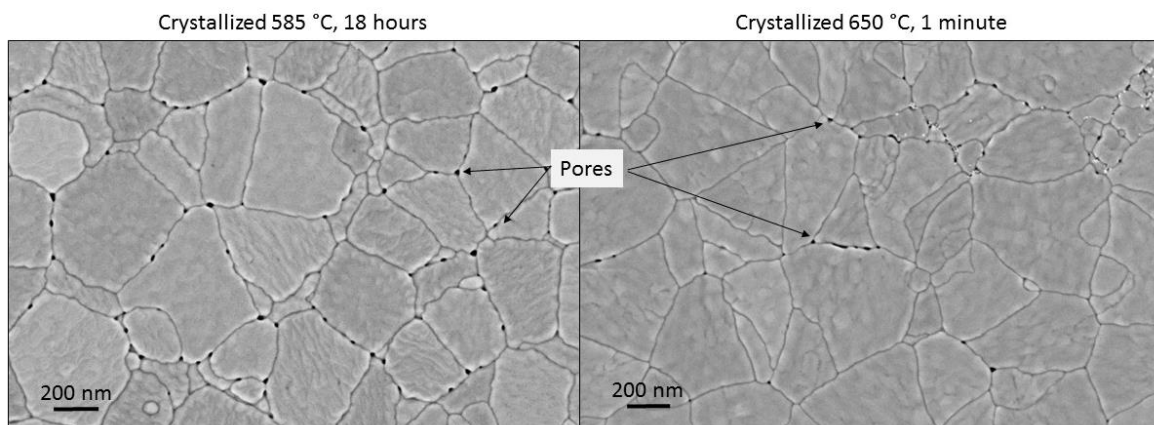


Figure 1.7. Top down FESEM micrographs of PZT films crystallized at 585 °C for 18 hours (left) and films crystallized at 650 °C for 1 minute (right). The 0.5 μm thick films were deposited at room temperature on silicon substrates at 4 mTorr in the same sputter run. It is apparent from the micrographs that more porosity is seen for the lower temperature crystallization

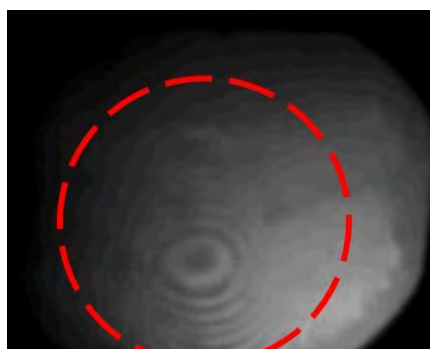


Figure 1.8. Tropel 9000 interferometer image of a glass wafer heat-treated in an RTA at 650 °C for 1 minute. The fringes are concentric, indicating no appreciable deformation from the RTA thermal cycle. The red outline indicates an approximate position of the wafer. Image taken courtesy of Z. Prieskorn of the Burrows Lab at PSU.

Electrical Properties

Despite residual porosity in the films deposited at room temperature, the electrical properties of the sputtered PZT were acceptable for applications described in Chapter 2. To probe the electrical response, Pt top electrodes were sputtered and patterned using lift off lithography. The conditions for lithography can be found in Appendix A. The dielectric constants measured at 100 Hz with a 30 mV ac signal ranged between 1400-1500; the loss tangent was < 4%. The remanent polarizations were >24 $\mu\text{C}/\text{cm}^2$ and the wafers had high yield (> 90%) with

cm² electrodes. Figure 1.9 shows the low field P–E characteristics of a sputtered film. Porosity in films often results in lower dielectric constants due to mixing rules and the low dielectric constant of air. The high dielectric constants seen in these data support the theory that the isolated pores exist (probably at the grain boundaries).

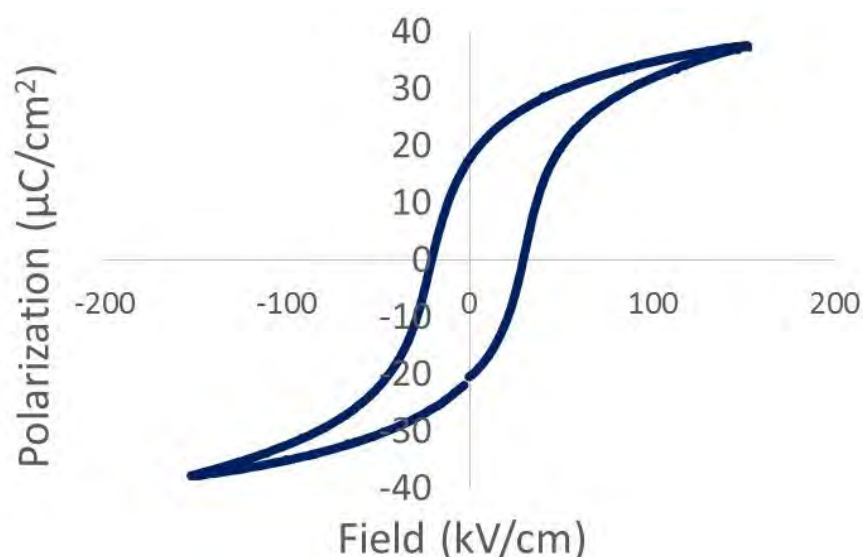


Figure 1.9. Low field P – E loop from a cm² electrode of a 1.5 µm sputtered PZT thin film. The film was sputtered with a 5% excess PbO target at 5 mTorr and crystallized for 1 minute in an RTA at 650 °C while flowing oxygen

In many cases, in order to improve the yield of large area electrodes, a small voltage (3 V) was applied through a battery to “resurrect” shorted electrodes. The lack of a current limiter allows high current to flow through the film, burning away leakage pathways from Joule heating without significantly degrading the remainder of the film. Capacitance values post-resurrection do not show significant differences from capacitance values of non-shortcd electrodes on the same film, suggesting a modest volume of degraded material [46].

1.4.4 Porosity Control in Sputtered PZT

As mentioned previously, residual porosity was observed in the post-deposition annealed films and is the result of improper Pb stoichiometric control in the as-deposited film. While the

top down micrographs show only small pores on the surface, the cross sectional FESEM images reveal the film has a higher percentage of porosity. Figure 1.10 shows a cross sectional FESEM of both an amorphous, as-deposited film and a crystallized film using the conditions detailed in the previous section. The amorphous film appears dense, indicating that the porosity seen in the crystallized films develops during the crystallization anneal.

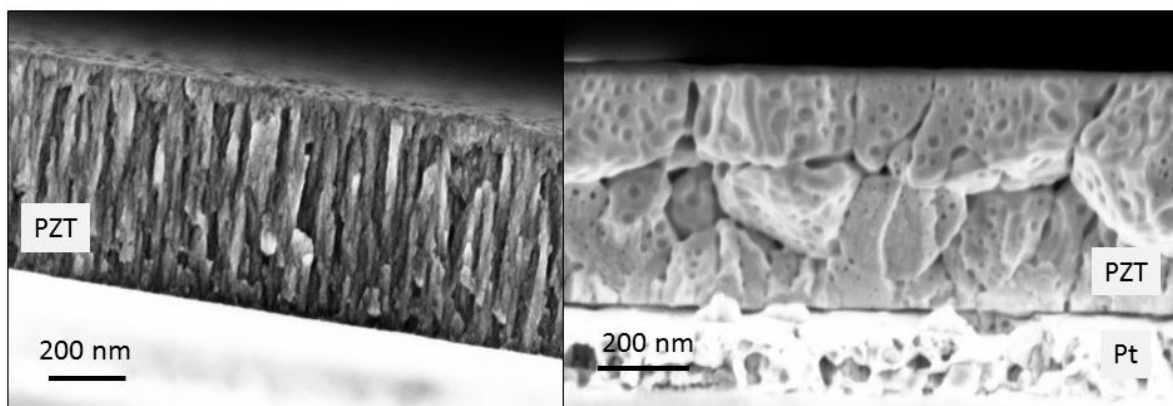


Figure 1.10. Cross sectional micrographs of amorphous, as-deposited, sputtered PZT (left) and PZT that had been crystallized at 700 °C in an RTA for 1 minute. While no evidence of porosity is present in the as-deposited film, the crystallized film shows both large and small pores. It is likely that the large pores exist at the grain boundaries where PbO can easily segregate and diffuse out of the film

Additionally, a bimodal distribution in pore size was observed in the cross sectional micrographs. Sections where smaller pores are evident are believed to be within grains whereas sections where larger pores are observed are believed to be in-between grains. As excess PbO will preferentially segregate to the grain boundaries before volatilization, it is expected that larger pockets of PbO will be located between grains and therefore, upon crystallization, produce larger pores. Figure 1.11 shows a cross sectional micrograph supporting this. In the cross section, there are two distinct pore sizes. The larger pores appear to separate grains, and often appear along lines in the micrographs, suggesting that they mark pathways for PbO escape. To prove this definitively, orientation imaging microscopy would be useful. An example of this is circled in Figure 1.11. The smaller pores may be within grains.

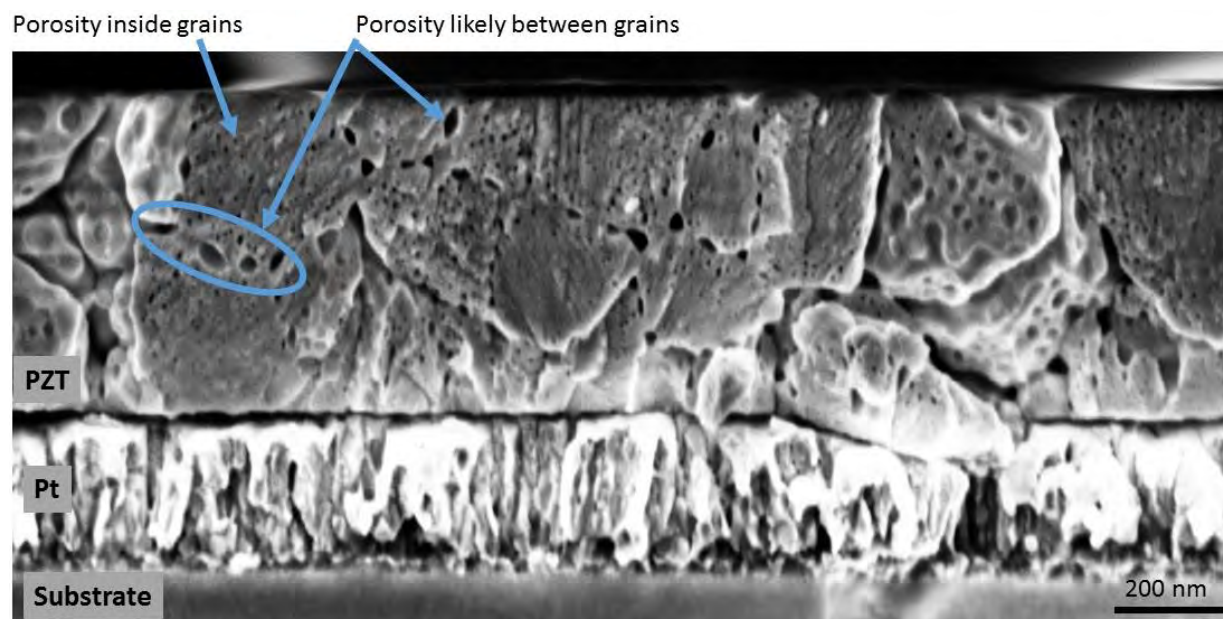


Figure 1.11. A cross sectional micrograph for a sputtered PZT thin film, deposited at 4 mTorr and crystallized in the box furnace at 585 °C for 18 hours, showing a bimodal distribution of pore sizes. The larger porosity appears to occur between grains

Experiments investigating porosity control were performed concurrently with device depositions. The short summary of the work presented here represents the work from a collaboration with several other researchers in the Troler-McKinstry group (H. G. Yeo, R. L. Johnson-Wilke, R. H. T. Wilke, and N. Kirchner).

Initial experiments focused on PZT deposition at room temperature, modifying either the substrate or the post deposition anneal conditions. Levels of porosity were estimated via inspection of cross sectional FESEM micrographs. In most films, the cross sectional FESEM revealed regions near the bottom electrode that showed higher density, presumably due to diffusion of Pb into platinum. Different seed layers were investigated to determine if the levels of porosity changed. However it was found that neither the density of the bottom electrode nor

whether or not it was saturated with Pb prior to deposition changed the porosity markedly. The substrate does not play the dominant role in the evolved microstructure.

Additionally, different post deposition annealing environments were investigated. In bulk ceramic processing it was found that the atmosphere during sintering had an effect on the final density [47]. When PZT and PLZT ceramics were sintered in an oxygen atmosphere, almost 99% theoretical density was achieved (compared to the 96% when sintered in air) [47]. Additionally, it was found that controlling the atmosphere, specifically in the early stages of firing, was important for forming dense PLZT ceramics [45]. In this case, a Pt crucible with oxygen atmosphere was used for a short (45 minute) sintering step at 1180 °C prior to a 60 hour heat treatment at 1200 °C in atmosphere in an Al₂O₃ crucible. The initial step in the Pt crucible reduced PbO loss in the early stages of firing, enabling densification [45].

For the sputtered films discussed here, annealing in oxygen, nitrogen and with a Pt top electrode (where the film is isolated from flowing gas, and where presumably outgassing should be slowed by the barrier) were investigated. The 0.5 μm films were sputtered at 4 mTorr with a 5% excess PbO target on a platinized silicon substrate. Annealing was performed at the same temperature and ramp rates (650 °C, 3 °C/min) for each sample, only varying the annealing environments. Representative cross sectional images can be found in Figure 1.12. Annealing in oxygen gave a similar microstructure to annealing in air. While films annealed in nitrogen exhibited some increase in pyrochlore near the bottom electrode, the structure of the porosity, beyond appearing more interconnected, is not improved. Furthermore, annealing with a Pt top coat did not eliminate the porosity; instead the Pt created a second nucleation interface. In light of this, it is apparent that these deposition conditions yield films too rich in PbO to be corrected post film growth.

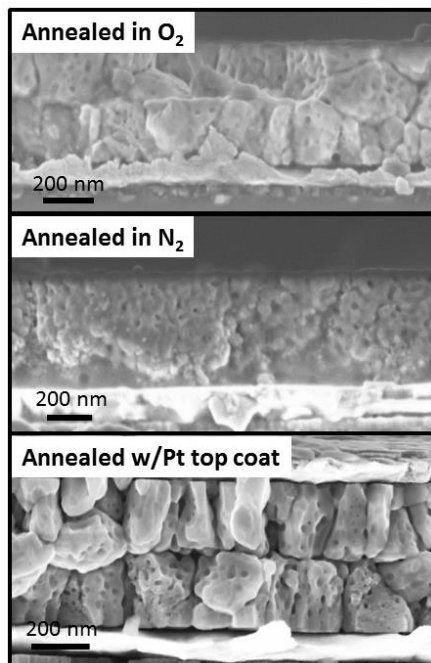


Figure 1.12. Cross sectional FESEM micrographs of PZT sputtered at room temperature and annealed in oxygen, nitrogen, and with a Pt top electrode. While the structure of the porosity changes slightly in the film annealed in nitrogen, there is not a significant reduction in porosity for any of the annealing conditions.

As mentioned previously, the conditions of the anneal will also have an effect on the resulting microstructure [8]. Porosity was investigated as a function of annealing time at 585 °C. It was found that as the annealing time was decreased from 18 hours to 5 hours, residual porosity was reduced, as seen in Figure 1.13. However, due to poor electrical properties in films annealed less than 12 hours, this was not a useful method for reducing porosity.

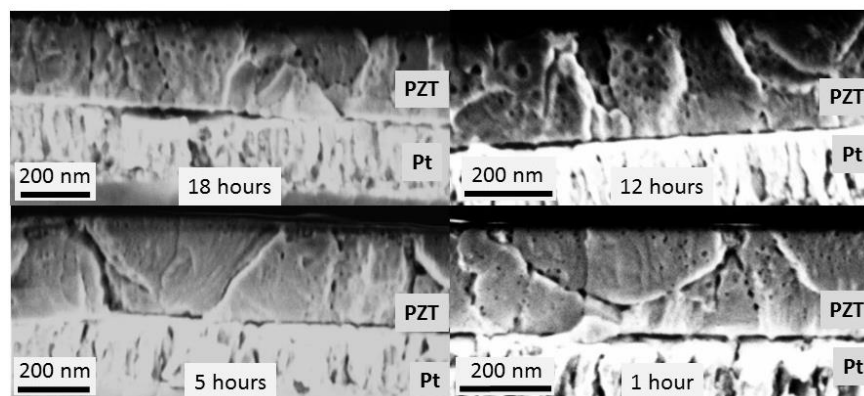


Figure 1.13. Cross sectional FESEM of PZT films deposited at room temperature which were crystallized at 585 °C for 18 hours, 12 hours, 5 hours and 1 hour. As the time at temperature is reduced, so is the residual porosity.

As such, the parameters during the deposition must be modified if the porosity is to be eliminated. It is well known that changing the deposition pressure affects the amount of PbO in the growing films. In order to investigate how porosity is influenced by the deposition pressure, a film was grown varying pressure and the cross section was inspected. The film was grown on a sol-gel seed layer to ensure that Pb diffusion into the bottom electrode would not complicate the microstructure observed. Half micron layers of PZT were grown at 2, 3 and 4 mTorr at room temperature without breaking vacuum. The film was annealed in air at 585 °C for 18 hours. High pressures (Pb rich) films exhibited higher amounts of porosity and pyrochlore. Pyrochlore which appears after a high temperature excursion, such as annealing, is often assumed to be Pb-deficient. Thus, its presence in an excessively Pb-rich as-deposited film is unexpected. One potential hypothesis to explain this is that the fluorite phase, in addition to forming a Pb-deficient phase, can accommodate excess PbO as well [14]. It is possible that in these regions the fluorite structure is stabilized by its ability to accommodate excess PbO that was not volatilized efficiently. Films deposited at lower pressures showed reduced levels of porosity and phase pure PZT (Figure 1.14).

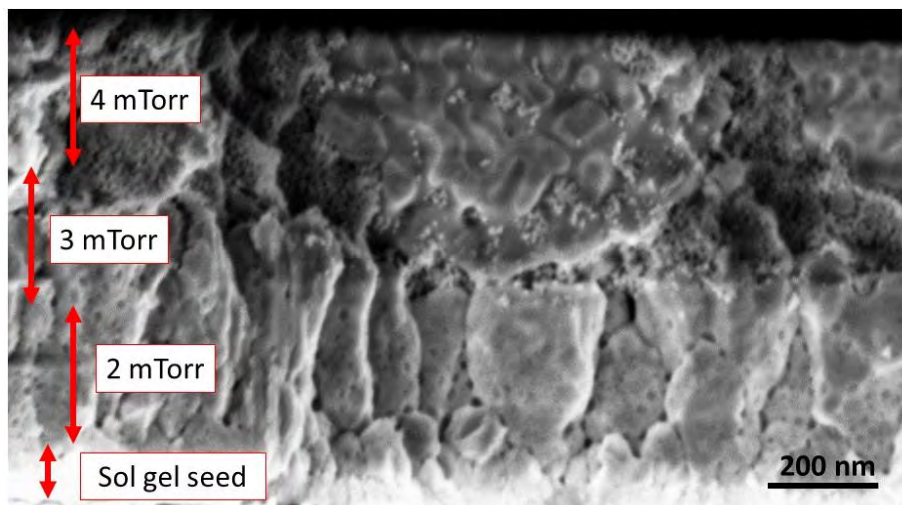


Figure 1.14. The cross-sectional FESEM of a film deposited at three different pressures without breaking vacuum. The film was crystallized at 585 °C for 18 hours. As the pressure increases, there is also an increase in the cross sectional porosity. Due to charging, the interface between the sol-gel seed layer and the 2 mTorr sputtered PZT appears blurred.

This is in contrast to the surface FESEM micrographs deposited at 2 mTorr which show a majority of pyrochlore. This is due to the Pb deficient surface layer as reported elsewhere [23], and observed in Figure 1.15. Despite the surface lead deficiency, large levels of porosity appear in the majority of the film. From this it is apparent that dense, phase pure PZT is difficult to grow only by changing pressure.

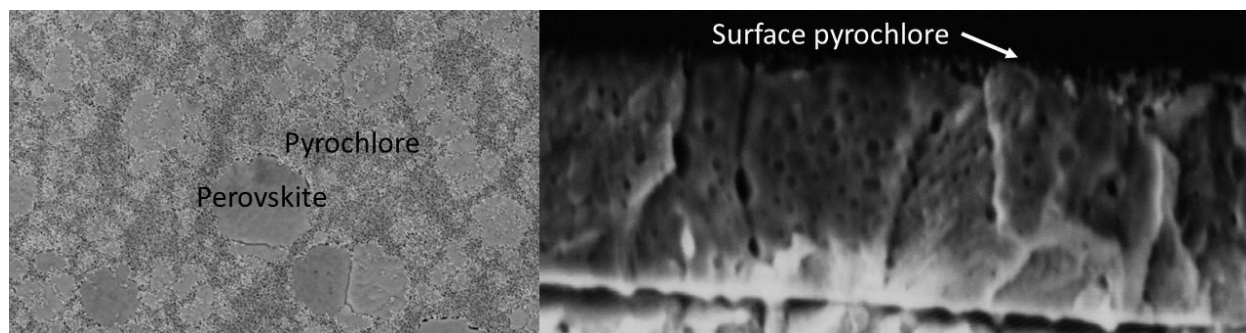


Figure 1.15. The top down (left) FESEM of a film shows high levels of pyrochlore. The cross sectional micrograph, however, shows predominately perovskite PZT with only surface pyrochlore.

Since many groups report dense films grown at higher temperature [30], [39], [48], [49], this was investigated. PZT growth at elevated temperatures was work led by H. G. Yeo of the Troler-McKinstry group. He showed that with a substrate temperature of 670 °C with a 10%

excess Pb target at 10 mT, phase pure, dense as-deposited PZT were grown on a CSD deposited PZT seed layer. An example of a dense film is shown in Figure 1.16. Density is likely enabled by self-limiting of PbO content as the evaporation during growth is balanced by the high excess Pb content of the target [30], [49]. The crystallinity of these films can be increased with a post deposition anneal at 650 °C for 1 minute in oxygen. Additionally, H. G. Yeo demonstrated that by incorporating 3.2% oxygen during growth, leakage and shorting of the PZT was reduced. While the high growth temperature studies show great improvement in the microstructure achieved, it is noted that the surface of the film is very rough. As such, a sol-gel PZT capping layer was sometimes needed before electrical properties could be measured.

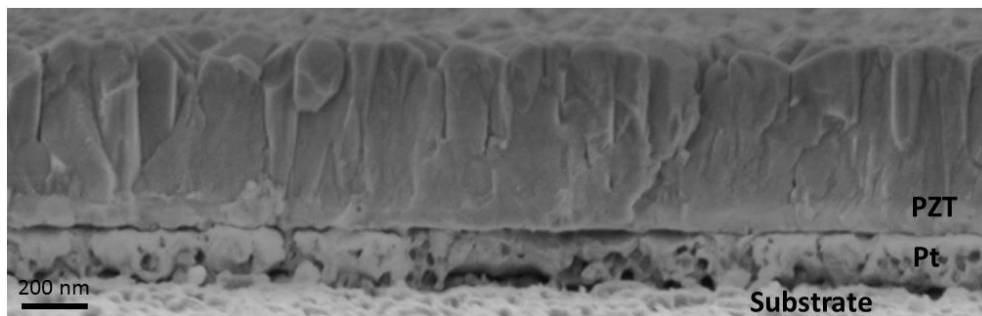


Figure 1.16. Cross section of a PZT film sputtered on a CSD deposited PZT sol gel seed layer at high temperature. The film is dense and columnar.

In an effort to reduce the roughness, a bias was introduced. Previous studies demonstrated that a negative bias on the substrate of the film during growth resulted in a smoother surface [36]. A -100 V bias was put on the substrate of the film during growth at the same elevated temperature conditions developed by H. G. Yeo. A comparison of top down FESEM of the films grown at the different conditions show that the negative bias does indeed smooth the surface, as seen in Figure 1.17.

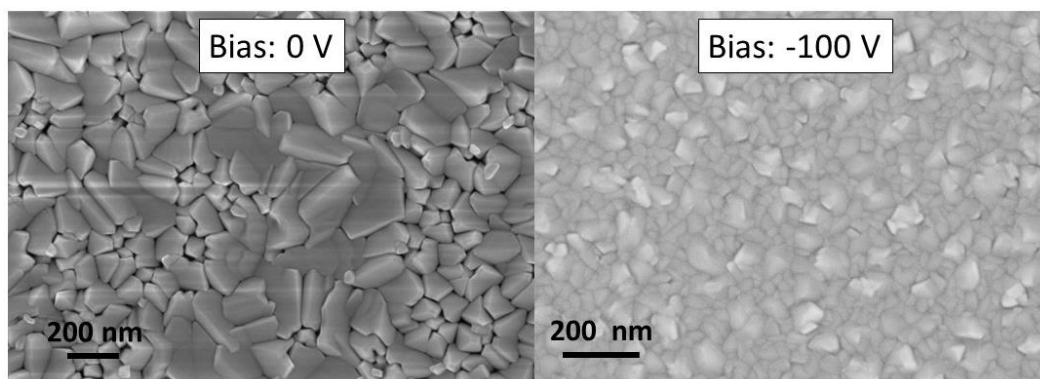


Figure 1.17. Shows the top down FESEM of a film deposited with 0 V substrate bias (left) and -100 V substrate bias (right). Both 0.5 μm thick samples were deposited at 670 $^{\circ}\text{C}$ with an oxygen to argon ratio of 3.2% at 10 mTorr. The large negative bias resulted in a smoother surface.

While the reason for this is currently unknown it is likely related to higher energy ion bombardment and increased resputtering of the growing film surface which is correlated with smoother film surfaces [24],[36]. However, while the roughness of the surface was reduced with the -100 V negative bias on the substrate, the stress exhibited by the film was greatly increased. This was evidenced by the swelling of the lattice parameters seen in the XRD data and the fact that upon annealing the film, extensive delamination was observed.

Substantial progress growing dense PZT films has been demonstrated, although PZT sputtering still remains a challenge and additional tuning of parameters is needed. Further investigation into Pb control in the sputtered films is ongoing. The current focus is on reducing the stress in films deposited under bias without sacrificing roughness. Additionally, the films of the high temperature work shown here were all grown on a PZT CSD deposited seed layer. Growth of dense films without the seed layer must also be investigated. Finally, the process must be modified for alternative substrates such as glass.

1.5 References

- [1] G. L. Smith, J. S. Pulskamp, L. M. Sanchez, D. M. Potrepka, R. M. Proie, T. G. Ivanov, R. Q. Rudy, W. D. Nothwang, S. S. Bedair, C. D. Meyer, and R. G. Polcawich, "PZT-Based Piezoelectric MEMS Technology," *J. Am. Ceram. Soc.*, vol. 95, no. 6, pp. 1777–1792, 2012.
- [2] P. Muralt, "PZT Thin Films for Microsensors and Actuators : Where Do We Stand?," *IEEE Trans. Ultrason. Ferroelectr. Freq. Control*, vol. 47, no. 4, pp. 903–915, 2000.
- [3] S. Trolier-McKinstry and P. Muralt, "Thin Film Piezoelectrics for MEMS," *J. Electroceramics*, vol. 12, no. 1/2, pp. 7–17, Jan. 2004.
- [4] F. Griggio, S. Jesse, A. Kumar, O. Ovchinnikov, H. Kim, T. N. Jackson, D. Damjanovic, S. V. Kalinin, and S. Trolier-McKinstry, "Substrate Clamping Effects on Irreversible Domain Wall Dynamics in Lead Zirconate Titanate Thin Films," *Phys. Rev. Lett.*, vol. 108, no. 15, p. 157604 1–5, 2012.
- [5] B. M. Melnick, J. D. Cuchiaro, L. D. McMillan, C. A. P. de Araujo, and J. F. Scott, "Process Optimization and Characterization of Device Worthy Sol-Gel Based PZT for Ferroelectric Memories," *Ferroelectrics*, vol. 112, no. 1, pp. 329–351, 1990.
- [6] S. K. Dey, K. D. Budd, and D. A. Payne, "Thin-Film Ferroelectrics of PZT by Sol-gel Processing," *IEEE Trans. Ultrason. Ferroelectr. Freq. Control*, vol. 35, no. 8717135, 1988.
- [7] R. W. Schwartz, "Chemical Solution Deposition of Perovskite Thin Films," *Chem. Mater.*, vol. 9, no. 11, pp. 2325–2340, 1997.
- [8] G. R. Fox, S. B. Krupanidhi, K. L. More, and L. Allard, "Composition/structure/property Relations of Multi-ion-beam Reactive Sputtered Lead Lanthanum Titanate Thin Films: Part I. Composition and Structure Analysis," *J. Mater. Res*, vol. 7, no. 11, pp. 3039–3055, 1992.
- [9] H. Chen, D. Yu, X. Dong, N. Duan, and Y. Wang, "The Preparation and Properties of PZT Thin Film by Sputtering Method," *Ferroelectr. Lett.*, vol. 20, pp. 35–40, 1995.
- [10] R. H. T. Wilke, R. L. Johnson-Wilke, V. Cotroneo, W. N. Davis, P. B. Reid, D. A. Schwartz, and S. Trolier-McKinstry, "Sputter Deposition of PZT Piezoelectric Films on Thin Glass Substrates for Adjustable X-ray Optics.," *Appl. Opt.*, vol. 52, no. 14, pp. 3412–9, 2013.
- [11] D. Chen, T. Murphy, and J. Phillips, "Properties of Ferroelectric Pb(Zr,Ti)O₃ Thin Films on ZnO/Al₂O₃ (0001) Epilayers," *Thin Solid Films*, vol. 491, no. 1–2, pp. 301–304, Nov. 2005.

- [12] M. B. Kelman and P. C. McIntyre, "Effect of Applied Mechanical Strain on the Ferroelectric and Dielectric Properties of $\text{Pb}(\text{Zr}_{0.35}\text{Ti}_{0.65})\text{O}_3$ Thin Films," *J. Appl. Phys.*, vol. 93, no. 11, pp. 9231–9236, 2003.
- [13] A. P. Wilkinson, J. S. Speck, A. K. Cheetham, S. Natarajan, and J. M. Thomas, "In Situ XRD Study of Crystallization Kinetics in $\text{PbZr}_{1-x}\text{Ti}_x\text{O}_3$ (PZT, $x=0.0,0.55,1.0$)," *Chem. Mater.*, vol. 6, no. 11, pp. 750–754, 1994.
- [14] M. J. Lefevre, J. S. Speck, R. W. Schwartz, D. Dimos, and S. J. Lockwood, "Microstructural Development in Sol-Gel Derived Lead Zirconate Titanate Thin Films: The Role of Precursor Stoichiometry and Processing Environment," *J. Mater. Res.*, vol. 11, no. 08, pp. 2076–2084, 1996.
- [15] C. K. Kwok and S. B. Desu, "Pyrochlore to Perovskite Phase Transformation in Sol-Gel Derived Lead-Zirconate-Titanate Thin Films," *Appl. Phys. Lett.*, vol. 60, no. 1992, pp. 1430–1432, 1992.
- [16] R. L. Johnson-Wilke, R. H. T. Wilke, M. Wallace, A. Rajashekhar, G. Esteves, Z. Merritt, J. L. Jones, and S. Trolrier-McKinstry, "Ferroelectric / Ferroelastic Domain Wall Motion in Dense and Porous Tetragonal Lead Zirconate Titanate Films," *IEEE Trans. Ultrason. Ferroelectr. Freq. Control*, vol. 62, no. 1, pp. 46–55, 2015.
- [17] M. N. Rahaman, *Ceramic Processing*. Taylor & Francis Group, LLC, 2007.
- [18] G. Yi and M. Sayer, "An Acetic Acid/Water Based Sol-Gel PZT Process II: Formation of a Water Based Solution," *J. Sol-Gel Sci. Technol.*, vol. 6, no. 1, pp. 75–82, 1996.
- [19] G. L. Brennecka, C. M. Parish, B. A. Tuttle, L. N. Brewer, M. A. Rodriguez, and M. J. Rye, "Reversibility of the Perovskite-to-Fluorite Phase Transformation in Lead-Based Thin and Ultrathin Films," *Adv. Mater.*, vol. 20, no. 8, pp. 1407–1411, 2008.
- [20] R. H. T. Wilke, S. Trolrier-McKinstry, P. B. Reid, and D. A. Schwartz, "PZT Piezoelectric Films on Glass for Gen-X Imaging," *SPIE 7803, Adapt. X-Ray Opt.*, vol. 7803, p. 78030O 1–10, 2010.
- [21] A. Mansingh, "Fabrication and Applications of Piezo-and Ferroelectric Films," *Ferroelectrics*, vol. 102, no. 1, pp. 69–84, 1990.
- [22] K. Suu, A. Osawa, N. Tani, M. Ishikawa, K. Nakamura, T. Ozawa, K. Sameshima, A. Kamisawa, and H. Takasu, "Lead Content Control of PLZT Thin Films Prepared by RF Magnetron Sputtering," *Integr. Ferroelectr.*, vol. 14, pp. 59–68, 1997.
- [23] F. Chu, G. Fox, T. Davenport, Y. Miyaguchi, and K. Suu, "The Control of Pb Loss for PZT Based FRAM," *Integr. Ferroelectr.*, vol. 48, no. 1, pp. 161–169, 2002.

- [24] M. Ohring, *Materials Science of Thin Films*, 2nd Edition. San Diego, USA: Academic Press, 2001.
- [25] K. Seshan, *Handbook of Thin-Film Deposition Processes and Techniques - Principles, Methods, Equipment and Applications*, 2nd Edition. William Andrew Publishing/Noyes, 2002.
- [26] P. M. Martin, *Handbook of Deposition Technologies for Films and Coatings - Science, Applications and Technology*, 3rd Edition. William Andrew Publishing, 2010.
- [27] S. M. Rossnagel, J. J. Cuomo, and W. D. Westwood, *Handbook of Plasma Processing Technology - Fundamentals, Etching, Deposition, and Surface Interactions*. William Andrew Publishing/Noyes, 1990.
- [28] D. M. Mattox, *Handbook of Physical Vapor Deposition (PVD) Processing*. William Andrew Publishing/Noyes, 1998.
- [29] P. May, "MSc Physics of Advanced Semiconductor Materials Plasmas and Plasma Processing Plasma Diagnostics : Electron Temperatures and Ion Energy Distributions," 2015. [Online]. Available: <http://www.chm.bris.ac.uk/~paulmay/misc/msc/msc4.htm>.
- [30] G. Velu and D. Remiens, "In Situ Deposition of Sputtered PZT Films: Control of the Growth Temperature by the Sputtered Lead Flux," *Vacuum*, vol. 56, no. 3, pp. 199–204, 2000.
- [31] G. R. Fox and S. B. Krupanidhi, "Dependence of Perovskite/Pyrochlore Phase Formation on Oxygen Stoichiometry in PLT Thin Films," *J. Mater. Res.*, vol. 9, no. 3, pp. 699–711, 1994.
- [32] O. Blanco, J. Heiras, J. M. Siqueiros, E. Martinez, and A. G. Castellanos-Guzman, "PZT Films Grown by RF Sputtering at High Oxygen Pressure," *J. Mater. Sci. Lett.*, vol. 22, pp. 449–453, 2003.
- [33] C. A. P. Muller and G. R. Fox, "Lead Titanate Coatings on Optical Fibers Deposited by Magnetron Sputtering," *J. Phys. IV France*, vol. 8, pp. 179–182, 1998.
- [34] S. B. Krupanidhi, H. Hu, and V. Kumar, "Multi-Ion-Beam Reactive Sputter Deposition of Ferroelectric Pb(Zr,Ti)O₃ Thin Films," *J. Appl. Phys.*, vol. 71, no. 1, pp. 376–388, 1992.
- [35] P. K. Larsen, R. Cuppens, and G. A. C. M. Spierings, "Ferroelectric Memories," *Ferroelectrics*, vol. 128, pp. 265–292, 1992.
- [36] S. M. Nam and T. Tsurumi, "In Situ Epitaxial Growth of Lead Zirconate Titanate Films by Bias Sputtering at High RF Power," *Japanese J. Appl. Physics, Part 1 Regul. Pap. Short Notes Rev. Pap.*, vol. 43, no. 5 A, pp. 2672–2676, 2004.

- [37] S. M. Ha, D. H. Kim, H. H. Park, and T. S. Kim, "Crystallization and Ferroelectric Behavior of Sputter Deposited PZT Using a Target Containing Excess Pb and O Contents," *Thin Solid Films*, vol. 355, pp. 525–530, 1999.
- [38] M. C. Hugon, B. E. Kim, F. Varniere, B. Agius, and E. Masetti, "Optical and Electrical Characterizations of PZT Films with Different O/Pb Stoichiometry," *MRS Proc.*, vol. 433, pp. 407–412, 1996.
- [39] K. Iijima, Y. Tomita, R. Takayama, and I. Ueda, "Preparation of *c*-axis Oriented PbTiO₃ Thin Films and Their Crystallographic, Dielectric, and Pyroelectric Properties," *J. Appl. Phys.*, vol. 60, no. 1, pp. 361–367, 1986.
- [40] F. Saharil, R. V. Wright, P. Rantakari, P. B. Kirby, T. Vähä-Heikkilä, F. Niklaus, G. Stemme, and J. Oberhammer, "Low-Temperature CMOS-Compatible 3D-Integration of Monocrystalline-Silicon Based PZT RF MEMS Switch Actuators on RF Substrates," *Proc. IEEE Int. Conf. Micro Electro Mech. Syst.*, pp. 47–50, 2010.
- [41] K. Komaki, T. Kamada, S. Hayashi, M. Kitagawa, R. Takayama, and T. Hirao, "Preparation of Pyroelectric Pb_{1-x}La_xTi_{1-x/4}O₃ Thin Films from Ceramic Target by RF Magnetron Sputtering," *Jpn. J. Appl. Phys.*, vol. 33, no. Pt. 2, No 3B, pp. 443–446, 1994.
- [42] J. D. Kim, K. Sasaki, and T. Hata, "Investigation of Oxygen Source from Vapor Phase and Target for Growth of Pb(Zr,Ti)O₃ Thin Film," *Electron. Commun. Japan, Part II Electron. (English Transl. Denshi Tsushin Gakkai Ronbunshi)*, vol. 86, no. 3, pp. 28–34, 2003.
- [43] R. H. T. Wilke, R. L. Johnson-Wilke, V. Cotroneo, S. McMuldloch, P. B. Reid, D. A. Schwartz, and S. Trolier-McKinstry, "Fabrication of Adjustable Cylindrical Mirror Segments for the SMART-X Telescope," *IEEE Trans. Ultrason. Ferroelectr. Freq. Control*, vol. 61, no. 8, pp. 1386–1392, 2014.
- [44] Corning, "Eagle 2000 Material Information," *Material Information*, 2005. [Online]. Available: [http://www.delta-technologies.com/downloads/Eagle 2000.pdf](http://www.delta-technologies.com/downloads/Eagle%2000.pdf). [Accessed: 01-Jan-2015].
- [45] G. S. Snow, "Improvements in Atmosphere Sintering of Transparent PLZT Ceramics," *J. Am. Ceram. Soc.*, vol. 56, no. 9, pp. 479–480, 1973.
- [46] R. L. Johnson-Wilke, R. H. T. Wilke, V. Cotroneo, W. N. Davis, P. B. Reid, D. a. Schwartz, and S. Trolier-McKinstry, "Improving Yield of PZT Piezoelectric Devices on Glass Substrates," *SPIE Proc.* vol. 8503, p. 85030A, 2012.
- [47] G. H. Haertling, "Ferroelectric Ceramics: History and Technology," *J. Am. Ceram. Soc.*, vol. 82, no. 4, pp. 797–818, 1999.

- [48] T. Fujii, Y. Hishinuma, T. Mita, and T. Naono, "Characterization of Nb-doped Pb(Zr,Ti)O₃ Films Deposited on Stainless Steel and Silicon Substrates by RF-Magnetron Sputtering for MEMS Applications," *Sensors Actuators, A Phys.*, vol. 163, no. 1, pp. 220–225, 2010.
- [49] T. Maeder, P. Murali, L. Sagalowicz, and N. Setter, "In Situ Sputter Deposition of PT and PZT Films on Platinum and RuO₂ Electrodes," *Microelectron. Eng.*, vol. 29, no. 1–4, pp. 177–180, 1995.

Chapter 2. Integrated Thin Film Electronics with Piezoelectrics

2.1 Introduction and Motivation to ZnO Integration

Thin film piezoelectrics are currently used in nonvolatile memory (FRAM), as well as MEMS devices such as actuators, transducers and adaptive optics [1]–[4]. For applications which require large piezoelectric coefficients, PZT can be used.

The integration of such piezoelectric devices with on-chip CMOS electronics would be beneficial in order to provide improved amplification, signal processing and feedback between sensors and actuators [5]. Additionally, for some devices a large number of piezoelectric elements are necessary, for instance to achieve high resolution ultrasound images with electronic focusing and steering [6]. By integrating the electronics with the piezoelectrics on the same chip, the parasitic capacitance is reduced, which also allows for higher sensitivity [7]. Additionally, by integrating arrays with electronic addressing, PZT MEMS can be controlled with fewer wires, decreasing the cable size (e.g. for 2D medical ultrasound arrays) and facilitating mass production [8], [9]. Furthermore, the adjacency of such electronics would enable functionality with reduced noise [5]. Integrating electronics would allow for increased performance in areas where higher piezoelectric coefficients, and thus materials such as PZT, are desired, such as medical imaging and underwater acoustics [10]. Electronics such as voltage amplifiers would be useful for driving piezoelectric actuators; conventional CMOS electronics are typically not designed for outputs greater than a 10 V operation [11].

However, there are several limitations to fully integrating PZT MEMS with existing CMOS foundries. While this integration has been performed previously, with FRAM being an example [12], it is not trivial and there are some instances where an alternative process, such as the one described here, would be useful. Many piezoelectric materials with the highest

piezoelectric coefficients contain Pb, which is considered a contamination risk in IC fabrication facilities. Before materials such as Pt and PZT (common materials in piezoelectric processing) can be introduced into a foundry, contamination studies have to be performed and appropriate segregation procedures developed [8]. Furthermore, the thermal budgets of the materials are not compatible with integration of PZT following completion of the CMOS. Crystallization temperatures for PZT tend to be $>500\text{ }^{\circ}\text{C}$, [13] temperatures at which dopant profiles of integrated circuits will become mobile and aluminum contacts might oxidize [14]. Finally, the passivation of the electronics typically introduces hydrogen, degrading the properties of the piezoelectric [14]. Despite these limitations, some lead-containing piezoelectric materials have been processed with integrated circuitry in a back-end process for FRAM [15]–[17].

Two methods have been demonstrated for integrating PZT and CMOS electronics; hybrid integration, where the devices are fabricated separately and then bonded together, and monolithic integration where the structures are fabricated on the same substrate. The latter is typically preferred for arrays or mass production in order to reduce the necessary wires [8].

Several groups have reported hybrid integration of piezoelectrics with CMOS electronics [14], [18]. For example, Kolesar *et al.* bonded 40 micron thick polyvinylidene difluoride (PVDF) to an integrated circuit using a urethane adhesive to create arrays of MOSFET amplifiers that were directly coupled via the gate to the piezoelectric for robotic skin sensing [19]. Using the same process of bonding separate sheets with conductive paste, Yokota *et al.* demonstrated a flexible strain sensing system using PVDF and organic field effect transistors (OFETs). The resulting strain sensor was mechanically flexible and the integrated circuitry was able to both amplify 10 mV signals by a factor of 100, and reduce variations in threshold voltage of the OFETs by using pseudo-CMOS inverters with floating gates. This was necessary to shift the

turn- on voltages for all OFETs in the array to one voltage [20]. Kato *et al.*, from the same group, produced arrays of PVDF ultrasound transducers on a flexible substrate and then bonded this to a flexible sheet of OFETS using an electrically conductive adhesive. The transducer array could launch and detect the reflected ultrasonic waves at 40 kHz and create a 3-D spatial image of an object approximately 210 mm away [6]. There have been many other reports using conductive bonding to electrically connect piezoelectrics with electronics [1], [5], [9], [10], [14], [21]–[23].

Integration via monolithic approaches has been demonstrated as well. Hsu *et al.* reduced the parasitic capacitance in large PVDF arrays (for sensing) by fabricating a transimpedance amplifier to convert the piezoelectric signal from charge to current using organic field effect transistors (OFETs) [24]. Similarly, Polla *et al.* designed and built working high voltage drive electronics (HVMOS) with PZT-based diaphragms and cantilevers. PZT cantilevers were successfully driven using the HVMOS structures and a tip deflection of approximately 3 μm (for a 100 μm x 50 μm cantilever with a 0.36 μm thick PZT film and 1.5 μm of low stress silicon nitride as an elastic later) was seen when 25 V was applied. The CMOS structures were characterized post PZT fabrication and the current-voltage characteristics indicated compatibility between the PZT thin film processing and the integrated circuits [11].

The work by Polla *et al.* is especially relevant to this thesis, given that a majority of the reports on integration of piezoelectric MEMS and control electronics used PVDF as the piezoelectric and pentacene for the semiconductor. However, in some applications, for instance medical ultrasound transducers, large piezoelectric coefficients are required; in this area morphotropic phase boundary PZT outshines its organic analogs, such as PVDF [6].

Pentacene based transistors typically demonstrate mobilities $< 1 \text{ cm}^2/\text{Vs}$ [6]. Therefore, there is a need to integrate transistors with higher mobilities for applications where fast switching

is desired. An example of such an application is beamforming for a 2D transducer array where, for a 50 MHz transducer, a minimum delay of 20 ps is needed [25]. Oxide electronics are attractive for their high performance and mobilities as well as their low deposition temperatures and high-stability. In particular, ZnO-based transistors deposited via plasma enhanced atomic layer deposition (PEALD) have high-resistivity with mobilities $> 20\text{-}30\text{ cm}^2/\text{Vs}$ [26]. Furthermore, the low temperature required for ZnO-based transistors suggests that integration with PZT MEMS should be possible.

In this section of the thesis, co-processing compatibility of PZT and ZnO is explored. ZnO thin film transistors (TFTs) are successfully used to control PZT capacitors, demonstrating the feasibility of integrating electronics with piezoelectrics to enable improved sensing and actuation for PZT MEMS devices. As an example, integrated electronics with piezoelectrics are being explored for a next generation x-ray telescope with excellent angular resolution as well as a large collection area [3], [4], [27], [28].

2.2 Demonstration of Co-Processing and PZT Capacitor Charging Tests

For initial studies investigating process compatibility of PZT capacitors and ZnO thin film transistors (TFT), $\text{Pb}(\text{Zr}_{0.52}\text{Ti}_{0.48})_{0.98}\text{Nb}_{0.02}\text{O}_3$ films were deposited on platinized silicon substrates using chemical solution deposition. The addition of the Nb dopant to the films increased the resistivity and decreased the leakage current density. This will decrease the current through the device during operation, which will lower the power needed. Additionally, it will increase the RC time constant of the capacitor, allowing faster charge times and longer self-discharge times. Details of solution synthesis and deposition procedures are described in Chapter 1. In short, a PZT solution containing 10% excess PbO was spun onto a platinized silicon wafer (NOVA Corporation), dried (250 °C in air for two minutes) and pyrolyzed (400 °C in air for two

minutes) before being crystallized in a rapid thermal annealing (RTA) furnace at 700 °C in air for one minute. The process was repeated until the desired thickness of PZT was achieved (760 nm). The PZT and the platinum bottom electrode were both patterned via dry etching into standalone features using reactive ion etching (RIE) in a Tegal 6572 RIE tool (Tegal Corporation, Petaluma, CA). In this case, the Pt bottom electrode was also etched to define the PZT structure, and separately into the gate for the TFT. The conditions for the PZT and Pt etches are described in Table 2.1. For these initial coprocessing studies, the TFTs were fabricated alongside the PZT capacitors. A schematic of this is shown in Figure 2.1.

Table 2.1. Etch Parameters of PZT and Pt

Material	Chamber Pressure	Gas Chemistry	Forward Power	Etch Time
Pt	5 mTorr	20 sccm Cl ₂ 40 sccm Ar	300 W at MHz 0 W at kHz	30 seconds
PZT	5 mTorr	7 sccm Cl ₂ 45 sccm Ar 28 sccm CF ₄	300 W at MHz 125 W at kHz	30 seconds

Following patterning, top electrodes were defined by lift-off using photolithography, and platinum was deposited using RF magnetron sputtering. The dielectric constant, measured both before and after ZnO deposition and patterning at 1 kHz with an ac signal of 30 mV, was ~ 1100 with a loss tangent of less than 3 %. The remanent polarization was greater than 24 $\mu\text{C}/\text{cm}^2$ and the leakage current, measured at three times the coercive voltage for 20 minutes, was approximately $1 \times 10^{-8} \text{ A}/\text{cm}^2$.

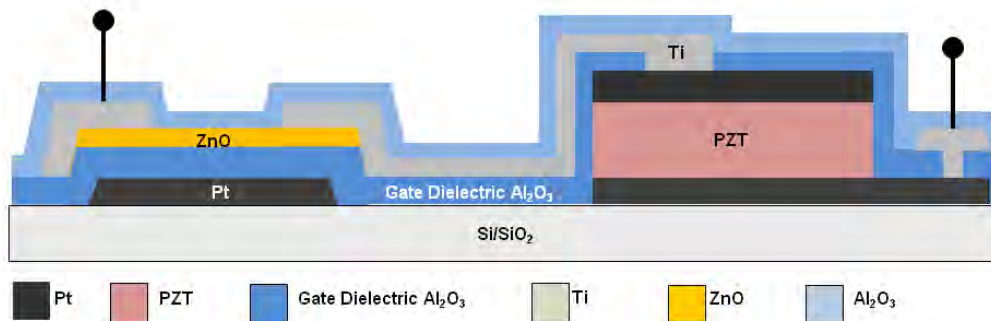


Figure 2.1. A side-view schematic of the PZT capacitor fabricated alongside the ZnO TFT. The source of the TFT is connected to the PZT via a lead to the top electrode

The process flow for fabricating the ZnO thin film transistors for this thesis was adopted from the process used by the Jackson group [26] and is outlined here. As the ZnO TFTs show excellent mobility and stability over time, modifications to the process were only imposed when the original process was either unsuitable for the materials stack or for ease of fabrication. Top down and a side view schematic of the processed TFTs is shown in Figure 2.2. Details of each step and how they were changed for coprocessing with the PZT will be given in the following subsections.

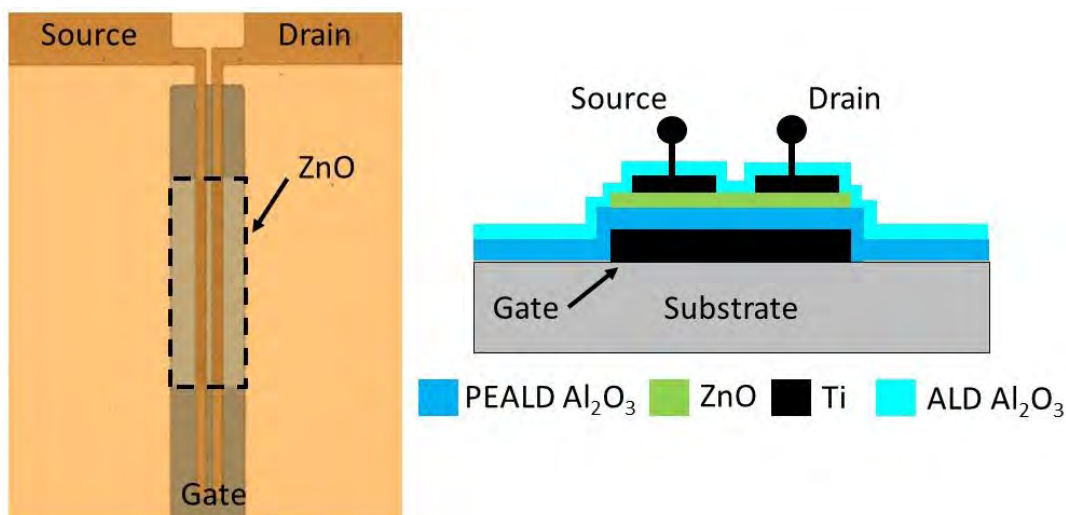


Figure 2.2. Top down (of a TFT on glass) and side view schematic of a typical ZnO based TFT. The ZnO channel is outlined in black

Gate Deposition

The first step in the transistor process used for this thesis is to deposit and pattern the gate material. Cr is often used as the bottom gate material for transistors fabricated on glass however, for ease of fabrication when the TFTs are patterned alongside the PZT capacitor, the TFT gate was made of Pt. This enabled the gate to be defined during an RIE etch, at the same time the bottom electrode for the PZT was also defined, eliminating additional material deposition and patterning. TFT characteristics with a Pt gate were similar to characteristics with a Cr gate.

Deposition of the Gate Dielectric and Semiconductor

The dielectric and semiconducting materials for the TFT (Al_2O_3 and ZnO respectively) were deposited using plasma enhanced atomic layer deposition (PEALD). The process was carried out in custom built tools in the Jackson Lab at Penn State.

In this process, a weak oxidant, typically CO_2 for Al_2O_3 depositions or N_2O for ZnO, is flowed continuously in order to remove either excess precursors and/or reaction products. The entire process is carried out at 200 °C. To begin growing the film, the metal-precursors (trimethylaluminum for Al_2O_3 and diethylzinc for ZnO) are pulsed, flow into the reaction chamber and chemisorb to the substrate surface. The growth rate of the Al_2O_3 is approximately 1.05 Å/cycle and the growth rate of the ZnO is ~ 2.5 Å/cycle. The deposition of ZnO is performed after the Al_2O_3 film was grown, but without breaking vacuum as that resulted in a non-ideal interface between the two materials [26].

After a purge to remove excess precursors, the RF plasma is pulsed to oxidize the adsorbed precursor. This process is repeated until the desired thickness is formed (50 nm Al_2O_3 and 10 nm ZnO for most of the work in this thesis).

ZnO Patterning

The ZnO is then patterned via wet etching with dilute HCl (1:4000 HCl:water) for 1 minute. This gives an etch rate of approximately 10 nm/min. This is a reliable etch, however as the ZnO is incredibly sensitive to acidic solutions, it is best to batch the etchant in large quantities where the 1:4000 ratio is easily targeted.

Al₂O₃ Patterning

For a majority of the TFTs processed for this thesis, the Al₂O₃ was patterned by wet etching with H₃PO₄. In this process, vias are opened in the Al₂O₃ in order to expose metals which will be contacted post-processing (Ti gates, Pt bottom electrode, Pt top electrodes). The resist (1 μm thick Microposit 1813) is patterned and then hard baked between 110-115 °C for 5 minutes. The alumina is then etched in a phosphoric acid bath warmed to ~ 80 °C. The etch rate for this process is approximately 40 nm/min.

Source/Drain Contacts

For the penultimate step in the transistor fabrication, titanium source and drain contacts were then deposited and patterned by a lift off process. As the ZnO is exposed during the lift off step, special care needs to be taken to make sure the acetone was neither old nor somehow contaminated as the ZnO easily etches in lower pH, polar liquids. This was generally done using a dummy wafer with ZnO. The ZnO thickness is measured before and after exposure to acetone using ellipsometry. If any ZnO etching is observed, the acetone was discarded.

Passivation using ALD Al₂O₃

Finally, the structures were passivated using ALD Al₂O₃. Passivation is necessary for good stability of the TFTs, as exposed ZnO can absorb moisture from the air which will shift

properties. The ALD alumina was deposited from trimethylaluminum and H₂O. The passivation layer was also deposited at 200 °C. Following this, a second alumina etch is performed, under the same conditions as before, to open up vias so contact can be made to the TFT array.

Post fabrication, TFTs were tested and found to have properties comparable to TFTs deposited on glass, with differential mobilities > 24 cm²/Vs. The help of J. I. Ramirez for all TFT fabrication and characterization is gratefully acknowledged.

PZT degradation studies

It is essential that the PZT characteristics do not degrade after going through TFT processing. The precursors for alumina and zinc oxide both contain hydrogen, which can be broken off during the cracking of the precursor. Hydrogen infiltration of the PZT lattice degrades properties [29]. To assess whether this was a problem, the dielectric and ferroelectric and dielectric properties were tested both before and after TFT processing. There was no appreciable degradation to the dielectric constant, the P-E characteristics or the leakage current density, as seen in Figure 2.3. Likewise, no significant changes in the aging rates for the permittivity were observed.

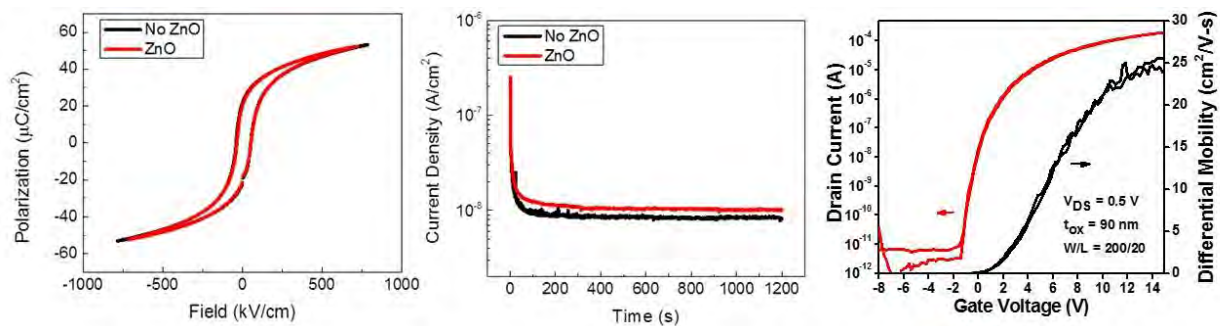


Figure 2.3. a) P-E loops of a PZT capacitor before (black) and after (red) TFT deposition. There is no appreciable change in the remanent polarization or the shape of the loop. b) The leakage current density remains approximately the same as well. c) I_{DS} versus V_{GS} of a discrete ZnO TFT with W/L = 200/20 μm co-fabricated with PZT capacitors

However, it was found that initial samples with ZnO TFTs experienced breakdown at lower fields compared with PZT that was not coprocessed. This lower breakdown strength was attributed to two factors: first, the thin, 30 nm of alumina that was deposited to serve as electrical isolation between the bottom electrode and the Ti lead that connected the top electrode of the capacitor to the source of the transistor. A schematic of the breakdown region is shown in Figure 2.4. This was combated by depositing a thicker layer of alumina as the gate dielectric (50 nm). Secondly, there was extensive damage to the sidewalls of the PZT film during the RIE step. The large non-uniformities, seen in Figure 2.4, likely created field concentrations which caused the alumina to break down at even lower fields.

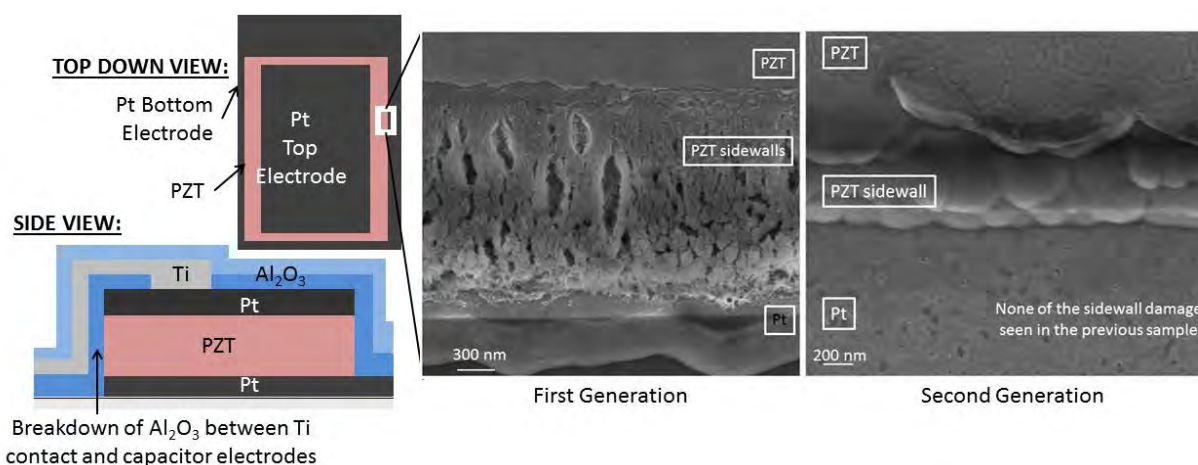


Figure 2.4. Side view of the structure highlighting the area where a short is likely to occur. Also shown are several top down views of the sidewalls of etched PZT. The first generation samples showed sidewalls characterized by large non-uniformities. This was mitigated through careful processing as described in the text, and the second generation side walls are shown here as well.

Samples were characterized in order to determine what caused this sidewall damage as it is not characteristic of RIE etching and could not be fixed with a post-etch annealing step. An analysis of the etched features in the FESEM showed excess photoresist left on the top edges of the etched PZT structure as well as along the sidewalls. Examples of the excess photoresist are shown in Figure 2.5. Figure 2.5a shows a clean sidewall with residual photoresist only on the

surface while Figure 2.5b shows excess photoresist both on the top and on the sidewalls. Additionally, the photoresist coating the sidewalls is similar in shape to the non-uniformities which are observed on the sidewall of the etched PZT. Given these two pieces of information, it is likely that the observed etch damage is linked to the residual photoresist.

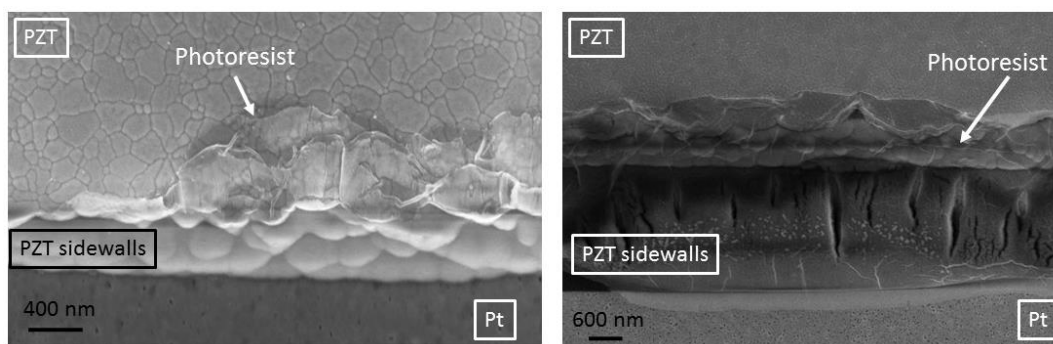


Figure 2.5. Examples of excess photoresist left on the wafer after RIE removal of PZT.

Beyond the etch damage in the side walls, the excess photoresist left on top of the film is undesirable. This photoresist could not be removed with high temperature thermal anneals, in acetone (warm or sonicated), using high power oxygen plasma, physically rubbing the features with a q-tip, or in nanostrip. All of these methods should be suitable to remove the SPR 955 2.1 photoresist that was used as the etch mask for this process. As such, it is likely that what remains is a compound created during the etch process where the etched ions are resputtered and embedded into the sidewall of the photoresist. This thin layer on the edge of the photoresist can collapse either during etching, masking the sidewall of the PZT and causing the degraded pattern to be etched in, or it can collapse during the photoresist removal, becoming stuck to the top of the PZT film.

With this in mind, it was decided that eliminating the photoresist “fences” would fix both problems. The approach taken for this thesis was to deposit a thin layer of lift off resist (LOR 5A) below the SPR 955. During the develop step, the LOR will undercut the 955. The PZT-

photoresist complex formed during the etch process will still develop but it will not be bonded to the surface of the PZT and so it will be easily removed when the LOR layer is removed. This solution worked well for the structures fabricated here; films etched with the optimized conditions showed smooth sidewalls. With the improved processing, films could be driven at higher voltages, increasing properties like the remanent polarization, as shown in Figure 2.6.

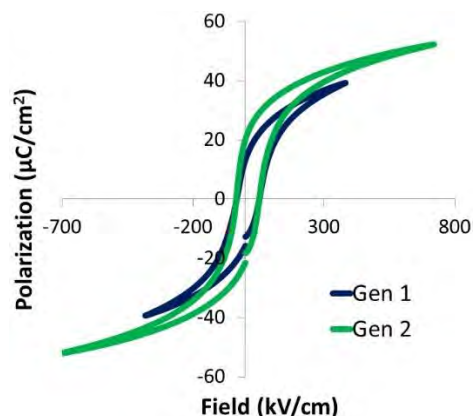


Figure 2.6. Films with improved processing and thicker alumina layers could be taken to higher fields before breakdown enabling the measurement of improved properties.

Charging/Discharging Time

Applications where the transistors control large arrays of piezoelectric devices require that the transistors can apply enough voltage to the piezoelectric within a reasonable time scale. Moreover, in adaptive optics the voltage applied to a piezoelectric capacitor must be maintained while the array charges other cells. The goal is to have a short charge time in order to charge each row or piezoelectric cells efficiently and a sufficiently long discharge time to ensure that the array will continue to hold voltage while the rest of the pixels are charged.

To test this, the structures used for coprocessing investigations, with TFTs fabricated alongside PZT capacitors, were utilized. As shown in Figure 2.1 and discussed previously, the TFT was connected to the PZT capacitor by a Ti lead. The ability of the TFT to charge the PZT was tested by turning the TFT on and off and measuring the voltage drop over the capacitor

using an oscilloscope. The TFT (Width/Length of the channel = 150/5) was turned on and off by placing +10 V and -10 V to the TFT gate, respectively. When the TFT was on, the voltage applied to the drain of the TFT was measured on the PZT pixel. Figure 2.7 shows the circuit diagram used for this measurement. The TFT and PZT capacitor are highlighted. By measuring the voltage drop over the capacitor, the charging and discharging times (defined assuming one time constant for each operation) can be determined.

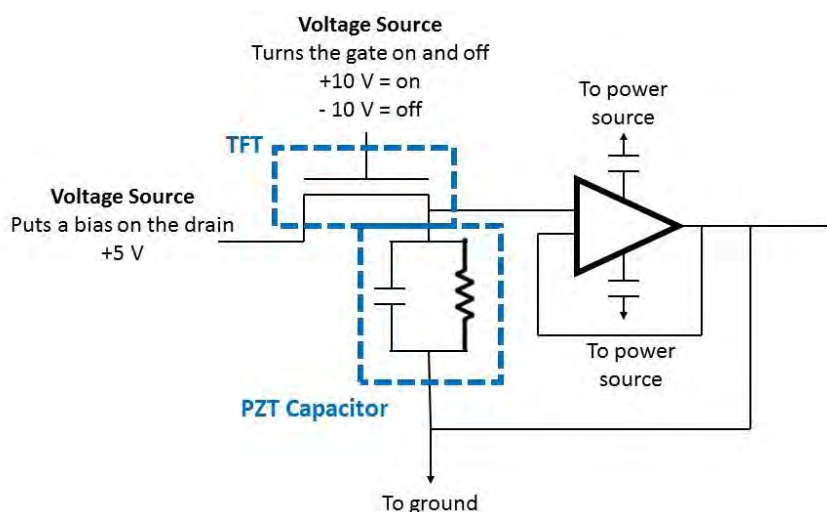


Figure 2.7. A circuit diagram showing the set up for the charging/discharging measurement. The PZT capacitor and TFT are highlighted in blue.

In order to determine the discharge time of the PZT element, it is important that neither the oscilloscope nor the TFT should interfere with the measurement. The wide band gap ZnO semiconductor ensures low leakage in the off state. Similarly, a non-inverting voltage follower was integrated into the circuit (shown in Figure 2.7 as the op amp) as a high impedance element to prevent discharging through the oscilloscope.

Different time constants were measured for the charging and discharging times. A PZT cell with an area of 0.0026 cm^2 with $C = 3 \text{ nF}$, charged in approximately 3 ms and took longer

than 70 seconds to discharge as seen in Figure 2.8. This is an acceptable ratio for the arrays in question.

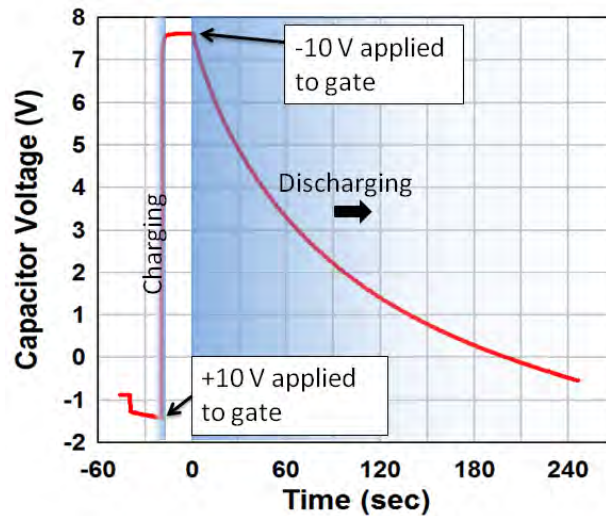


Figure 2.8. A plot of the capacitor voltage, indicating the charging/discharging of the capacitor, versus time as the TFT is turned on and off. Assuming a single time constant for either charging or discharging, a fast charge time (3 ms) was observed and a comparatively long self-discharge time (> 70 s) was observed.

2.3 Introduction to SMART-X

Figure 2.9 shows a side-by-side comparison of the Crab Nebula imaged using the previous X-ray telescope, ROSAT, and the current state of the art, the Chandra Observatory. The excellent angular resolution of the Chandra (0.5 arcsecond) allows for the details of the structure of the nebula, such as the inner ring, to come into focus whereas with the ROSAT, no features can really be detected. This increase in angular resolution has enabled astrophysicists to better understand the universe.

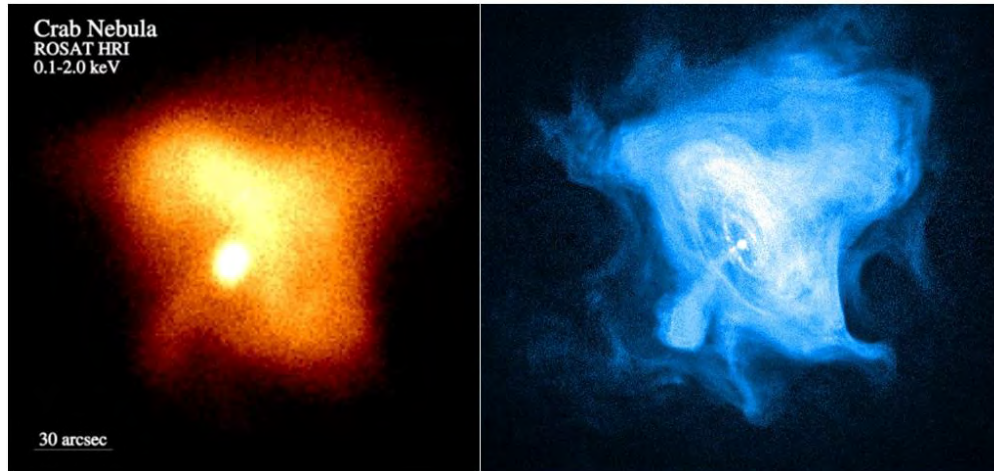


Figure 2.9. X-ray images of the Crab Nebula from (left) ROSAT and (right) Chandra. (ROSAT Credit: S.L. Snowden, NASA/GSFC. Chandra Credit: NASA/CXC/SAO)

However, the Chandra is hindered by the lack of collecting area. A proposed next generation telescope, e.g. SMART-X or X-ray Surveyor, aims to maintain the angular resolution of the Chandra while increasing the collecting area by 20-30 times. While, several approaches are being investigated concurrently, one promising method is to use adjustable optics.

The program seeks to use a thin glass mirror that can be deformed *in situ* in a predictable and reproducible way to allow correction of figure errors while the telescope is in orbit. The proposed method uses thin, slumped glass substrates which have an uncorrected angular resolution of 5-10 arcseconds. Thin films of piezoelectrics on the back apply stresses to the glass to change the shape of the mirror, creating a corrected figure with angular resolution of at least 0.5 arcseconds. The piezoelectric PZT was selected for this work for the high piezoelectric coefficients which will allow larger strains at lower operating voltages.

Previous work has demonstrated the ability to sputter deposit PZT thin films on both flat and curved (slumped along one axis to a radius of curvature of 220 mm) glass substrates. Additionally, it was shown that mathematical models fit experimental data for the glass deformations well and that the 0.5 arcsecond resolution is achievable [3].

However, the SMART-X telescope will require many large area, nested segments. As the pieces are increased in size, the number of electrical connections increases. Each top electrode will need its own individual contact as well as one of the bottom electrode. For a 40x40 array, this will require 1601 electrical connections. For decreased complexity and increased mechanical reliability, array control electronics, similar to those used for flat screen computer monitors, are proposed. This would enable a large reduction in the number of contacts needed, requiring only 81 for a 40x40 array. Due to the compatibility between PZT and ZnO demonstrated in previous sections, ZnO thin film transistors were chosen. Furthermore, PZT capacitors and ZnO TFTs have previously been demonstrated to be radiation hard and suitable for space applications [30]–[32].

2.4 Mirror Fabrication Process Flow for SMART-X

A mask layout for a 5 x 5 array of 1 cm² piezoelectric elements for a four inch substrate was designed for a proof of concept. A fully fabricated wafer is shown in Figure 2.10, demonstrating the intended design. The top down view inset shows a completed thin film transistor (TFT) as part of the array. The PZT elements are individually controlled through ZnO TFTs with W/L = 200 μm / 5 μm dimensions. The source of each TFT is connected to the top electrode of the PZT. The metal pads making this connection were designed to be relatively large to accommodate future experiments of bonding ZnO electronics on a flexible substrate to the PZT array on a curved glass substrate. The drains and gates are connected in a row/column addressing scheme so that cells can be controlled individually. For the array, the gate and drain line connections were designed to be compatible with off-the-shelf ribbon cables with 250 μm lines and 250 μm spacing. Additionally, single element addressing to make electrical contact to the PZT bypassing the TFTs was incorporated and discrete TFTs were fabricated along the sides

of the wafer for easy testing to determine properties.

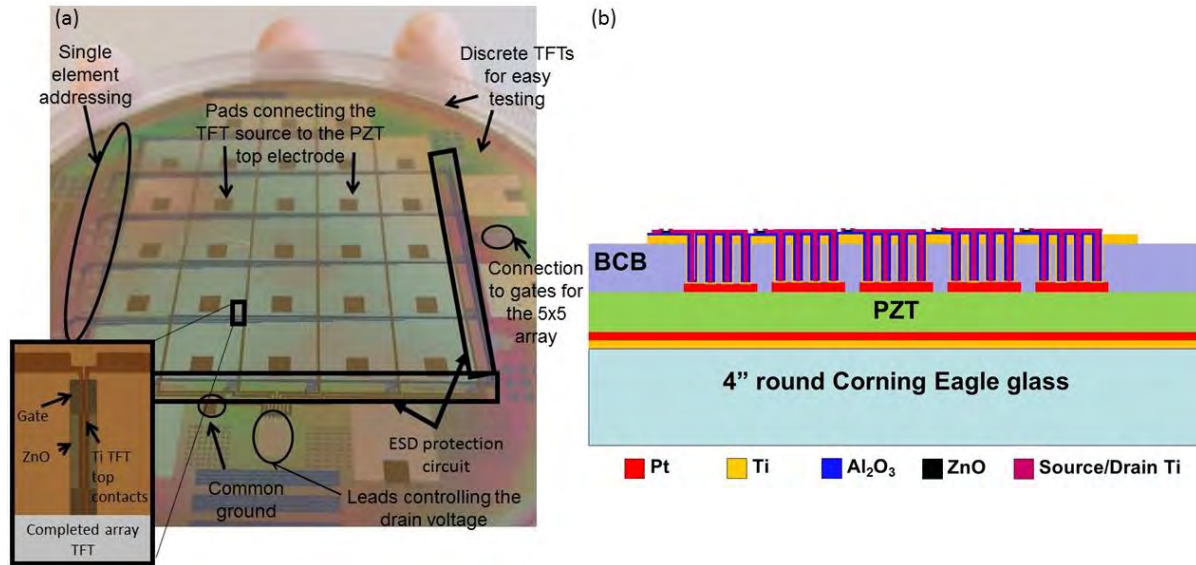


Figure 2.10. (a) Top down view of the proposed wafer structure including a close of a completed array TFT. (b) Shows the side view of the materials stack on the backside of the mirror.

A 0.4 mm thick Corning Eagle glass wafer was used as the substrate. Before processing, the wafer was cleaned by sonicating in acetone and IPA and a low power oxygen plasma etch step was performed to remove residual organics and dirt from the surface. Next, a Ti/Pt bottom electrode was sputter deposited (30 nm and 100 nm respectively) on the glass substrate. It was found that sputtering at higher temperatures, e.g. 150 °C, was necessary to increase adhesion and prevent delamination of the piezoelectric cells on subsequent steps. Figure 2.11 shows the improvement on electrode adhesion between the first and second generation pieces.

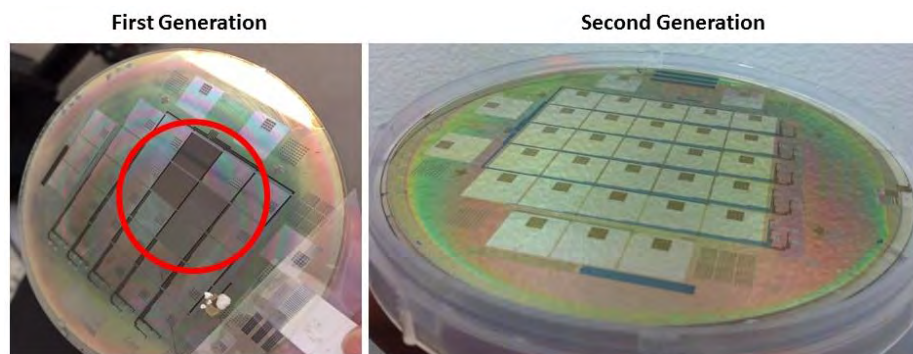


Figure 2.11. The first generation (room temperature deposition of bottom electrode) and second generation (150 °C deposition of bottom electrode) mirror pieces. While the first generation saw delamination of piezoelectric cells upon the final lift off lithography step, by increasing the temperature of deposition, better adhesion was achieved.

Following this, the PZT thin film was deposited. The sol-gel process is unsuitable for this substrate as the thin layers needed for crack-free films result in a cumbersome deposition process. As such, $\text{Pb}(\text{Zr}_{0.52}\text{Ti}_{0.48})_{0.99}\text{Nb}_{0.01}\text{O}_3$ films were sputter-deposited up to a thickness of 1.5 microns in 0.5 micron steps. The thickness of 1.5 μm was chosen as it was previously demonstrated to have suitable deflections for SMART-X requirements. The sputtering procedure is described in detail elsewhere and the sputtering parameters are shown in Table 2.2.

Table 2.2. Sputter Parameters of PZT on Glass

Parameter	Value
Target Composition	$\text{Pb}_{1.05}\text{Zr}_{0.52}\text{Ti}_{0.48}\text{O}_{3.05}$ + 1% Nb
RF Power Density	Target: 2.0 W/cm ²
Substrate Temperature	25 °C
Sputtering Gas	Ar
Working Pressure	4-5 mTorr
Deposition Time	3 x 12,500s
Thickness	3 x 0.5 μm

Post deposition, the films are amorphous and must undergo a crystallization step. However, the thermal conductivity and strain point of the glass complicates this. The post-deposition anneal was described in detail previously. For this thesis, the films on glass were

either crystallized at 585 °C for 18 hours or, for later generations, 650 °C for 1 minute.

Top Pt electrodes were then patterned via lift-off lithography and sputter-deposited. The dielectric constants measured at 100 Hz with a 30 mV ac signal ranged between 1200-1500, loss tangents were < 4%. The remanent polarizations were >24 $\mu\text{C}/\text{cm}^2$. Figure 2.12 shows the polarization versus field loops for the PZT deposited in these studies. Additionally, the wafers had high yield (>90%) on cm^2 electrodes. Often, to increase yield, a direct current (DC) voltage was applied to electrodes with high loss tangents or shorted characteristics. In such large area electrodes, the possibility of having locally defective PZT material is high. A likely source of increased leakage on an electrode is conductive PbO in grain boundaries. When a DC voltage (3 V) from two batteries in series is applied to the film for at least 5 seconds, these conductive regions see high levels of current which, due to Joule heating, vaporize the conductive defects, leaving insulating piezoelectric cells. The capacitance values can be compared to originally insulating electrodes to verify that the amount of material vaporized is small enough that it doesn't cause large portions of the electrode to be unusable. One important aspect of this technique is the use of batteries which do not have current limiting circuitry as is seen in testing equipment. Because of this, the high levels of current that are needed for vaporization of the conducting pathways can be achieved [4].

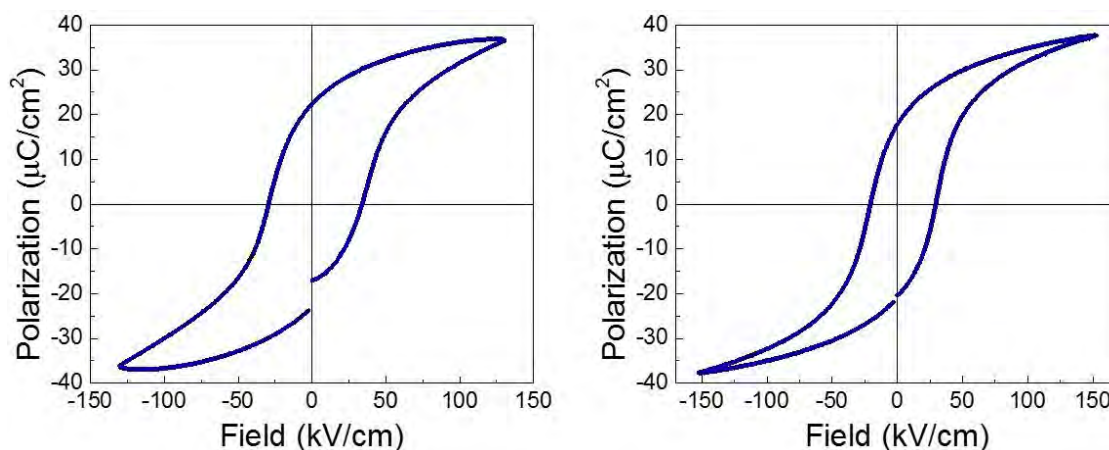


Figure 2.12. Shown here are the polarization versus field loops for films on glass used for these studies. The figure on the left was crystallized under low temperature (585 °C, 18 hours) conditions and the figure on the right was crystallized at higher temperature (650 °C, 1 min). While the low temperature conditions produced P-E loops with wider tips, both films show accepted low field remanent polarizations.

TFTs were fabricated directly on top of the PZT capacitor. In order to electrically isolate the TFT bottom gate from the PZT, photopatternable BCB 4022-35 (Dow Chemical), diluted with one part T1100 (Dow Chemical) for three parts BCB, was spun on to the wafer and dried at 60 °C for 90 seconds. The BCB had a cured thickness of 1.1 μm. Following the deposition and soft bake, BCB vias to the top electrode of the PZT were exposed using a Karl Suss MA/BA-6. After a post-exposure bake at 60 °C for 5 minutes, the pattern was developed in a 45 °C bath of DS3000 for 2 minutes. The BCB was then cured in a vacuum oven at 225 °C overnight (~12 hours) in vacuum. More detailed information on the BCB deposition process can be found in chapter 3.

The TFTs were then fabricated in a similar way as described above. The few differences in the processing will be described here. For TFTs deposited on top of BCB, Ti was used as a gate material. Cr was not used for this application as the stress of the deposited Cr was too large and would cause cracking. The cracking is believed to be from highly stressed Cr which can be slightly oxidized on the BCB, making the Cr more brittle. While chromium can be used on top of

BCB, the sputtering conditions need to be carefully controlled to avoid high stress films. Instead, Ti is recommended as it will more easily adhere to the BCB through Ti-C bonds [33]. The Ti gate is patterned on top of the BCB using lift off lithography and then 100 nm of Ti is deposited via sputtering. Typically a short oxygen plasma etch step is performed just prior to the sputtering step in order to remove any organic residue left by the photoresist. The parameters of the oxygen etch step are shown in Table 2.3. However on BCB, an oxygen plasma can oxidize the surface and thus weaken the bond between the deposited metal and the top of the BCB and so this step must be kept very short [33].

Table 2.3 Oxygen Plasma Etch Parameters

Parameter	Value
Pressure	550 mT
Oxygen Flow	150 sccm
Helium Flow	50 sccm
Power	200 W
Time	1 minute

Additionally, to promote metal adhesion, a sputter etch *in situ* was performed using an argon etch step in the sputter chamber prior to deposition. This etch step serves a dual purpose, preparing the BCB surface as well as repairing small amounts of oxidation which may have formed at the surface during the oxygen etch step. With this process, successful deposition of the gate metal on BCB is possible.

The deposition of the dielectric and semiconducting layers of the device (50 nm Al₂O₃ / 10 nm ZnO) as well as the patterning of the ZnO was performed as described previously.

However, it was found that the warm H_3PO_4 in the Al_2O_3 via etch slightly oxidized the Ti contacts. This was clear from the non-ohmic behavior measured on Ti that had been exposed to the etchant.

As such, a buffered solution of mainly tetramethylammonium hydroxide (TMAH) and water with a pH of 12 (provided by K. Sun of the Jackson group) was used instead [34]. As TMAH is the active chemical in many developers it is known to be unreactive with titanium. The etch rate of the buffered solution is extremely sensitive to both pH and temperature, so it is important for these parameters to be well controlled. For the samples fabricated in this thesis a solution temperature of $55\text{ }^\circ\text{C}$ was used. At this temperature, the etch rate of alumina is approximately 23 nm/minute.

The lift off of Ti for source/drain contacts/array leads as well as the Al_2O_3 ALD passivation deposition was not modified for this process. In this case, vias were etched into the passivating Al_2O_3 to allow electrical connection to the control electronics. For the last step in the fabrication, 75 nm chrome and 75 nm iridium films were sputter-deposited on the opposite side of the mirror to serve as a reflective coating.

Connections to the array were made using flex cables bonded to the leads using anisotropic conductive film (Hitachi 7206U). Initially, off-the-shelf ribbon cables were used, however it was found that they were too stiff and caused local stresses and, in some cases, even delamination of the materials on the wafer. As such, thin polyimide cables with sputter Cu leads were designed and fabricated to promote greater flexibility. The cables themselves were bonded to the wafer using the anisotropic conductive film (ACF). ACF is comprised of a metal/epoxy matrix which should lower any distortion the bond would exert on the wafer. A schematic of an ACF bond is shown in Figure 2.13 [35]. In essence, small (micron sized) particles generally with

a polymer core plated with nickel, gold, and finally a thin polymer, are surrounded by an epoxy matrix [35]. As heat and pressure is applied, conductive vertical pathways are formed. This provides conduction vertically but insulation laterally.

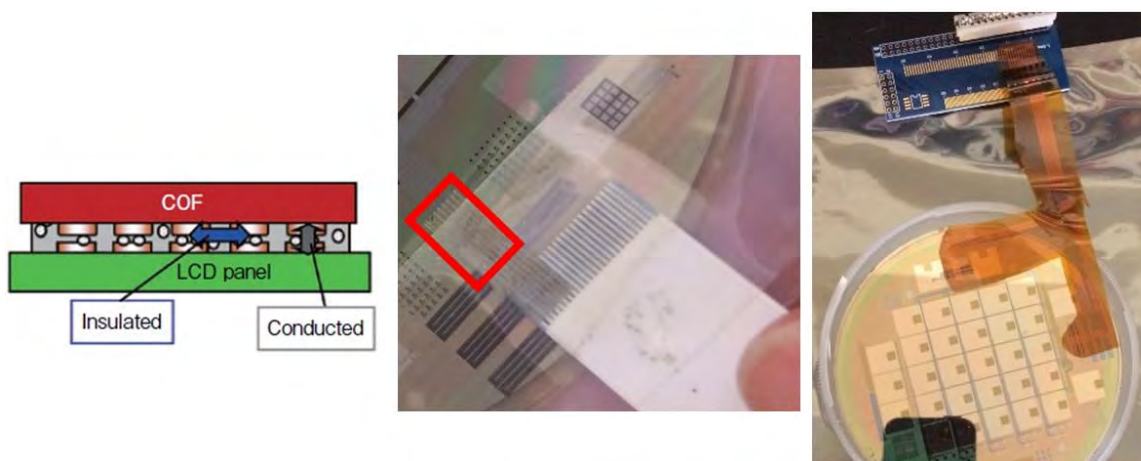


Figure 2.13. Shows (left) a schematic of and ACF bond (middle) a close up of an ACF bond on one of the SMART-X wafers and (right) a picture of the flex cables bonded to the wafer using ACF

2.4.1 Electrostatic Discharge Protection Circuit

One of the challenges faced, beyond processing, is the fact that the TFT arrays such as the ones described here are especially susceptible to electrostatic discharge (ESD) events due to the thin dielectric layer (~ 50 nm). This became a more pressing problem as flex cables were used to bond the TFTs to external power sources. This configuration made it more difficult to keep the sample properly grounded, especially as not all measurements were made in grounded probe stations. While preventive, off-chip, procedures were set in place to minimize ESD-induced damage, these procedures were not sufficient to prevent damage to the ZnO electronics. Protecting for ESD is an important concern as it is believed to be the cause of TFT breakdown post fabrication. Thus, an ESD protection circuit was designed and integrated into the process flow to fully protect the array TFTs.

The on-chip ESD-protective circuitry was designed for each gate and drain line of the array to prevent damage or malfunction of the ZnO TFTs addressing each PZT pixel.

The purpose of the ESD protection circuit is to automatically create a shunting path to safely discharge static electricity. A common ESD protection circuit used in display arrays has two diode-connected TFTs, in parallel, connected between a drain/gate line and a common potential ring. The ESD-protection circuit is designed to have low impedance in the case of an ESD event compared to other possible current paths (array) and high impedance during normal array operation.

The ESD protection circuit for the samples in this thesis was designed by J. I. Ramirez and is described in detail in his thesis [36].

2.5 Influence Function Measurements

Completed samples were taken to the Smithsonian Astrophysical Observatory (SAO) for testing. A Shack-Hartmann wave-front sensor (WFS) was used for the influence function measurements. The WFS uses a red laser which is collimated just before the mirror. The reflected plane wave carries information about the shape of the imaged mirror. A measurement is made at voltage and prior to voltage application. Subtracting the two images provides the influence function. Additionally, the wave front sensor enables a sensitive measurement of the deformation of the surface of the entire wafer on a short time scale (~ 10 sec/measurement). The wafer was bonded to a 6 point flexure mount which ensures identical mechanical boundary constraints on measurements of different wafers.

The PZT was poled at one times the coercive voltage (5 V) for fifteen minutes, via the individual contact pads directly addressing the PZT cell. A less aggressive poling procedure was

used for this film as, reported previously, the cross sections showed increased levels of porosity. The porosity likely affects the leakage current as a function of time and so a careful poling procedure was employed to reduce the likelihood of catastrophic breakdown. Additionally, as will be shown in chapter 3, domain alignment is facilitated both by porosity [37] and substrates with low elastic moduli, like the one used here.

The surface shape was measured as certain PZT cells were turned on and off either with the TFT array or bypassing the TFT array and actuating the PZT cell directly. Immediately prior to a measurement where the PZT is actuated, a reference image was taken. Unfortunately, during the process of bonding the mirror to the 6 point flexure mount at SAO, a piece of the wafer was broken off and so the full wafer could not be measured. As a consequence, the wafer was only bonded in four places to the mount. Figure 2.14 shows the influence function of the wafer with no PZT cells actuated, along with an approximate map of the PZT labeled numerically.

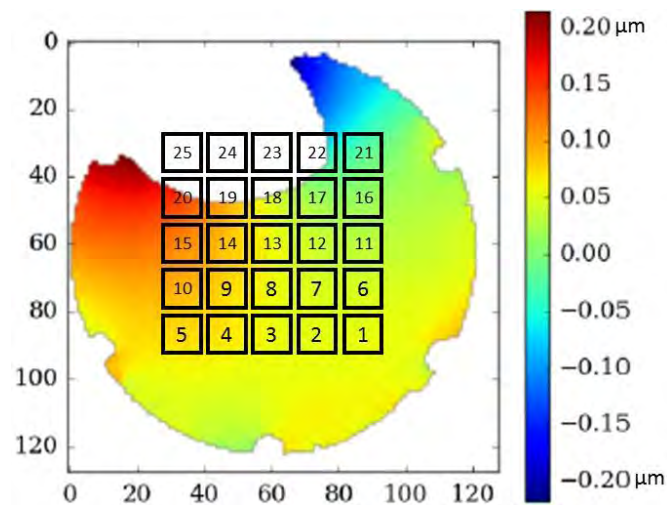


Figure 2.14. The influence function of the wafer with no PZT cells actuated. The PZT cells are outlined in black and numbered according to how they are referenced in the text.

Figure 2.15 shows the influence function of the wafer as the five cells along the bottom row are actuated one at a time at 5 V. It is clear that different regions of the wafer are actuated as

different cells are turned on. It is noted that the amount of deformation is not limited to the immediate area around the actuated cell. Several cells were electrically connected to each other and thus it was impossible to actuate one without also actuating certain other cells. For example, when 5 V was applied to cell 1, approximately 0.686 V was measured on cells 11 and 14. That these two cells were actuated is readily apparent in the influence function seen in Figure 2.15. The unintentional actuation near cell 14 has smaller deflections, spread out over a larger region due to the proximity to the broken edge of the wafer. The region around cell 11 shows a high level of deflection when cell 1 was actuated; this increased deformation is likely due to the wafer being freer to strain in the area around the break.

The cause of the electrical cross-talk is not known, but there are two likely possibilities. First, the electrical connections between cells in the array could be due to processing errors, as 100% yield samples are difficult to fabricate in university cleanroom conditions. A second possibility is that an electrostatic discharge (ESD) event may have occurred when the wafer was broken. While an ESD protection circuit was employed, it was meant to protect the TFTs from high voltage coming from the flex cables. The region where the break occurred was on the other side of the ESD circuit and thus interacted with TFTs before seeing the protection circuit. As such, the TFTs were not protected and may have exposed the TFTs to high voltage during the breakage. However, it is still clear that the shape of the mirror could be successfully modulated upon actuation. Furthermore, the TFTs can be turned on and off.

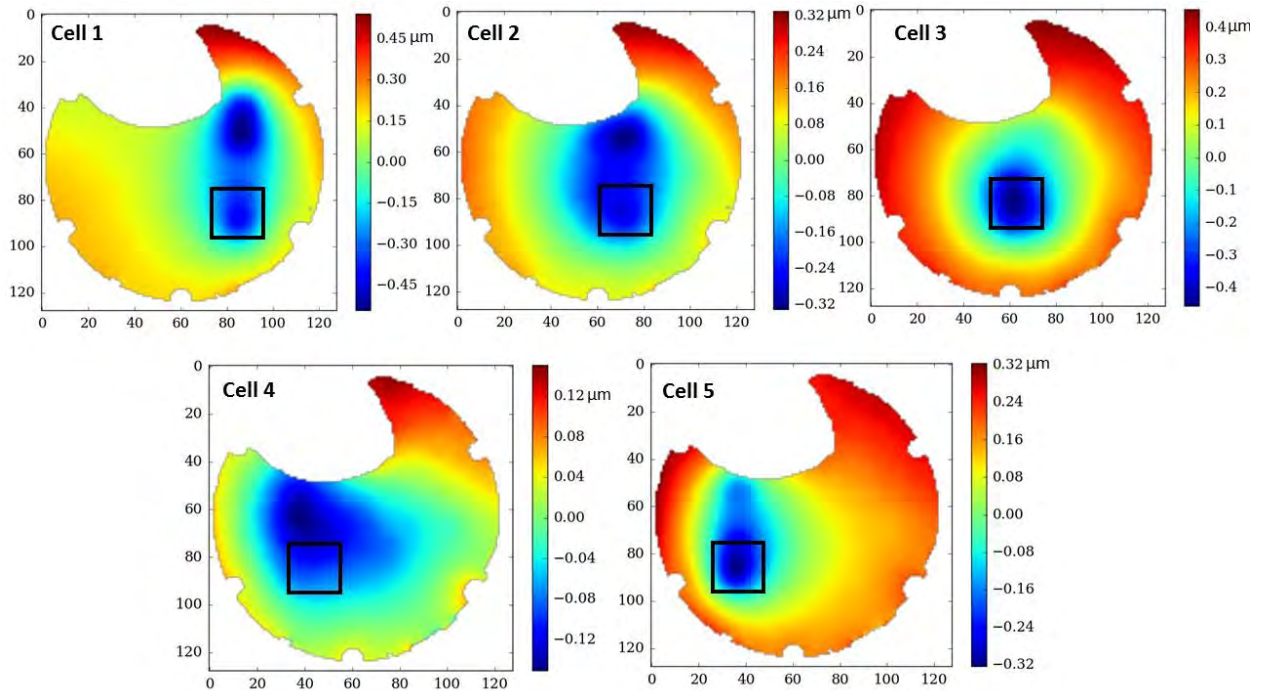


Figure 2.15. The influence functions of the wafer as different PZT cells are actuated at 5 V. While the deflection of the wafer is not limited to the region directly adjacent to the actuated cell, it is clear that different areas of the wafer could be addressed and actuated. The actuated cells are outlined in black.

The wafer shape was investigated as the PZT was actuated either using the TFT array or directly using contact pads fabricated on the side of the wafer. It was found that while the general shape of the wafer deflection was similar, the absolute magnitude of the deflection differed slightly in regions away from the actuated cell. This was found to be due to a difference in the voltage that was measured on cells that were not intentionally actuated, but which were weakly electrically connected to the actuated cell. For instance, when cell 1 was actuated at 5 V, the electrically connected cells (11 and 14) saw 0.686 V when actuated through the TFT array and only 0.3 V when actuated through the contact pads. This may be due a difference in the resistivities between cells depending on which direction the voltage comes from (through the array or from the PZT cell). However, it is important to note that actuation voltage applied to cell 1 was the same in both cases. Considering both this and the fact that the influence functions

show very similar amounts of deflection, it is expected that without defects in the TFT array the wafer would show the same levels of deflection whether actuation is performed either through the TFTs or directly. Figure 2.16 shows the influence functions for the cell actuated directly and through the TFT.

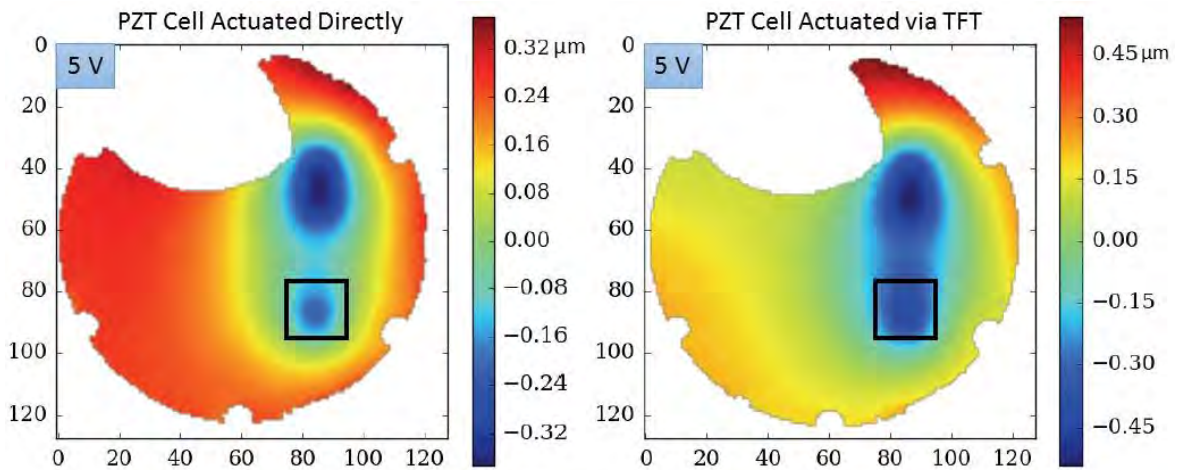


Figure 2.16. The influence functions for the cell actuated directly (left) and through the TFT (right). The actuated cell is outlined in black.

Finally, it was demonstrated that the magnitude of the deflection is controllable via the amount of voltage applied through the TFT. Figure 2.17 shows the influence functions for the wafer as the actuation voltage applied to one cell through the TFT was stepped up progressively.

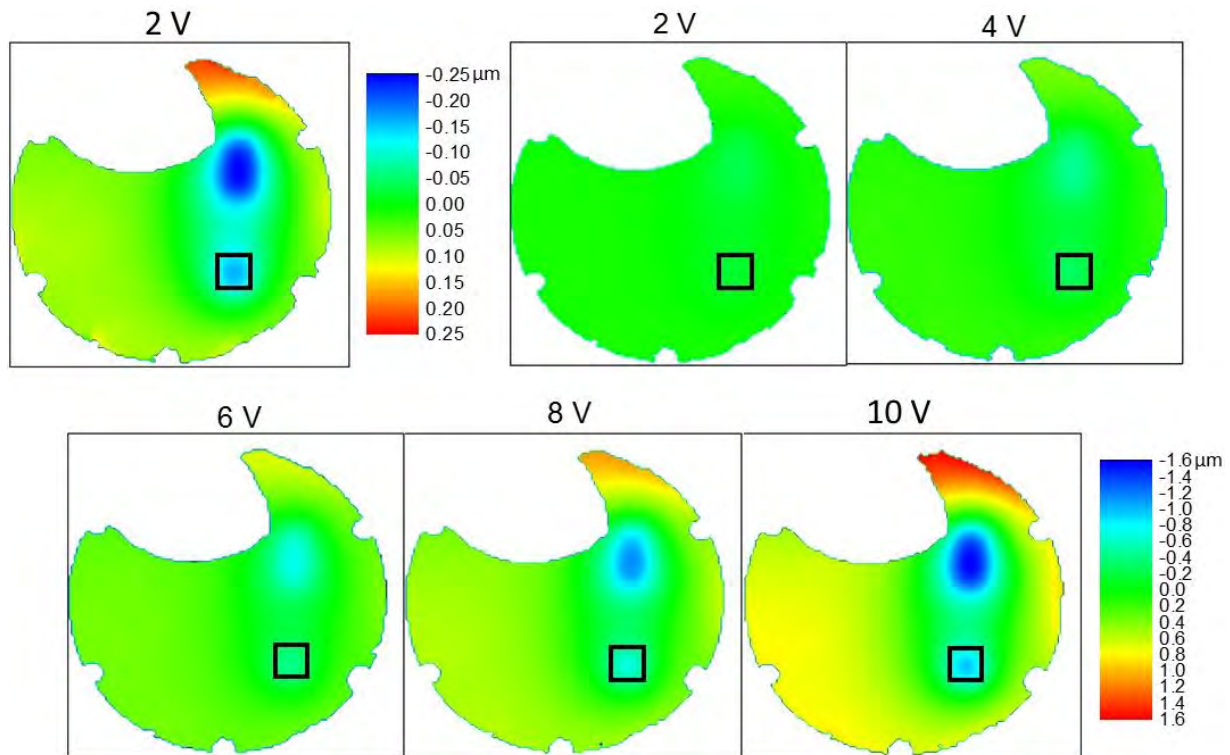


Figure 2.17. Shape change as the voltage is modulated from 2 V to 10 V for a single cell (cell 1). To show increased levels of deflection with voltage, the influence functions are shown plotted with the same scale. The first image shows the 2 V actuation on a separate scale to demonstrate the wafer does change shape even at these low voltages.

The wafer shows a systematic increase in the deformation as the applied voltage increased. The out-of-plane deflection was approximately $1.5 \mu\text{m}$ for every 10 V applied, as shown in Figure 2.18. This is slightly higher than the deflection measured on samples without ZnO TFTs ($\sim 1 \mu\text{m}/10 \text{ V}$) [3]. The likely reason for this discrepancy is that in the case presented here, multiple TFTs are actuated at once. As shown in work by Wilke *et al.*, when two electrodes located next to each other are actuated simultaneously, a larger deflection ($\sim 1.2 \mu\text{m}/10\text{V}$) is measured [3].

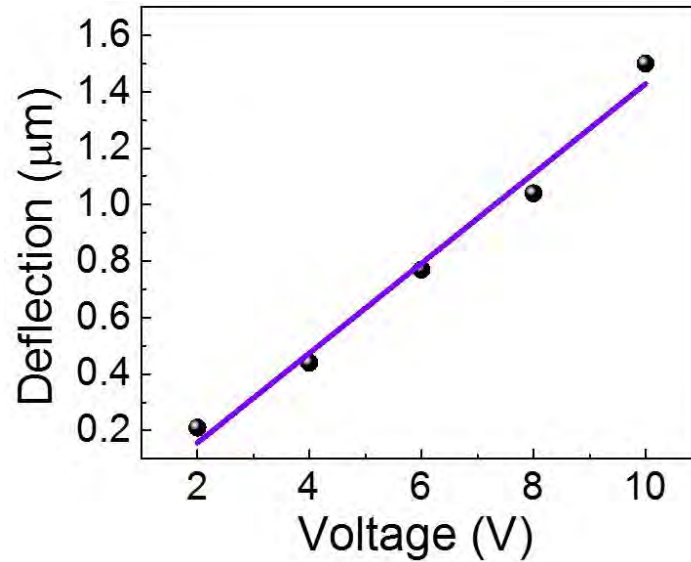


Figure 2.18. The deflection of the actuated cell as a function of voltage. The slope indicates $\sim 1.5 \mu\text{m}$ deflection for 10 V applied.

2.6 Conclusions

In conclusion, it was demonstrated that PZT MEMS structures could be successfully coprocessed and controlled by ZnO electronics. In particular, the ZnO electronics were shown to be a useful method for controlling piezoelectric deflection in adaptive optics. While the mirrors used for this demonstration show some weak electrical connection between cells, the mirror could be controlled by the PZT cells using the ZnO TFT for addressing. The amount of deflection and the area of the wafer deformed are both controllable via the TFT. This integration is expected to be applicable to other technologies such as transducer or sensor arrays or active rectification for mechanical energy harvesting.

2.7 References

- [1] P. Muralt, “Ferroelectric Thin Films for Micro-Sensors and Actuators: A Review,” *J. Micromechanics Microengineering*, vol. 10, p. 136, 2000.
- [2] G. L. Smith, J. S. Pulskamp, L. M. Sanchez, D. M. Potrepka, R. M. Proie, T. G. Ivanov, R. Q. Rudy, W. D. Nothwang, S. S. Bedair, C. D. Meyer, and R. G. Polcawich, “PZT-Based Piezoelectric MEMS Technology,” *J. Am. Ceram. Soc.*, vol. 95, no. 6, pp. 1777–1792, 2012.
- [3] R. H. T. Wilke, R. L. Johnson-Wilke, V. Cotroneo, S. Mcmudroch, P. B. Reid, D. A. Schwartz, and S. Trolier-McKinstry, “Fabrication of Adjustable Cylindrical Mirror Segments for the SMART-X Telescope,” *IEEE Trans. Ultrason. Ferroelectr. Freq. Control*, vol. 61, no. 8, pp. 1386–1392, 2014.
- [4] R. L. Johnson-Wilke, R. H. T. Wilke, V. Cotroneo, W. N. Davis, P. B. Reid, D. A. Schwartz, and S. Trolier-McKinstry, “Improving Yield of PZT Piezoelectric Devices on Glass Substrates,” *SPIE Proc.* vol. 8503, p. 85030A, 2012.
- [5] D. L. Polla and L. F. Francis, “Processing and Characterization of Piezoelectric Materials and,” *Annu. Rev. Mater. Sci.*, vol. 28, no. 1, pp. 563–597, 1998.
- [6] Y. Kato, T. Sekitani, Y. Noguchi, T. Yokota, M. Takamiya, T. Sakurai, and T. Someya, “Large-Area Flexible Ultrasonic Imaging System with an Organic Transistor Active Matrix,” *IEEE Trans. Electron Devices*, vol. 57, no. 5, pp. 995–1002, 2010.
- [7] A. Wung, R. V. Park, K. J. Rebello, and G. K. Fedder, “Tri-Axial High-G CMOS-MEMS Capacitive Accelerometer Array,” *Proc. IEEE Int. Conf. Micro Electro Mech. Syst.*, pp. 876–879, 2008.
- [8] A. Witvrouw, F. Van Steenkiste, D. Maes, L. Haspeslagh, P. Van Gerwen, P. De Moor, S. Sedky, C. Van Hoof, A. C. de Vries, A. Verbist, A. De Caussemaeker, B. Parmentier, and K. Baert, “Why CMOS-Integrated Transducers? A Review,” *Microsyst. Technol.*, vol. 6, no. 5, pp. 192–199, 2000.
- [9] A. J. Fleming and Y. K. Yong, “Thermal Analysis of Piezoelectric Benders with Laminated Power Electronics,” *2013 IEEE/ASME Int. Conf. Adv. Intell. Mechatronics Mechatronics Hum. Wellbeing, AIM 2013*, pp. 83–88, 2013.
- [10] T. Ji, M. Kathiresan, S. Nair, S. Jung, V. Natarajan, R. M. R. Vishnubhatla, and V. K. Varadan, “Design and Fabrication of OTFT Based Flexible Piezoelectric Sensor,” *Nanosensors, Microsens. Biosens. Syst.*, vol. 6528, no. 2007, p. 65281P–6, 2007.
- [11] D. L. Polla and P. J. Schiller, “Integrated Ferroelectric Microelectromechanical Systems (MEMS),” *Integr. Ferroelectr.*, vol. 7, no. 1–4, pp. 359–370, 1995.

- [12] Y. Kaneko, Y. Nishitani, H. Tanaka, M. Ueda, Y. Kato, E. Tokumitsu, and E. Fujii, "Correlated Motion Dynamics of Electron Channels and Domain Walls in a Ferroelectric-Gate Thin-Film Transistor Consisting of a ZnO/Pb(Zr,Ti)O₃ Stacked Structure," *J. Appl. Phys.*, vol. 110, no. 084106, pp. 1–7, 2011.
- [13] F. Saharil, R. V. Wright, P. Rantakari, P. B. Kirby, T. Vähä-Heikkilä, F. Niklaus, G. Stemme, and J. Oberhammer, "Low-Temperature CMOS-Compatible 3D-Integration of Monocrystalline-Silicon Based PZT RF MEMS Switch Actuators on RF Substrates," *Proc. IEEE Int. Conf. Micro Electro Mech. Syst.*, pp. 47–50, 2010.
- [14] K. Rho, S. Zurn, D. Markus, and D. L. Polla, "Integration of a CMOS Preamplifier with a Lead Zirconate Titanate Resonant Frequency Microsensor," *J. Electrochem. Soc.*, vol. 149, no. 7, p. J53, 2002.
- [15] P. K. Leung and I. T. Emesh, "Method of Adding on Chip Capacitors to an Integrated Circuit," US Patent Number 5789303, 1998.
- [16] Y. Fukuda, K. Aoki, A. Nishimura, and K. Numata, "Capacitor, Electrode Structure, and Semiconductor Memory Device," US Patent Number 5508953, 1996.
- [17] S. Ma, G. W. Ray, and F. Eschbach, "Three-Dimensional Ferroelectric Capacitor Structure for Nonvolatile Random Access Memory Cell," US Patent 6281535, 2001.
- [18] H. Kim, F. Griggio, I. S. Kim, K. Choi, R. L. Tutwiler, T. N. Jackson, and S. Trolier-McKinstry, "Piezoelectric Thin Films for a High Frequency Ultrasound Transducer with Integrated Electronics," *Sensors, 2010 IEEE*, pp. 2186–2188, 2010.
- [19] E. S. Kolesar and C. S. Dyson, "Object Imaging with a Piezoelectric Robotic Tactile Sensor," *J. Microelectromechanical Syst.*, vol. 4, no. 2, pp. 87–96, 1995.
- [20] T. Yokota, T. Sekitani, T. Tokuhara, N. Take, U. Zschieschang, H. Klauk, K. Takimiya, T. C. Huang, M. Takamiya, T. Sakurai, and T. Someya, "Sheet-Type Flexible Organic Active Matrix Amplifier System Using Pseudo-CMOS Circuits with Floating-Gate Structure," *IEEE Trans. Electron Devices*, vol. 59, no. 12, pp. 3434–3441, 2012.
- [21] E. E. Aktakka, R. L. Peterson, and K. Najafi, "A CMOS-Compatible Piezoelectric Vibration Energy Scavenger Based on the Integration of Bulk PZT Films on Silicon," *Tech. Dig. - Int. Electron Devices Meet. IEDM*, no. 2, pp. 716–719, 2010.
- [22] R. E. Davidsen and S. W. Smith, "Two-Dimensional Arrays for Medical Ultrasound Using Multilayer Flexible Circuit Interconnection," *IEEE Trans. Ultrason. Ferroelectr. Freq. Control*, vol. 45, no. 2, pp. 338–348, 1998.
- [23] R. G. Swartz and J. D. Plummer, "Integrated Silicon-PVF₂ Acoustic Transducer Arrays," *IEEE Trans. Electron Devices*, vol. ED-26, no. 12, pp. 1921–1931, 1979.

- [24] Y.J. Hsu, Z. Jia, and I. Kymissis, "A Locally Amplified Strain Sensor Based on a Piezoelectric Polymer and Organic Field-Effect Transistors," *IEEE Trans. Electron Devices*, vol. 58, no. 3, pp. 910–917, 2011.
- [25] I. Kim, H. Kim, F. Griggio, R. L. Tutwiler, T. N. Jackson, S. Trolrier-McKinstry, and K. Choi, "CMOS Ultrasound Transceiver Chip for High-Resolution Ultrasonic Imaging Systems," *IEEE Trans. Biomed. Circuits Syst.*, vol. 3, no. 5, pp. 293–303, 2009.
- [26] D. A. Mourey, D. A. Zhao, J. Sun, T. N. Jackson, "Fast PEALD ZnO Thin-Film Transistor Circuits," *IEEE Trans. Electron Devices*, vol. 57, no. 2, pp. 530–534, 2010.
- [27] D. A. Schwartz, T. L. Aldcroft, J. A. Bookbinder, V. Cotroneo, W. N. Davis, W. R. Forman, M. D. Freeman, S. McMuldloch, P. Reid, H. Tananbaum, A. Vikhlinin, S. Trolrier-McKinstry, D. Wilke, and R. Johnson-Wilke, "The Square Meter Arcsecond Resolution X-ray Telescope: SMART-X," *SPIE Proc.* vol. 8503, p. 850308, 2012.
- [28] S. O'Dell, C. Atkins, T. Button, V. Cotroneo, W. Davis, A. Doel, C. Feldman, M. Freeman, M. Gubarev, J. Kolodziejczak, A. Michette, B. Ramsey, P. Reid, D. Rodriguez Sanmartin, T. Saha, D. Schwartz, S. Trolrier-McKinstry, R. Wilke, R. Willingale, and W. Zhang, "Towards Active X-ray Telescopes," *SPIE Proc.* vol. 8147, pp. 1–18, 2011.
- [29] S. Aggarwal, S. R. Perusse, C. J. Kerr, R. Ramesh, D. B. Romero, J. T. Evans, L. Boyer, and G. Velasquez, "Recovery of Forming Gas Damaged Pb(Nb, Zr, Ti)O₃ Capacitors," *Appl. Phys. Lett.*, vol. 76, no. 7, p. 918, 2000.
- [30] R. H. T. Wilke, R. L. Johnson-Wilke, V. Cotroneo, W. N. Davis, P. B. Reid, D. a Schwartz, and S. Trolrier-McKinstry, "Sputter Deposition of PZT Piezoelectric Films on Thin Glass Substrates for Adjustable X-ray Optics," *Appl. Opt.*, vol. 52, no. 14, pp. 3412–9, 2013.
- [31] Y. M. Coic, O. Musseau, and J. L. Leray, "A Study of Radiation Vulnerability of Ferroelectric Material and Devices," *IEEE Trans. Nucl. Sci.*, vol. 41, no. 3, pp. 495–502, 1994.
- [32] J. I. Ramirez, Y. V Li, H. Basantani, K. Leedy, B. Bayraktaroglu, G. H. Jessen, and T. N. Jackson, "Radiation-Hard ZnO Thin Film Transistors," *IEEE Trans. Nucl. Sci.*, vol. 62, no. 3, pp. 1399–1404, 2015.
- [33] Dow Chemical, "Processing Procedures for BCB Adhesion," 2007.
- [34] K. G. Sun, Y. V. Li, D. B. Saint John, and T. N. Jackson, "pH-Controlled Selective Etching of Al₂O₃ over ZnO," *ACS Appl. Mater. Interfaces*, vol. 6, no. 10, pp. 7028–7031, 2014.
- [35] N. Takano, "Film Technologies for Semiconductor & Electronic Components," no. 55, pp. 20–23, 1990.

- [36] J. I. Ramirez, "ZnO Thin Film Electronics For More Than Displays," Ph. D. Thesis in Electrical Engineering, The Pennsylvania State University, 2015.
- [37] R. L. Johnson-Wilke, R. H. T. Wilke, M. Wallace, A. Rajashekhar, G. Esteves, Z. Merritt, J. L. Jones, and S. Trolier-McKinstry, "Ferroelectric / Ferroelastic Domain Wall Motion in Dense and Porous Tetragonal Lead Zirconate Titanate Films," *IEEE Trans. Ultrason. Ferroelectr. Freq. Control*, vol. 62, no. 1, pp. 46–55, 2015.

Chapter 3. Direct Measurements of 90° Domain Reorientation in Thin Film PZT as a Function of the Substrate

3.1 Measurement of Domain Wall Motion in Declamped PZT Thin Films

Portions of this chapter are reproduced from: M. Wallace, R. L. Johnson-Wilke, G. Esteves, C. M. Fancher, R. H. T. Wilke, J. L. Jones, and S. Trolier-McKinstry, “*In situ* measurement of increased ferroelectric/ferroelastic domain wall motion in declamped tetragonal lead zirconate titanate thin films.” *J. Appl. Phys.* **117** [5] 054103 (2015).

Reprinted with permission

3.1.1 Introduction to Clamping of Domain Walls in Thin Films

Piezoelectric thin films are an area of great interest for transducers, energy harvesters, gyroscopes, actuators and switches in microelectromechanical systems (MEMS) [1], [2]. $\text{Pb}(\text{Zr}_x\text{Ti}_{1-x})\text{O}_3$, PZT, is often used for such applications due to its high piezoelectric constants and enhanced sensing and actuating capabilities relative to other common piezoelectrics such as $\text{Al}_{1-x}\text{Sc}_x\text{N}$ and ZnO [2]. However, ferroelectric thin films such as PZT generally possess lower piezoelectric coefficients than their bulk counterparts. It has been proposed that the inferior properties in films are due to a combination of a clamping effect from the substrate, limited domain wall mobility, high point and line defect concentrations, large residual stresses, and small grain sizes [3]–[10]. Understanding the relative importance of different factors controlling the piezoelectric responses of PZT thin films is imperative in producing optimized devices and generating better predictive models.

In ferroelectric ceramics, there are two main contributions to the dielectric and piezoelectric coefficients: an intrinsic contribution (which describes the contribution of the lattice) and an extrinsic contribution (primarily due to domain wall motion). In bulk, polycrystalline PZT, up to 50% of the measured piezoelectric and dielectric coefficients at room

temperature are due to extrinsic domain wall contributions [11]. These extrinsic domain wall contributions are generally dominated by motion of non-180° domain walls accompanied by ferroelectric/ferroelastic distortion, although in principle 180° domain walls can also contribute [12]. However, both families of walls can be pinned by a variety of sources, such as point defects, defect dipoles, grain boundaries and film/surface interface features [13]. The collection of pinning sources is a strong function of the processing and the mechanical boundary conditions, and cannot be expected to be equivalent for thin film and bulk samples [3]–[8].

Generally, non-180° domain wall motion is reduced in films relative to bulk ceramics of the same composition [3], [8], [14]–[17] due to substrate clamping. However, when the influence of the substrate is reduced or eliminated, increased domain wall mobility is observed. Significant mobility of domain walls has been reported in piezoelectric islands [18], [19], and in some bilayers [20]. By patterning PZT into small islands (with a lateral dimension on the order of the thickness of the film) or depositing in bilayers, the material is partially declamped from the substrate. This increases the piezoelectric constant either by eliminating *a*-domains (for which the polarization is in-plane) or by facilitating domain wall motion via a reduction in pinning associated with the substrate. Lee *et al.* demonstrated via X-ray diffraction (XRD) that the patterning of islands has the ability to change the *c*-domain abundance [21].

Previously, 90° domain wall motion has been investigated in tetragonal thin films of PZT. Studies found that grain size is an important factor affecting domain wall mobility [3], [7], [9]. With increasing grain size, higher piezoelectric coefficients were observed due to reduced pinning from grain boundaries [9]. 90° domain walls are especially difficult to mobilize for films deposited on silicon with small grain sizes ($< 1 \mu\text{m}$), particularly when compared to ceramics [7]. Xu *et al.* found that ferroelectric/ferroelastic wall motion was constrained in thin, fine grained

films, but thicker films ($> 2 \mu\text{m}$), exhibited more non- 180° domain wall motion after a certain poling voltage, specific to the thickness [3]. Using XRD, Kohli *et al.* (in an *ex situ* study) and Eatough *et al.* (in an *in situ* study) investigated the domain reorientation of 90° domain walls with applied voltage and found that with increasing voltage, $00l$ type domains are preferred, thus reducing the overall volume fraction of $h00$ domains [7], [17]. Work on characterizing domain reorientation using *in situ* X-ray synchrotron techniques has also been done by Morioka *et al.* on epitaxial $\text{Pb}(\text{Zr}_{0.43}\text{Ti}_{0.57})\text{O}_3$ films. The study demonstrated that 90° switching occurred in the films, thereby increasing the remanent polarization and piezoelectric response [22]. Although it is established that these reorientations take place, the formation of c -domains and the switching as a function of voltage is limited for films on silicon substrates due to thermal expansion stresses and substrate clamping effects [16], [17], [23], [24]. XRD has also been used previously to study domain reorientation in porous versus dense tetragonal PZT thin films [25]. It was found that $\sim 3\text{-}4\%$ volume porosity increased domain reorientation in the film by more than a factor of three. The increase in domain wall mobility is attributed to one or both of the following mechanisms: 1) reduction in stiffness due to porosity, which essentially reduced the clamping effect or 2) a local enhancement of the electric field near the pores [25].

Griggio *et al.* demonstrated that by locally declamping the film from the substrate through the use of diaphragm structures, an increase in the piezoelectric response in the released region was observed. This increase was attributed, in part, to increased ferroelectric/ferroelastic domain wall motion. Rayleigh data comparing clamped and released films showed up to a 75% increase in the irreversible Rayleigh coefficient, indicating the existence of irreversible domain wall motion in the diaphragm structures. Upon breaking the diaphragms, the average, global, tensile stress of the film was eliminated and a further increase in the dielectric nonlinearity was

observed [4]. In this case, the Rayleigh coefficients approached values similar to those of bulk PZT ceramics, which suggests a reduction in barrier height for pinning centers or a change in domain wall density. In Griggio's work, the type of domain walls (ferroelectric/ferroelastic or only ferroelectric) that contributed to the nonlinearity was not determined and thus no quantitative assessments of ferroelectric/ferroelastic domain wall mobility was reported.

Other experiments have been performed in an effort to examine domain wall motion under conditions utilizing the direct piezoelectric effect and different results are reported. Shepard *et al.* monitored the relative permittivity as a function of applied compressive and tensile stress on $\text{Pb}(\text{Zr}_{0.52}\text{Ti}_{0.48})\text{O}_3$ thin films. Small, reversible changes in the transverse piezoelectric coefficient were identified as a function of the applied pressure, indicating at most modest irreversible domain wall motion [26]. Zednik *et al.*, however, demonstrated that a finite volume fraction of ferroelectric/ferroelastic domain switching could be induced under applied stress [13].

In this chapter, *in situ* XRD was used to quantify 90° domain reorientation as a function of mechanical boundary constraints. A direct measure of domain reorientation is extremely valuable for understanding which population of domain walls contributes to the nonlinearity of PZT films. For instance, in MEMS actuators using the converse piezoelectric effect, knowledge of domain reorientation would allow designers to understand the field dependence of the strain. Synchrotron x-ray diffraction techniques have been a useful tool in characterizing domain wall motion in bulk PZT ceramics and thin films [16], [27], [28]. XRD probes the volume fraction of domains of different orientations and can therefore be sensitive to the changes in orientation upon actuation. This technique has been used in the past to measure changes in peak intensities in films clamped to the substrate [3], [7], [17], [25]. Typical values for volume fraction of

reoriented domains as a function of electrical poling in bulk, polycrystalline PZT samples are 15 - 25% [27]. This present study provides a quantitative, direct measurement of how the mobility of ferroelectric/ferroelastic domain walls changes as a function of boundary condition to confirm conclusions drawn in previous studies regarding the effect of substrate clamping. It was found that upon declamping the film from the substrate, a systematic increase in the amount of 90° domain reorientation was observed for increasing released states. The volume fraction of 90° domains that switched approached the values of bulk PZT of similar compositions [27], [28].

3.1.2 Processing Declamped Films

Thin Film Fabrication

A 1.9 μm thick film of chemical solution deposited (CSD) $\text{PbZr}_{0.30}\text{Ti}_{0.70}\text{O}_3$ (PZT 30/70) doped with 1% Mn was used for this study. While manganese limits domain wall mobility due to the formation of defect dipoles ($Mn'_{Ti} - V_o''$) which act as pinning centers [29], they also potentially reduce the likelihood of oxygen vacancy migration, leading to increased lifetime [30]. The 30/70 composition was chosen to ensure the film was tetragonal and that only 90° and 180° domain walls were present. Additionally, symmetry related reflections in the 30/70 composition (e.g. 002/200) are far enough apart in order to quantitatively fit the diffraction data with good confidence. Clean fitting of multiple peaks in the diffraction data for 52/48 films was not possible, even when the films were deposited Zr/Ti gradient free.

The LaNiO_3 (LNO) bottom electrode was deposited on a thermally oxidized silicon substrate (NOVA Electronic Materials) via CSD. The thickness of the SiO_2 layer was 1 μm . The LaNiO_3 solution was made as described in Chapter 3 of this thesis. Since none of the components are moisture sensitive, the dehydration of powder precursors was skipped. In this case, a 0.2 M solution was utilized to prepare a layer approximately 20 nm thick when spun at

3000 rpm, resulting in highly {100} oriented bottom electrodes [31]. Since the conductivity of LNO changes as a function of thickness [32], the process was repeated until the LNO was ~ 170 nm thick, enabling an electrical resistivity $< 2 \text{ m}\Omega \text{ cm}$ [32].

Following this, a 0.55 M PZT 30/70 solution doped with 1% Mn and containing 10% excess PbO (synthesized using a similar process to the LNO) was spin coated onto the LNO/SiO₂/Si stack. Just prior to spinning, 7 vol% acetic acid was added and homogeneously mixed into the solution to reduce the likelihood of precipitation during deposition. After spinning a layer of solution at 1500 rpm for 45 seconds, the film was heat-treated at 250 °C for 5 minutes followed by 400 °C for 5 minutes. The long pyrolysis steps were utilized to grow high-density films of this composition. The films were then crystallized at 650 °C for 1 minute in flowing oxygen in an RTA. The annealed thickness of each PZT layer was approximately 120 nm, and the process was repeated until the films were ~1.9 μm thick to ensure an adequate volume of irradiated film material during the XRD measurements.

A pattern of top electrodes was defined photolithographically. The platinum electrodes were deposited at room temperature onto the PZT using RF magnetron sputtering. The 1.5 mm x 10 mm electrodes were designed to rotated 15° from the {001} crystallographic plane of the silicon. This orientation reduced the possibility of observing diffraction from the substrate during the XRD measurements. Additionally, each electrode had a contact pad offset from the electrode for the probe to make electrical contact so that the measurements were free of diffraction from the tungsten probe tip.

Structural and Electrical Characterization

A lab source diffractometer (PANalytical X'Pert Pro MPD) was used to determine the phase and preferred orientation of the films. The film was verified to be predominately {001}

textured, as shown in Figure 3.1, with a Lotgering factor of 97%. Field-emission scanning electron microscope (FESEM) images of the plan view and cross section of the sample show the film to be crack-free and dense (Figure 3.1). High contrast in the FESEM images was beneficial in showing porosity which, in lower contrast images, was more difficult to see. Prior to diffraction experiments, the electrical properties of the films were tested. The film exhibited a saturated PE-loop (measured with a Radiant Precision Ferroelectric Tester) with a remanent polarization $>23 \mu\text{C}/\text{cm}^2$. The dielectric constant was 475 with a loss of 0.013 (at 100 Hz and 30 mV measured with a Hewlett Packard 4284A LCR meter). The as-deposited films had a leakage current density $<10^{-7} \text{ A}/\text{cm}^2$ at three times the coercive voltage ($V_c = 12 \text{ V}$, $E_c = 63 \text{ kV}/\text{cm}$).

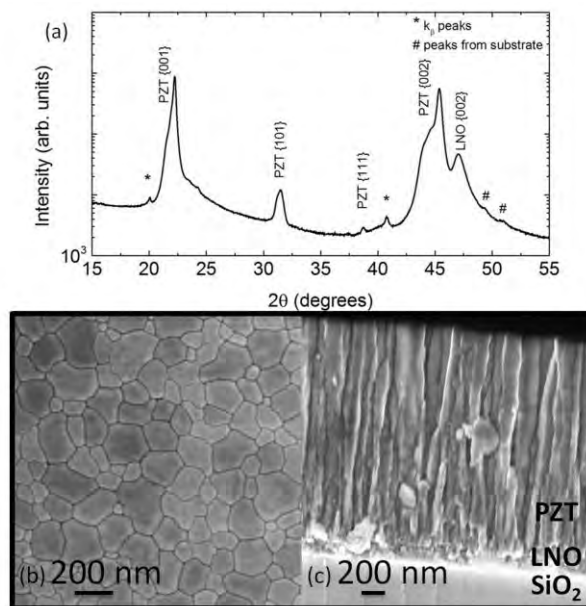


Figure 3.1. (a) Diffraction pattern of the film demonstrating strong $\{001\}$ preferred orientation (b) Top-down micrograph of the PZT film showing grains with no evidence of secondary phases or cracking. (c) Cross-sectional micrograph of the film indicating columnar growth of dense PZT on LNO.

Released Structure Processing

In order to release the films via undercutting the substrate, $10 \mu\text{m} \times 1.25 \text{ mm}$ trenches were etched through the Pt/PZT/LNO/SiO₂ stack to the underlying silicon. Etch pits were

necessary to expose the substrate so the Si could be removed via an isotropic XeF₂ etch, thereby declamping portions of the film. A schematic of the pattern is shown in Figure 3.2.

The etch pits were photolithographically defined using a multilayer deposition of SPR 955 described in Appendix 1. A total thickness of approximately 12 microns was routinely achieved and was a suitable etch mask for the materials and thicknesses in question. The etch pits were dry etched via reactive ion etching (RIE) in a Tegal 6572 RIE tool (Tegal Corporation, Petaluma, CA). The conditions for the etch recipes are given in Table 3.1. The CF₄ gas was used for the high reactivity of the fluorine with the Ti and Zr and the chlorine gas was used for its high reactivity with the Pb and Pt [33]. The Ar gas provides a physical etching component which was especially important for the Pt [33]. Additionally, it is known that LaNiO₃ etches well in a Cl₂/Ar based gas chemistry, so the same process was used for both perovskites [34]. The etch steps were limited to 30-45 seconds to allow the He backside cooling to efficiently reduce the temperature of the wafer. While the etch rate increased as temperature is increased, the selectivity between the photoresist and the etched film decreased. Furthermore, if temperatures are increased further, the resist may reticulate and reflow, ruining the resist as an etch mask.

Following RIE etching, the sample was annealed at 400 °C for one hour to reduce etch damage (such as hydrogen from the photoresist, which can diffuse into the PZT lattice and degrade the film properties). This step is critical as the hydrogen can form an [OH⁻] bond between the hydrogen ion and oxygen ions in the perovskite structure known to suppress the switchable polarization [35]. A recovery anneal at 400 °C for at least a half hour has been demonstrated to allow the hydrogen ions to diffuse out, enabling recovery of a substantial switchable polarization [36].

Table 3.1: Etch Conditions Utilized for Sample Processing

Material	Chamber Pressure	Gas Chemistry	Forward Power	Etch Time
Pt	5 mTorr	20 sccm Cl ₂ 40 sccm Ar	300 W at MHz 0 W at kHz	30 seconds (10 cycles total)
PZT/LNO	5 mTorr	7 sccm Cl ₂ 45 sccm Ar 28 sccm CF ₄	300 W at MHz 125 W at kHz	30 seconds (60 cycles total)
SiO ₂	5 mTorr	50 sccm CF ₄	300 W at MHz 25 W at kHz	45 seconds (20 cycles total)

XeF₂ release

To release regions of the ferroelectric film, the silicon was isotropically etched using a Xactix XeF₂ e1 vapor etch system (SPTS, Allentown, PA). XeF₂ was chosen as it readily etches silicon with good selectivity compared to the other materials in the stack. XeF₂ gas, sublimed from a solid XeF₂ crystal, reacts with the surface of the silicon, forming fluorosilyls (e.g. SiF₄). The fluorosilyls then desorb to form gaseous SiF₄ at room temperature [37]. The ability to perform the etch at room temperature is important as temperature-induced deflection of the released diaphragm will produce tears in diameters > 100 μm. While in most cases, any native SiO₂ formed post etch can be removed using XeF₂, this is not always the case [37]. Therefore, a short SiO₂ etch was performed just prior to the release step in order to remove any native oxide that may have formed in the etch pit during the post-etch anneal.

A witness wafer was used to gauge when the etch on the real sample would be close to the desired dimensions. However, the XeF₂ etch is very sensitive to the amount of silicon exposed and the geometry of the etch mask. For example, silicon exposed by etch pits of a smaller size or a deeper pit demonstrated reduced etch rates than silicon below larger, more shallow etch pits. Additionally places where more silicon is exposed will use the XeF₂ in the

chamber faster and lower etch rates will be seen in those regions. Therefore, a witness wafer will experience slightly different etch rates and can only be used as a guideline. The diaphragms on the real sample were broken post measurements to reveal an actual etch length of $99.7 \pm 3.3 \mu\text{m}$.

The goal of the study was to understand the role of declamping of the substrate by systematically releasing portions of the film. Control of percentage release was achieved by spacing the etched trenches in such a way that upon etching the underlying silicon, different amounts of release were achieved (fully clamped, $25\% \pm 0.8\%$, $50\% \pm 1.6\%$ and $75\% \pm 2.4\%$ of material is released from the substrate). A schematic the different etch pit spacings is shown in Figure 3.2. This technique enabled the same film to be used for all the measurements in this study, thus minimizing film to film variation, for example, due to other pinning sites such as grain boundaries and point defects.

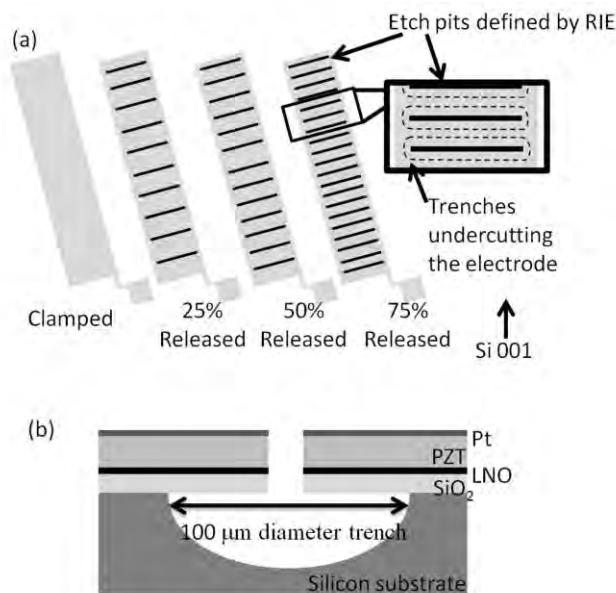


Figure 3.2. The electrode release schematic is shown. (a) Electrodes were deposited in groups of four with a small contact pad to the side for the electrical probes during the *in situ* X-ray measurements. Different degrees of release were achieved by changing the spacing between the etch pits on each electrode. (b) Approximately 100 μm width trenches were then undercut into the silicon using a XeF₂ etch.

The sample underwent 27 total cycles (etch time: 60 seconds, XeF₂ pressure: 2 Torr) in order to etch ~ 100 microns of silicon beneath the etch pits. This process is analogous to that used in previous reports [4] and a cross sectional schematic is illustrated in Figure 3.2.

3.1.3 Measurement Process at 11-ID-C

XRD measurements were performed at beamline 11-ID-C at the Advanced Photon Source at Argonne National Laboratory using an energy of 115 keV. The high brilliance of the X-rays significantly reduced collection times compared to a lab source diffractometer. Piece parts of the wafer were mounted on a custom built stage. Electrical probes were used to apply voltage to the electrodes via a Keithley 2410C 1100 V source meter. An HP 4194 LCR meter was used to check electrical contact. The leakage current density remained below ~ 10⁻⁶ A/cm² for all measurements. The sample was tilted 1° to the incident beam in order to increase the irradiated area of the sample. The X-ray beam was 500 μm in the horizontal direction and 100 μm in the vertical direction. As such, taking into account the tilt of the sample, the beam had a footprint on the sample surface of 500 μm x 5.6 mm. The electrode under measurement was aligned to the beam spot to ensure the resulting diffraction pattern was only from actuated PZT. The alignment was performed in x, y, z and theta.

The volume fraction of ferroelectric/ferroelastic domain switching in samples with different release states was then quantified via XRD. Diffraction patterns were measured from capacitors that were fully clamped to the substrate as well as ~25%, ~50%, and ~75% released from the substrate. In all cases, individual capacitors were poled using a sequence of electric fields, shown in Figure 3.3, where increasing voltage was applied in steps of 0.25 V_c up to 1.5 V_c at which point the voltage was decreased in steps of 0.5 V_c. Following this, the sample was measured while applying voltage up to 3 V_c in steps of 0.5 V_c and back to zero in steps of V_c. At

each step, the voltage was applied for 210 seconds, during which time the 2D diffraction patterns were recorded. The 2D diffraction patterns were calibrated using a powder CeO_2 standard to determine the position of the detector relative to the sample to extract d-spacing values.

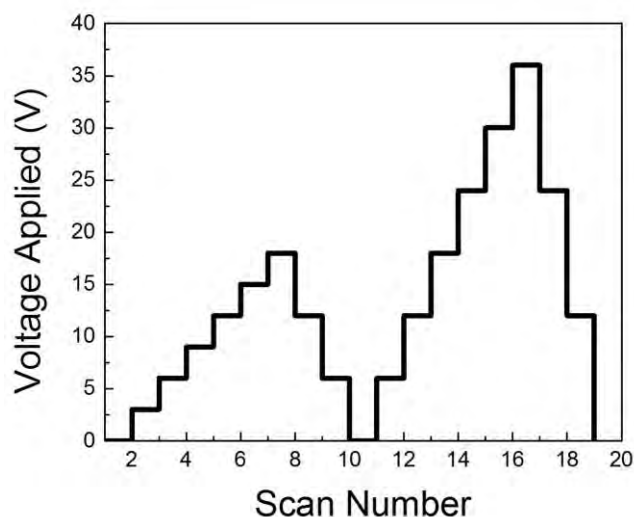


Figure 3.3. A schematic of the voltage applied to the sample during the *in situ* poling study. The voltage was first increased in steps of $0.25 V_c$ up to $1.5 V_c$. It was then decreased in steps of $0.5 V_c$ back to 0 V. The second voltage sweep took the sample up to $3 V_c$ in steps of $0.5 V_c$ and then back down to zero in steps of V_c .

3.1.4 Processing Raw Data

The calibration and processing (extracting line profiles from 2D diffraction patterns) was carried out using Fit2D software (European Radiation Synchrotron Facility, Grenoble, France) [38]. Prior to data analysis, Fit 2D was used to integrate the intensity of the Debye-Scherrer rings over a 20 degree sector and convert it into a 1D pattern. For data shown in the present work, the sector chosen was the vertical direction (close to parallel to the direction of applied field). The sector was integrated using Fit2D with an integration range of $\pm 10^\circ$ azimuthal angle to extract 2θ versus intensity data; these were later converted to d-spacing. Examples of the line profiles obtained from this procedure are seen in Figure 3.4.

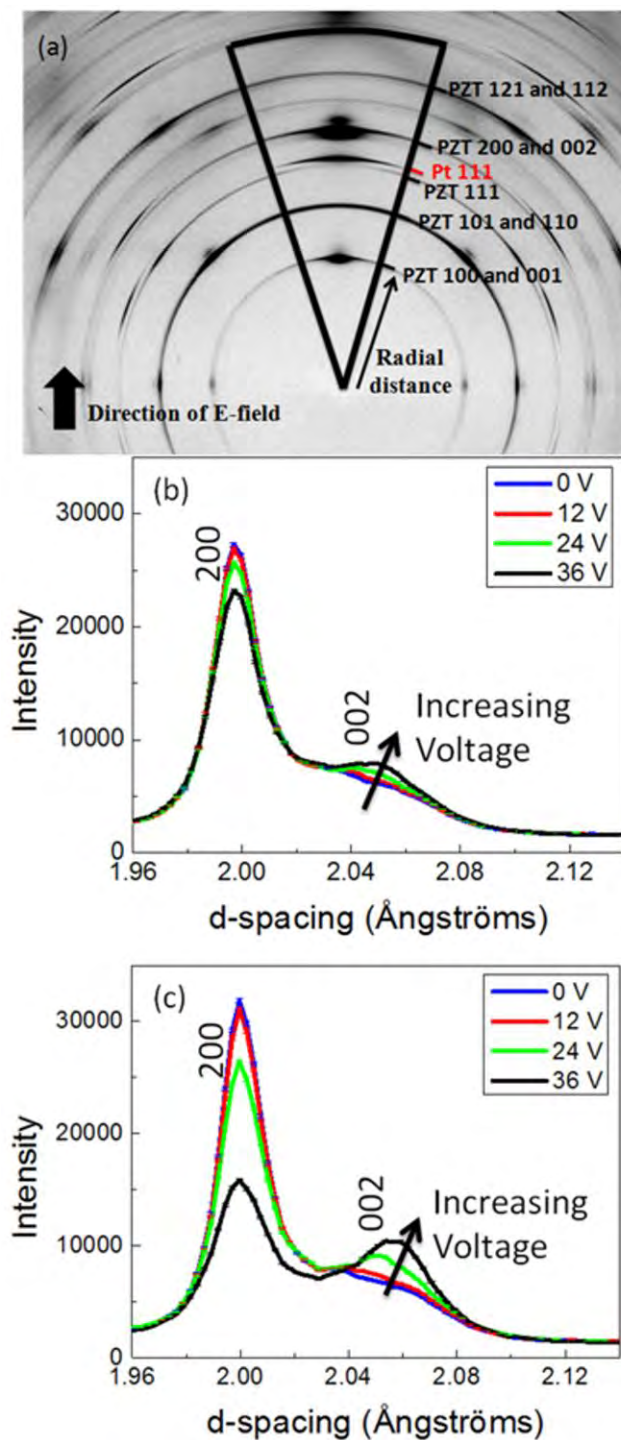


Figure 3.4. (a) An example of a 2D diffraction pattern with the integrated sector to create a 1D diffraction pattern outlined. Also shown in the schematic are the radial distances for the PZT and Pt peaks. (b) and (c) show the processed data of the peak intensity changes of the 200/002 peaks for the clamped (b) and 75% released (c) data. The error bars are well outside of the observed changes for both release states. The direction of increasing voltage is shown with an arrow; the lines correspond to 0 V, 12 V, 24 V and 36 V (0 kV/cm, 63 kV/cm, 126 kV/cm and 189 kV/cm, respectively).

Quantifying the changes in peak intensity and peak shape requires fitting the diffraction data to profile shape functions. Figure 3.4 shows an example 2D diffraction pattern obtained at 11 ID-C. As is seen in Figures 3.4, there is an obvious change in intensity of the 002 and 200 peaks as a function of electric field. Here, the domain reorientation is observable through the increase in the 002 intensity and decrease in 200 intensity as voltage is increased. Based on the data shown, it is clear that films that are partially de-clamped from the substrate (i.e. 75% released) show a much stronger change in intensity than in the clamped film, qualitatively demonstrating a higher degree of domain wall motion in response to electric field in the released films.

Following the data reduction procedure, the diffraction peaks in the line profiles were fit using asymmetric Pearson VII functions. The asymmetric Pearson VII provided the best fit for the {002} PZT peak profile. Symmetric Lorentzian or pseudo-Voigt profiles were not suitable due to the fact that diffuse scattering associated with the domain structure is observed [39]. Figure 3.5 shows an example of the {002} peak profile and the asymmetric Pearson VII fit. There can be several sources of diffuse scattering in ferroelectrics, for instance due to strain near domain walls [39] or spatial variations in the polarization [40], [41]. In this case, the dominant contribution to diffuse scattering between the 002 and 200 diffraction peaks has been attributed to strain near the domain walls. Tetragonal ferroelectric perovskites that have {110} ferroelectric/ferroelastic domain walls can have strain fields located around the domain wall due to the distortion of the structure that occurs during cooling through the Curie temperature. A perfect twin boundary would be strain free, but ferroelectric/ferroelastic domain boundaries have been shown to have lattice distortions in 5-10 unit cells near the domain boundary for compositions near the morphotropic phase boundary [42]. Strained domain boundaries have also

been observed in tetragonal compositions [39], [43] like the ones in the present study. Furthermore, PZT films processed in a similar manner do not show the asymmetry indicative of diffuse scattering when the films contain 3-4 vol% porosity, suggesting the dominant contribution to diffuse scattering is from local strains associated with the domain structure [25]. The resultant diffuse scattering is observable as an increase in intensity between twin-related reflections. A peak integration procedure was used to provide a reasonable estimate of the intensity under the peaks in cases in which long tails may contribute intensity to adjacent peaks [39]. A schematic of the method used to determine the integrated intensity is shown in Figure 3.5. In short, a window of integration is selected. The distance between the two center positions is defined as 2δ . An analytical integration of each profile is performed between the upper and lower bounds of $-\delta$ and $+\delta$ where δ is the distance away from the peak center position.

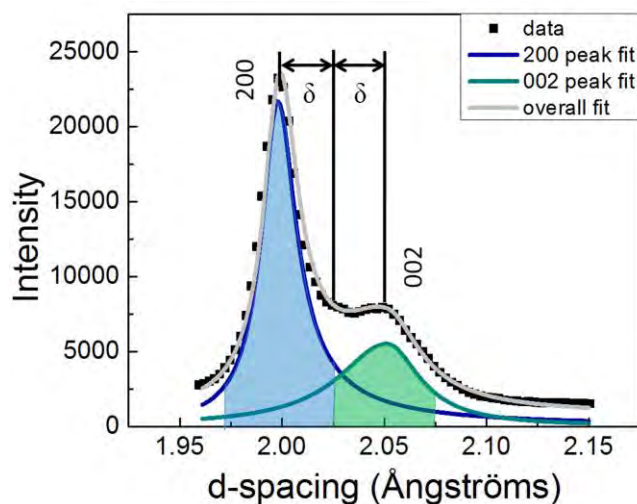


Figure 3.5. An example of a selection of a 1D pattern taken at the highest voltage (36 V, 189 kV/cm) on a clamped sample. The dotted black line represents the processed data from the 2D diffraction pattern while the grey line shows the fit with an asymmetric Pearson VII function. The grey line is the summation of the two individual peak fits which represent the PZT 200 and PZT 002 peaks. The center positions of each peak (indicated by a short line intersecting the middle of the peak) are used to determine how wide the window of integration should be. The width of the window is defined by assigning 2δ as the distance between the two peak centers. The integration is then performed with limits of $-\delta$ to $+\delta$ where δ is the distance away from the center of the peak. The background is not included in the integrated intensity.

3.1.5 Volume Fraction Calculations

The amount of domain reorientation as a function of applied field was quantified based on the intensity changes of related twin peaks [27], [44]. To calculate the volume fraction of 002 domains, v_{002} , in tetragonal PZT ceramics, Equation 3.1 is used. Here, the term I_{hkl} is the integrated intensity of the given hkl reflection and I'_{hkl} is the reference intensity from the powder diffraction file ($I'_{002} = 109$, $I'_{200} = 249$) [45]. By using the ratio of the integrated intensity over a reference intensity, the differences in the structure factors for 200 and 002 reflections were taken into account. Additionally, the {200} peak includes both 200/020 reflections. As a result, when calculating the volume fraction of 200 domains, a factor of two must be inserted into the numerator to account for this multiplicity (which is already factored into the powder diffraction file). Equation 3.2 shows the modified equation for the 200 domains.

Equation 3.1

$$v_{002} = \frac{\frac{I_{002}}{I'_{002}}}{\frac{I_{002}}{I'_{002}} + 2 \frac{I_{200}}{I'_{200}}}$$

Equation 3.2

$$v_{200} = \frac{2 \frac{I_{200}}{I'_{200}}}{\frac{I_{002}}{I'_{002}} + 2 \frac{I_{200}}{I'_{200}}}$$

The volume fraction of 002 domains for each state of release for the first cycle can be seen in Figure 3.6. This gives important information regarding the initial state of the domains. In PZT 30/70 thin films deposited on silicon substrates, the domain structure is not random. Instead, there is a preference for the polarization (along [001]) to lie in plane due to the tensile stress imposed by the substrate-film thermal expansion mismatch [23], [24], [46]. The volume fraction of reoriented domains, η , is relative to this initial domain state. In <100> perovskite single

crystals, the highest amount of domain reorientation from a sample with an originally random domain population is $\eta=0.67$; however in thin films, the initial v_{002} is smaller than in bulk ceramics. Thus, there is increased opportunity for domains to reorient that is coupled to the initial v_{002} .

While it is accepted that domain wall motion is clamped by the substrate [3], [4], [13], it is unclear whether or not domain wall motion increases in released films because the height of potential wells is decreased or because the domain wall density is reduced in released films [4]. In this data, the v_{002} is approximately the same ($24.4\% \pm 0.33\%$) in the unpoled material for all states of release. If the domain wall density were to decrease in released films, it is expected that the initial volume fraction of the 002 domains would change. As this doesn't happen, the data supports the claim that domain walls are more mobile in released films, as the clamping from the substrate which imposes large barriers to domain wall motion is removed.

3.1.6 Quantification of Domain Reorientation

For thin films, since the film starts with a preferred domain state, the volume fraction of reoriented domains, η , can be calculated using the initial zero field measurement as show in Equation 3.3.

$$\eta_{002} = \left(\frac{\frac{I_{002}}{I'_{002}}}{\frac{I_{002}}{I'_{002}} + 2 \frac{I_{200}}{I'_{200}}} \right) - \left(\frac{\frac{I_{002}}{I'_{002}}}{\frac{I_{002}}{I'_{002}} + 2 \frac{I_{200}}{I'_{200}}} \right)^{0 \text{ field}} \quad \text{Equation 3.3}$$

Here, the zero field measurement is the volume fraction of 002 domains in the unpoled state.

Since the experiment cycled through two voltage sweeps, the data for the second cycle shown in Figure 3.6 are offset from zero, accounting for the hysteresis from the initial cycle.

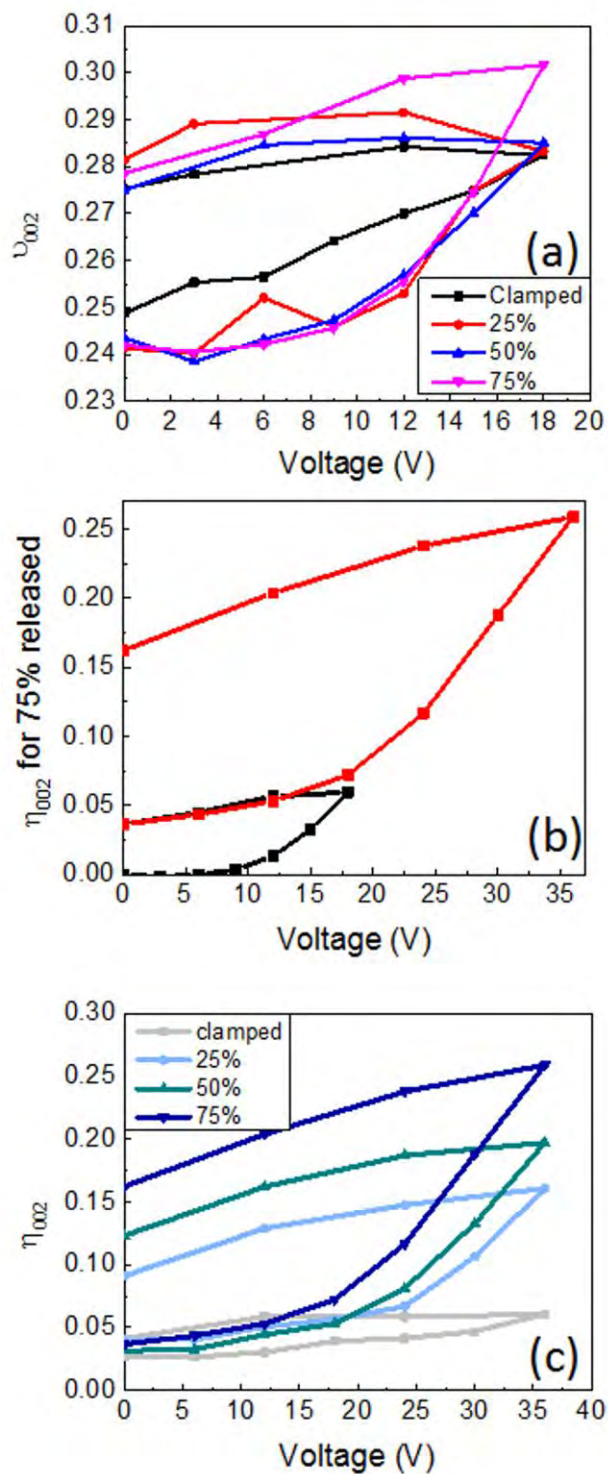


Figure 3.6. (a) The volume fraction of 002 domains for the first cycle for different release states. (b) The volume fraction of reoriented domains for the first cycle up to 1.5 V_c (black) with the second cycle up to 3 V_c (red) in the 75% release sample. (c) The volume fraction changed (η_{002}) of the 002 peak as a function of voltage for the 4 films under different release states. Voltages as high as 3 V_c were applied to the films.

The volume fraction of domains that were reoriented in response to applied voltage is shown in Figure 3.6. In Figure 3.6b, both cycles of voltage are shown for the 75% released sample while Figure 3.6c shows the volume fraction of domains changed in the second voltage cycle for each state of release. Because the intensity of the symmetry-related reflections is approximately conserved and the fact that η_{002} and η_{200} are not independent, either η value is valid. Here, the intensity change in the 002 peak was inspected. The η increases with the amount of release for a given applied voltage; this is direct evidence that there is more 90° domain reorientation in released films (presumably due to higher mobility of the 90° domain walls). Due to the low intensity of the 002 reflections at low applied field, which can be seen by the 0 V scan in Figures 3.4 b and c, the uncertainty associated with the integrated intensity (calculated using error propagation) was high. Here, the confidence in the observed trends is based on the changes in the intensity observed in the data and the fact that those changes are outside the error bars, as is seen in Figure 3.4.

The amount of 90° domain reorientation as a function of applied electric field shows an increase with release state for a particular voltage. When the voltage was increased beyond a critical value, the elongated diaphragms cracked [4]. This was observed with an optical microscope during the *in situ* XRD measurements. In this work, the elongated diaphragms were monitored during the measurements and the voltage at which they started to crack was noted. Since the elongated diaphragms have a long beam-shaped etch pit, they tended to crack at the ends of the trench. Though the cracks are outside of the irradiated portion of the electrode, the change in the sample's strain state is reflected in the amount of domain wall motion. When the elongated diaphragms cracked, typically at voltages >18 V (94.7 kV/cm), the field dependence of η increased for the released electrodes; this slope change was not observed in the clamped

electrode, consistent with the absence of cracking. As the film is released from additional mechanical boundary constraints from the substrate, the amount of 90° domain reorientation is increased further. This is consistent with work by Griggio *et al.* where upon breaking the released diaphragms, a larger irreversible Rayleigh component was observed [4].

It was determined that the highest amount of domain reorientation was in the 75% released film with $\eta_{002} \sim 0.26$. This value for η is on the order of domain volume fraction changes in bulk PZT ceramics of similar composition [27], [28]. An as-deposited film on silicon has tensile in-plane stress, which results in a greater number of *a*-domains than bulk PZT ceramics. Because of this, there are more *a*-domains that can be switched with applied field. Thus, it is not surprising that even for de-clamped films that are <100% released, the film ferroelectric/ferroelastic switching is comparable to that for a bulk ceramic.

An extrapolated η for a fully released film was calculated and is shown in Figure 3.7. It is found that the data demonstrates an approximately linear relationship between the degree of release and η_{002} at the highest applied field. Assuming linearity, an extrapolation to a fully released film is possible. Using this model with the maximum values (which represent cracked released structures), it is predicted that a fully released film would reorient approximately 32% of the 90° domains.

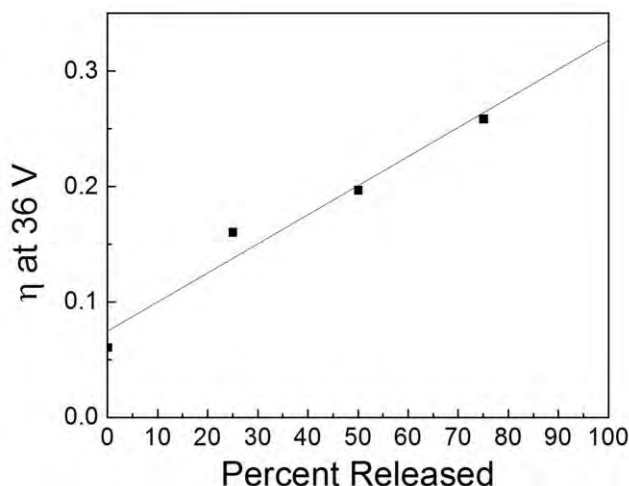


Figure 3.7. Volume fraction of domain reorientation at the maximum voltage ($3V_c$) applied for clamped, 25%, 50% and 75% released samples. A best fit line (R^2 value > 0.96) was used to extrapolate the volume fraction changed in a fully released sample; this corresponds to approximately 32% volume fraction reorientation.

The percent of domains that revert back to the original domain state (i.e. which will govern the remanence in η) when the field is removed was also found to decrease with degree of release. As the field is removed from the capacitor, some domains that reoriented to align with the electric field revert, or backswitch, to an a -domain state. It is thought that the mechanical boundary constraints which initially determine the domain configurations would increase the driving force for domains to relax back into those positions. Therefore, it is expected that as the mechanical boundary constraint is removed, there would be less driving force for the domains to reorient back to the original configuration. As the material reaches 50% release, there is a marked decrease in the amount of backswitching. For clamped and 25% released electrodes, about 56% of the domains oriented by applied fields relax back into the a -domain state, and for the 50% and 75% released films, only approximately 44% of the reoriented domains relax back.

3.1.7 Summary of Effect of the Substrate on Clamping Domain Wall Motion

Synchrotron X-ray diffraction was used to monitor 002-200 type reflections as a function of both applied voltage and the degree of release in tetragonal PZT thin films. It was found that

as the mechanical boundary imposed on the film is removed, domain reorientation increases. This suggests that enhanced piezoelectric coefficients should be observed upon declamping due to increased probability of ferroelectric/ferroelastic domain wall motion. As the amount of release increased from fully clamped to 75%, η for the film approached η values observed in bulk ceramics. These results provide direct evidence that substrate clamping plays a substantial role on the amount of domain reorientation observed in tetragonal PZT thin films.

3.2 Investigating the Role of Geometry of Release

3.2.1 Motivation

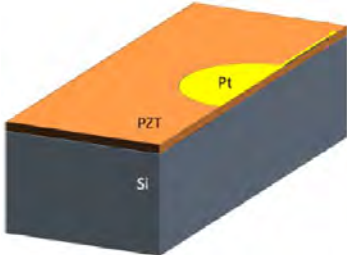
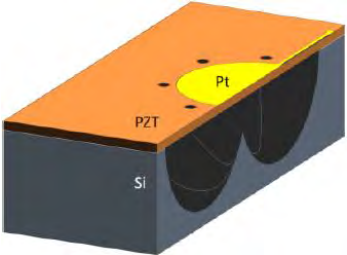
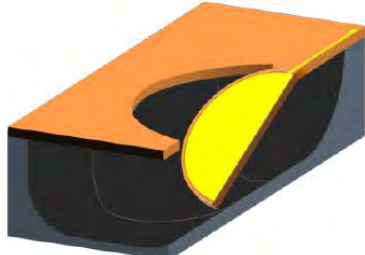
While many groups have studied the effect of substrate release on the ferroelectric response of PZT thin films, different methods are utilized for the release, which creates another variable (device geometry) which may affect the results. In order to better understand the role of the substrate in both restricting domain reorientation and controlling the strain state of the film, different device geometries and release methodologies were studied.

Release via a XeF_2 etch is a common method for undercutting silicon substrates [4], [47]–[49] and was used in the work reported in section 3.1. However, reports on the ferroelectric behavior of released films differ depending, on part, on the geometry of the released region. In a virtually identical experiment to the one described previously in this chapter, Esteves *et al.* showed that $\{111\}$ oriented PZT30/70 films exhibited no increase in domain reorientation when the film was 75% released from the substrate compared to a clamped case [49]. While this is likely primarily due to the $\{111\}$ orientation of the PZT, which has a domain-engineered domain configuration that reduces the propensity for domain switching (and thus domain reorientation should change less based on clamping to the substrate [50]), it cannot be ruled out that the geometry of release also played a role.

Yeager *et al.* showed only modest increases in the irreversible Rayleigh coefficient, α , when a circular shaped diaphragms were released [48]. The films in that study were 1.17 μm and 1.64 μm thick, undoped, {001} oriented PZT 52/48 with an average grain size of approximately 200 nm. The Lotgering factors for these films ranged from 80-90%. Upon the local release of the PZT thin film, almost no change in α was seen. Furthermore, upon breaking of the diaphragms and achieving a globally released device, the α coefficient increased only by a factor of two [48]. This is in contrast to the work shown in section 3.1, as well as reports of declamping via patterning an epitaxial {001} film into island structures [51] and the work by Griggio *et al.* [4]. As the work by Griggio *et al.* also had high {001} texture (Lotgering factor $\sim 98\%$), it is not expected that these differences are a result of orientation. While some of these differences are likely due to the differences in the film itself, some discrepancy could be a result of different release geometries.

Additionally, there is work indicating that the overall strain state of the released region, determined via the geometry, is a critical component influencing the ferroelectric response. Yeager *et al.* showed finite element analysis for a fully released cantilever tab and island structures which indicated that restoring stresses associated with residual stresses will depend strongly on the specific geometries of the device [48]. This was further supported by his Rayleigh analysis, the results of which for a 1.17 μm , predominately {001} oriented, film, is presented in Table 3.2. Here, the increased restoring forces in the diaphragm structure cause the dielectric response to have no increased domain reorientation, which would result in a higher value of α . However, in the tab structure, depicted in Table 3.2, there is a 28% increase in the α coefficient when compared to the clamped α . This indicates that there is substantially more irreversible domain contribution to the properties of the tab structures.

Table 3.2. Effect of Geometry on Rayleigh Coefficients in Previous Work [46]

	Clamped	Diaphragm (Undercut)	Tab (Released)
Geometry			
Release State	Clamped	Local Release	Global Release
Description	Area under the electrode is completely attached to the substrate	Substrate is removed beneath the electrode but the film is not free to deform upon actuation due to the diaphragm stresses	Substrate beneath the electrode is completely removed and the actuated film is able to deform
ϵ_{init} (@ 1 kHz)	1082	1051	988
α (cm/kV) (@ 1 kHz)	26.06	24.09	33.4

In order to better understand the previous data in the context of the literature, it would be useful to have a measure of domain reorientation for release using different geometries. Domain reorientation is explored in samples with an elongated beam geometry (described in section 3.1) and also a circular geometry, where the substrate is etched from underneath the film using circular etch pits. This circular geometry is closer to what was used by Esteves *et al.*, Griggio *et al.*, and Yeager *et al.* and will provide a better understanding of the causes of discrepancies between previous reports.

3.2.2 Processing of Thin Films with Hole and Beam Geometries

A 1.77 μm thick film of chemical solution deposited (CSD) $\text{PbZr}_{0.30}\text{Ti}_{0.70}\text{O}_3$ (PZT 30/70) doped with 1% Mn was used for this study. The film was deposited on a thermally oxidized silicon wafer (NOVA Corporation) where 130 nm of Ti had been sputter deposited as the adhesion layer and the bottom electrode Pt was sputtered, at room temperature, on top of that.

Previous work by Fox *et al.* demonstrated that as the thickness of the titanium adhesion layer underneath the Pt electrode is increased, the Pt {111} texture is decreased [52]. As PZT texture can be templated from the underlying Pt, this leads to incompletely oriented films where different PZT reflections have similar intensities. This film was selected for the geometry of release experiments because both the processing and the subsequent synchrotron measurements were performed at the same time with the same tools for both geometries. An example diffraction pattern taken at the synchrotron showing the film orientation is shown in Figure 3.8.

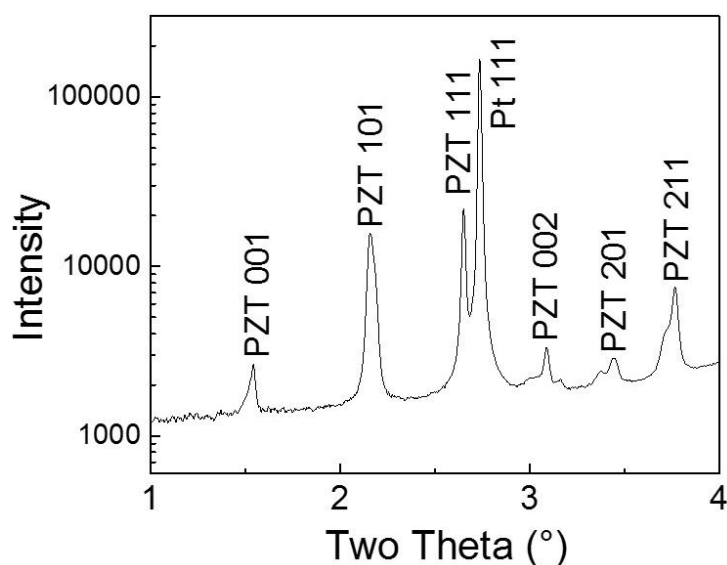


Figure 3.8. X-ray diffraction pattern taken from the incompletely oriented film at the synchrotron ($\lambda=0.10801 \text{ \AA}$)

The as-deposited films were dense and while the top down FESEM micrograph shows small amounts of surface pyrochlore, the overall volume of the second phase is small compared to the perovskite phase and is evenly distributed across the wafer. As such, comparisons between different electrodes on the same wafer are possible. The top down and cross-sectional FESEM micrographs are shown in Figure 3.9. Additionally, the electrical properties of the as-deposited films show good characteristics, indicating they are not significantly influenced by any surface pyrochlore. The remanent polarizations are $> 30 \mu\text{C}/\text{cm}^2$ and the dielectric constant is 510 with a loss of 2.1% measured at 1 kHz and an ac signal of 30 mV. The leakage current density,

measured at three times the coercive voltage for 20 minutes, was below 1×10^{-7} A/cm² with no degradation of the material ($V_c = 12$ V, $E_c = 68$ kV/cm). Examples of the electrical data can be found in Figure 3.9.

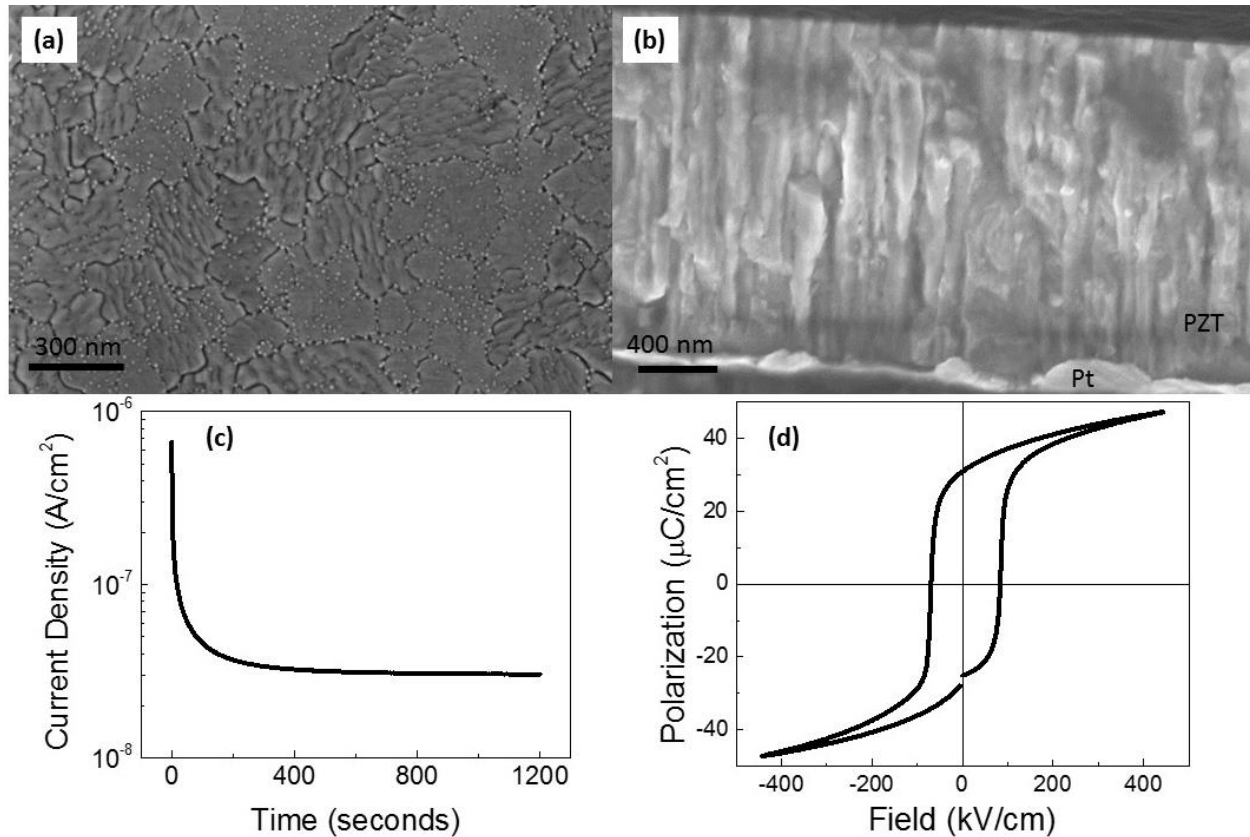


Figure 3.9. (a) top down and (b) cross-sectional FESEM micrographs. A small amount of pyrochlore exist on the surface but it is evenly distributed. The cross section shows good density. (c) leakage current density and (d) polarization versus field (P–E) loops. The P–E loop was taken at 10 Hz.

Two geometries of release were investigated, one geometry, as described in the above sections, where the etch pits are shaped into $10 \mu\text{m} \times 1.25 \text{ mm}$ beams, and one where the etch pits were $10 \mu\text{m}$ diameter circular holes. The RIE etch recipes are identical to the ones described previously. In both cases, $100 \mu\text{m}$ of underlying silicon was etched away beneath the bottom electrode to form elongated diaphragms and circular diaphragms. Schematics of the different geometries are shown in Figure 3.10.

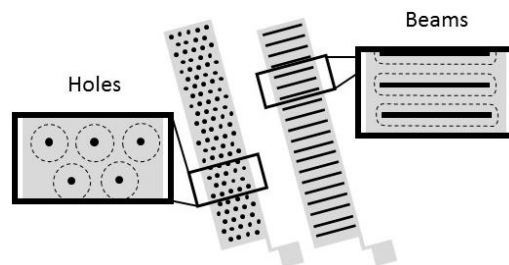


Figure 3.10. Schematic showing the two different geometries of release investigated in this study. Circular shaped etch pits (holes) with resulting circular diaphragms (the diameter is indicated with the dashed line) and beam shaped etch pits (beams) with elongated diaphragms.

The measurement methodology utilized was identical to the process outlined previously, including the voltage application sequence. The leakage current density was monitored during irradiation and remained below $\sim 10^{-6}$ A/cm² for all measurements. In this case, electrodes 75% released from the substrate with either the hole or beam geometry were measured in addition to a clamped electrode.

3.2.3 Investigation of 112/211 Reflections

An example 2D diffraction pattern measured at 11-ID C is shown in Figure 3.11. To obtain 1D diffraction patterns, the raw data were integrated over a sector of interest. Using Fit 2D, a 20° sector parallel to the electric field was investigated.

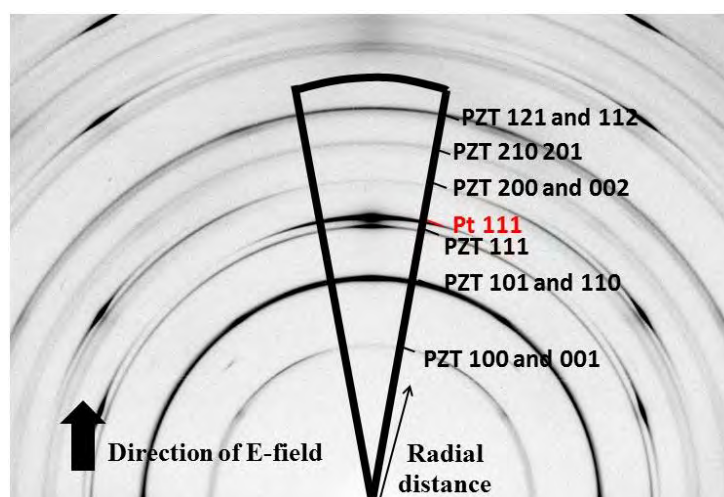


Figure 3.11. An example of a 2D diffraction pattern for the incompletely oriented sample with 130 nm of TiO₂ beneath the bottom electrode. The integrated sector to create a 1D diffraction pattern is outlined and PZT/Pt peaks are labeled.

Example line profiles from clamped, 75% released films using a hole geometry, and 75% released films using a beam geometry, are shown in Figure 3.12. Because of the texture of this film, the 112/211 peaks were considered. The intensity of these peaks was large and the peaks were further apart than PZT reflections at lower 2θ values. By inspection, it is not clear if there is an appreciable increase in domain reorientation in the electrodes released via the hole geometry when compared to the domain reorientation seen in the clamped sample. On the other hand, there is substantially more domain reorientation in the sample released via the beam geometry.

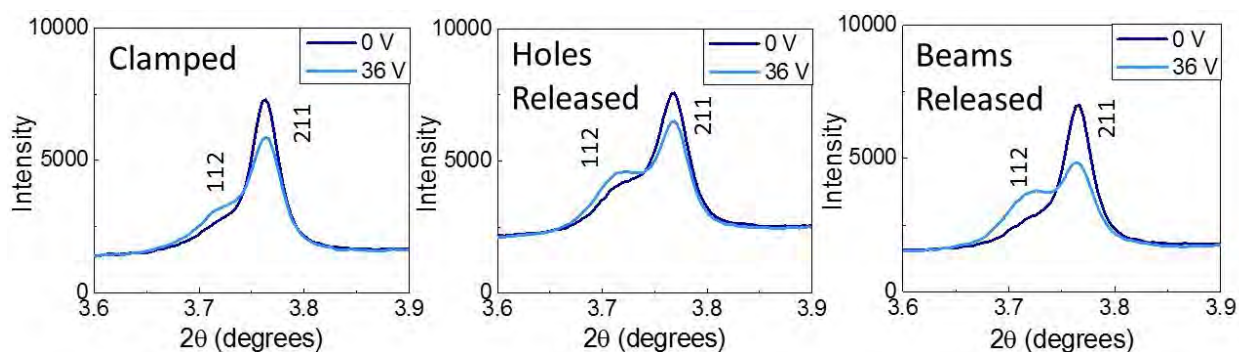


Figure 3.12. Line profiles extracted from the 2D diffraction patterns for clamped, hole released, and beam released PZT films. While clamped and hole released electrodes show similar amounts of domain reorientation between 0 V and 36 V, there is a noticeable increase in domain reorientation in the beam release geometry.

For a quantitative analysis of the intensity exchanges, diffraction profiles were fit using Mathematica. Several different fitting functions were investigated but it was found that two Lorentzian functions fit the 112/211 peaks well for all geometries of release and voltages. An example of one such peak fit is shown in Figure 3.13.

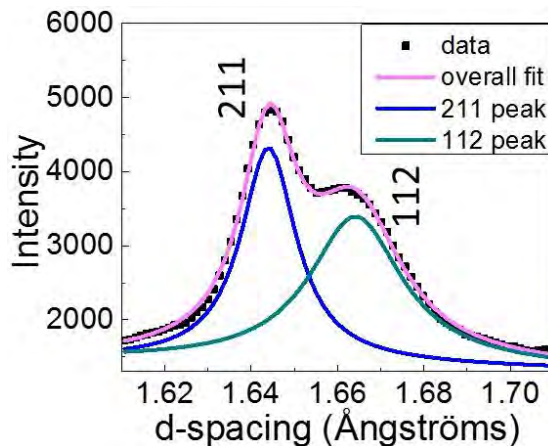


Figure 3.13. An example of the data fitted with two Lorentzian functions for the sample released via beam geometry at $3 V_c$

The use of symmetric functions simplifies the calculation of the integrated intensity and is usable for this case due to the lack of diffuse scattering between these peaks. In this case, the integrated intensity was calculated using an analytical integration of the fitting function from $-\infty$ to $+\infty$. The integral for the integrated intensity for the Lorentzian functions is shown in equation 3.4.

Equation 3.4

$$\int_{-\infty}^{+\infty} Amp \left(\frac{2}{\pi} \frac{FWHM}{4(x - x_0)^2 + FWHM^2} \right) dx$$

<i>Amp</i>	Amplitude of the fitting peak
<i>FWHM</i>	Full width half max of fitting peak
x_0	d-spacing of center of fitting peak
x	d-spacing

3.2.4 Volume Fraction Calculations for 112/211 Peaks

The volume fractions of 211/112 domains were calculated using the integrated intensities and the same methodology described previously. The equation for the volume fraction of 112 domains is shown in Equation 3.5.

Equation 3.5

$$v_{112} = \frac{\frac{I_{112}}{I'_{112}}}{\frac{I_{112}}{I'_{112}} + 2\frac{I_{211}}{I'_{211}}}$$

I_{hkl} is the integrated intensity while I'_{hkl} is the reference intensity from the powder diffraction file ($I'_{112} = 138, I'_{211} = 332$) [45]. Due to the difference in thermal expansion coefficient, the tensile stress imposed on the film increases the volume fraction of {211} domains with respect to 112. The volume fractions of the 211/112 domains for the first voltage cycle of the three electrodes probed is shown in Figure 3.14.

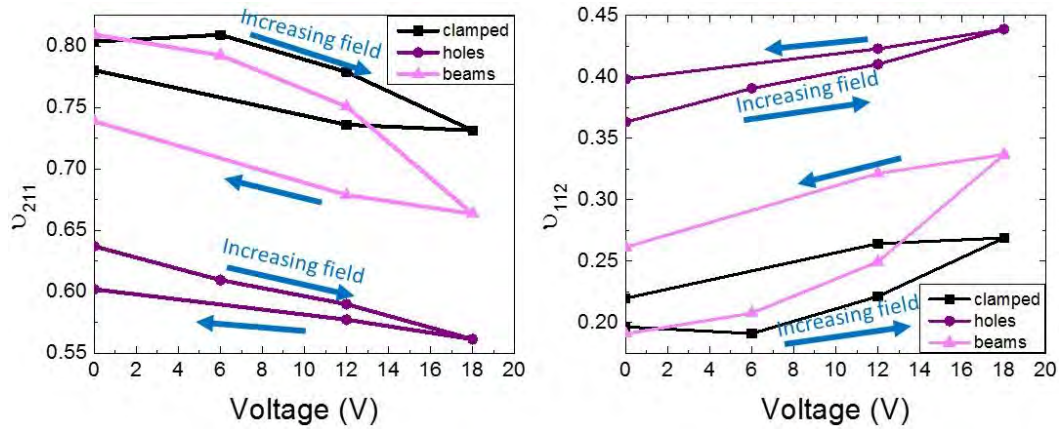


Figure 3.14. The volume fraction of 211/112 domains as a function of voltage. The clamped electrode and the electrode released via the beam geometry (beams) show similar initial domains volume fraction, while the electrode released via the hole geometry show a different volume fraction.

While the clamped electrode and the electrode released with a beam geometry show similar initial volume fractions, the electrode released with the hole geometry shows an increased volume of 112 domains. The reason for this is unknown though it was not expected as it was seen previously that releasing the film did not change the initial volume fraction. The difference in initial volume fraction is not expected to have influenced the domain reorientation discussed below. Separate data corroborating this is presented at the end of this section.

3.2.5 Quantification of Domain Reorientation for Different Geometries

The volume fraction of reoriented domains at a specific voltage, η , was calculated using the initial zero field measurement as shown in Equation 3.6. As mentioned previously, this accounts for the initial domain state imposed by the substrate.

Equation 3.6

$$\eta_{112} = \left(\frac{\frac{I_{112}}{I'_{112}}}{\frac{I_{112}}{I'_{112}} + 2 \frac{I_{211}}{I'_{211}}} \right) - \left(\frac{\frac{I_{112}}{I'_{112}}}{\frac{I_{112}}{I'_{112}} + 2 \frac{I_{211}}{I'_{211}}} \right)^{0 \text{ field}}$$

As the overall population of 211/112 domains is conserved, the percentage of domains reoriented is the same for both reflections. Here, the 112 domain reorientation will be discussed. Each electrode was electrically excited in two voltage sweeps. The first sweep increased the voltage to $1.5 V_c$, where the diaphragms remain intact, and the second sweep increased the voltage to $3 V_c$, where diaphragms broke. The domains reoriented, η_{112} , for the first voltage cycle for the three states of release is shown in Figure 3.15.

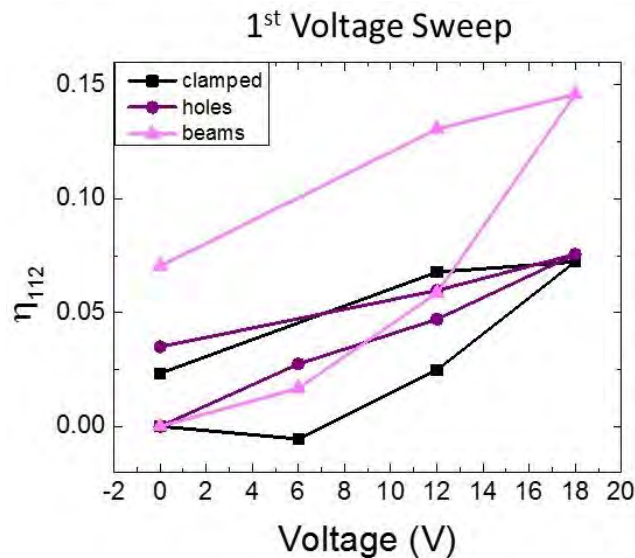


Figure 3.15. The volume fraction of 112 domains reoriented with applied field for the first voltage cycle where the structures are locally released.

The amount of domain reorientation seen in the clamped electrode compared with the electrode released via the hole geometry is very similar at 1.5 V_c. The two electrodes show about 7 vol% domain reorientation at high voltage. In contrast, the percentage of domain reorientation experienced by the film released by the beam geometry is increased by approximately a factor of two to 14 vol%. Additionally, in the film released by beams, ~ 7 vol% of the switched domains retained their switched state when the field was removed, compared to ~2-3 vol% in the clamped film and the film released by holes.

To better understand the difference in stress state between the two release geometries, models estimating the strain relaxation were generated in COMSOL. For the circular and elongated beam diaphragms, the released region (100 μm in diameter) was modeled using material data found in Table 3.3.

Table 3.3 Materials Properties Used for COMSOL Models

Material	Thickness	Young's Modulus	Poisson Ratio	Initial Stress: $\sigma_{11} = \sigma_{22}$
PZT-5H	1.77 μm	85 GPa	0.26	150 MPa [53]
Pt	100 nm	168 GPa	0.38	1200 MPa [53]
TiO ₂	300 nm	230 GPa	0.27	500 MPa [54]
SiO ₂	1 μm	70 GPa	0.17	-150 MPa [55]

The model was made using a 2D mesh of tetrahedral elements that was propagated from the base to the surface of the membrane with four partitions for the different layers. The outer perimeter, where the film is connected to the silicon substrate, was set as a fixed boundary condition. The etch pit perimeter, where the material is free to deform, was set as a free boundary condition. As previously discussed, the higher thermal expansion coefficient of the PZT places the film in tensile stress when fabricated on silicon. As a result, when the residual tensile stress in the film is removed, the release sections curls. Thus, the z-displacement shown from the strain

relaxation plots is an indication of how much in-plane stress still exists in the structures post release. The resultant z-displacements from the strain relaxation for the two geometries investigated are shown in Figure 3.16. The maximum z-displacement due to the strain relaxation seen in the beam diaphragm is an order of magnitude larger than the displacement in the circular diaphragms. At the free boundary perimeter, the maximum displacement seen in the elongated beam structures is approximately $0.78 \mu\text{m}$ while it is only $0.05 \mu\text{m}$ at the edge of the etch pit for the circular structure.

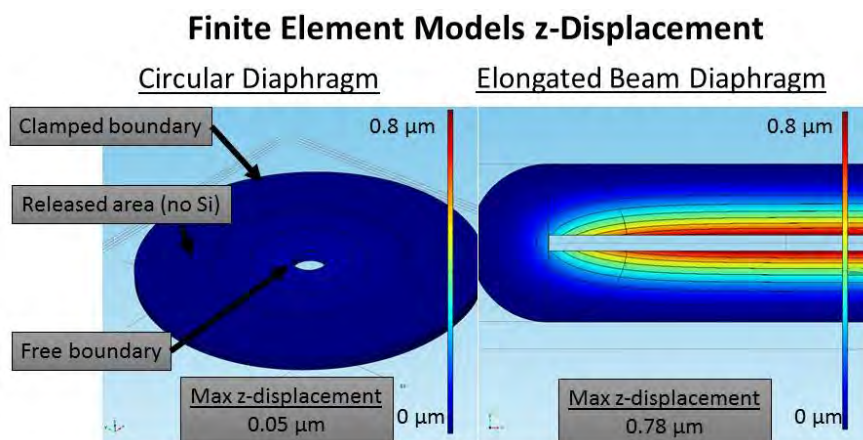


Figure 3.16. Finite element models of the z-displacement of the released areas of the circular and elongated beam diaphragms. The maximum displacement seen in the beam diaphragm is an order of magnitude larger than the displacement due to strain relaxation seen in the circular diaphragm.

The elongated beam geometry has a much higher degree of strain relaxation because of the larger amount of material next to the free boundary condition, where the structure is free to deform. Because of this, though the overall area of released region is the same for the two geometries, the beam geometry has a higher released perimeter where pinning of domains due to film stress is reduced.

The circular diaphragms are comparatively flat, even at the released boundary. Thus, it is clear that the in-plane stresses from fabrication are not well relieved in this geometry. In contrast, the larger deflection in the beam diaphragms with elongated etch trenches reduces the in-plane stresses. This information, coupled with the X-ray diffraction data, suggest that the in-plane

stresses from the fabrication plays a large role in the magnitude of domain reorientation, even upon release.

It should be noted that the zero field COMSOL models are no longer descriptive when the films are taken to high enough voltages to break the diaphragms ($> 1.5 V_c$ for these $1.77 \mu\text{m}$ thick films with $100 \mu\text{m}$ wide cavities). Once the diaphragms break, the released segments act more similarly to cantilevers and the in-plane stresses should be partially relieved. However, as is shown in Figure 3.17, the films released via the hole geometry do not show an increase in domain reorientation compared to the clamped electrodes even beyond the voltage where some breakage occurs. At $3 V_c$ the clamped electrode and the electrode released by holes show similar amounts of domain reorientation. The beam electrode shows about 20 vol % more domain reorientation at high field than the clamped electrode. Additionally, upon release of field about half the reoriented domains in both the clamped electrode and the electrode released via holes relax back. In contrast, the beam geometry shows only a modest relaxation of domains, with only about one quarter of the reoriented domains back switching.

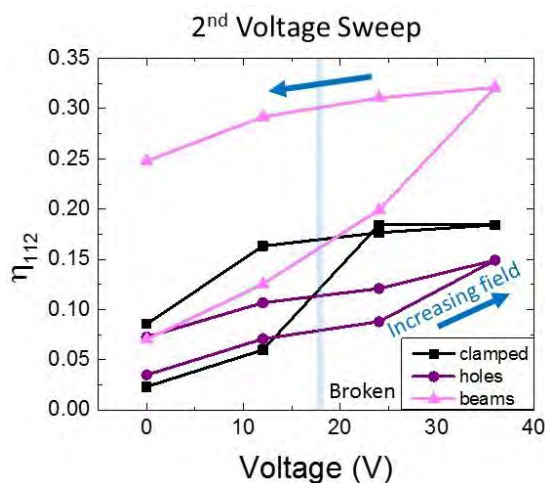


Figure 3.17. Reorientation of the 112 domains for three different geometry release states upon the second voltage sweep up to $3 V_c$.

This was unexpected based on the strain relaxation observed in the COMSOL models. Once the diaphragm breaks, increased strain relaxation should occur. However, the circular diaphragms have some variability in the way they break, as demonstrated in Figure 3.18. This will have an effect on the membrane tension and the overall strain state of the diaphragm. Yeager *et al.* showed that the irreversible Rayleigh coefficient, α , varied substantially depending on how the circular diaphragms broke - as the number of tears increased, so did alpha. It was found that upon sectioning the diaphragm into four sections, almost a two times increase in alpha was observed, compared to an unbroken one. However, only about a 1.5 times increase in alpha was seen for a diaphragm with two splits [48]. Similarly, not every diaphragm breaks at $V > 1.5 V_c$, and, after a voltage excursion up to $3 V_c$, there is some distribution of unbroken/broken diaphragms.

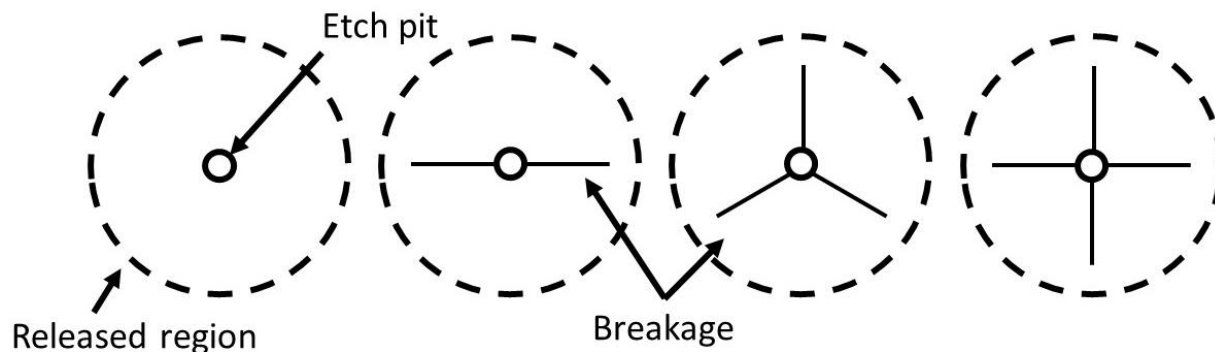


Figure 3.18. A schematic showing possible symmetrical breakage patterns of the circular diaphragms. The schematic shows (from left to right) a fully intact membrane and then ones with two, three and four splits.

The diaphragms were observed through an optical camera during actuation and displayed visual characteristics consistent with breakage at high voltage. However, given the low resolution of the camera, it could not be determined during the experiment how the diaphragms sectioned during the breakage. As such, it is difficult to speculate on the overall release state of the electrode and this may be at least part of the reason why these data differ from the reports of Griggio *et al.* and Yeager *et al.* However, after the *in situ* experiments, it was found that a

majority of the diaphragms sectioned into two parts. Few diaphragms were sectioned into three regions and no diaphragms were found to be sectioned into four.

Additionally, the material stacks in these three studies are not the same. Both Yeager *et al.* and Griggio *et al.* used substrates with thinner layers of SiO₂ under the film (100-200 nm) whereas in this study, 1 μm of SiO₂ was used [4], [48]. The thicker SiO₂ may also retain some of the stress and increase the pinning of domains.

Another possible explanation for the difference in data is the difference in composition. The experiments by Griggio *et al.* and Yeager *et al.* were performed on compositions at the morphotropic phase boundary (MPB), PZT52/48, while these data are from tetragonal PZT30/70 films. PZT films at the MPB have a higher density of domain walls than tetragonal PZT films, and as a result, can release residual stresses more easily due to increasing domain complexity [56]. Additionally, the PZT 30/70 films used here were doped with 1% Mn, which has been shown in bulk PZT to harden the material and make domain wall motion more difficult [29]. These differences may also contribute to the reduced 90° domain reorientation seen in this study.

While the electrode released via the hole geometry showed a different initial volume fraction of domains, it is not expected that this is responsible for the reduced domain reorientation seen in the circularly released electrodes. In similar measurements performed on {001} textured gradient free PZT30/70 films with electrodes released via a hole geometry, no significant difference in the initial volume fraction was detected. The integrated data for this is shown in Figure 3.19. These films started out with approximately the same initial volume fraction of 002 domains (~15-17%). During voltage cycling, both clamped and released films show comparable amounts of domain reorientation. Therefore, the difference in initial volume fraction in the previously discussed randomly oriented film is not expected to have skewed the

data. It is clear from these corroborated results that films released via a circular geometry do not show increased domain reorientation compared to clamped films.

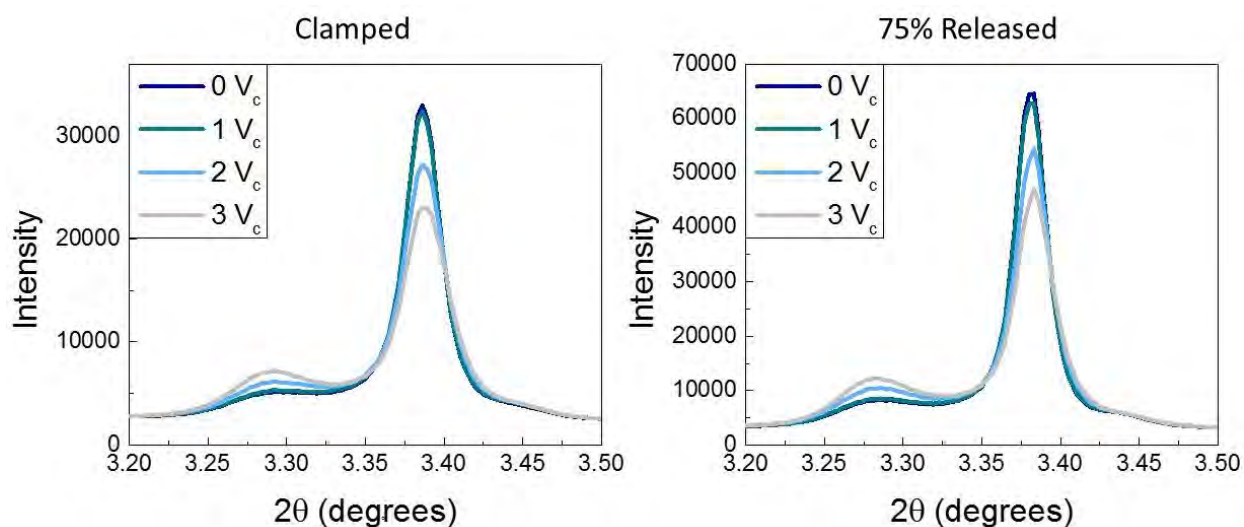


Figure 3.19. Integrated data from clamped and 75% released, 640 nm thick {001} oriented gradient free PZT 30/70 films. The 75% released electrode was released using a circular geometry. Both clamped and released films show comparable amounts of domain reorientation.

3.2.6 Summary of Effect of the Geometry on Clamping

Synchrotron X-ray diffraction was used to monitor the 112/211 reflections as a function of applied field to investigate the dependence of domain reorientation on the geometry of a released region. It was found that the geometry of the released region plays a significant role in the ability of ferroelastic domain reorientation. This helps to shed light on some of the differences in domain mobility reported in the literature. In electrodes where the substrate was removed in a circular diaphragm geometry, the amount of domain reorientation with applied field was nearly the same (only differing by 3 vol%) as the amount of domain reorientation expressed by the clamped electrode. This is in contrast to domain reorientation measured on samples in which the same percentage of the substrate was removed but in the geometry of elongated beams where approximately 20 vol% more domains were reoriented with applied field

than in the clamped electrode. Here, the domain reorientation up to $1.5 V_c$ was measured to be twice that of the clamped/hole released electrodes. This was shown to be due to the presence of in-plane stress which was not fully relieved upon the removal of the Si substrate. In release geometries where the perimeter of the free boundary is small, such as the case with the hole geometry, this stress dominates and suppresses domain reorientation.

3.3 Effect of the Elastic Properties of the Substrate on Domain Reorientation

3.3.1 Motivation to Investigate Domain Reorientation on Alternate Substrates

The previous results in this chapter focused on domain reorientation in tetragonal PZT films deposited on silicon substrates. However, for some applications, such as a next generation X-ray telescope, alternative substrates are of interest [57]. Thus, it is useful to understand how the domain response changes for different substrates.

As seen in section 3.2, the in-plane stress in the film is a major contribution to clamping domain wall motion. When the substrate was removed but the in-plane stress was still present, the film was not free to relax or deform and, as a result, less domain reorientation was observed. Tuttle *et al.* showed that the initial volume fraction of domains is determined by the difference in thermal expansion coefficients between the film and the substrate as well as the temperature range between the crystallization temperature and the Curie temperature [24]. In order to change the volume fraction of domains, the film must bow to accommodate the strain at field. The amount of static wafer bow at zero field is represented by the radius of curvature, the equation for which is given below [58]

Equation 3.7

$$\frac{1}{r_i} = \frac{6E_i t_i (\alpha_i - \alpha_s) \Delta T}{E_s t_s^2}$$

r_i	Curvature of film
E_i	Elastic modulus of film
t_i	Thickness of film
α_i	Thermal expansion coefficient of film
α_s	Thermal expansion coefficient of substrate
ΔT	Temperature between crystallization and transformation
E_s	Elastic modulus of the substrate
t_s	Thickness of the substrate

This equation shows that the radius of curvature is directly proportional to the elastic modulus of the substrate. As voltage is applied to either of these substrates, due to the d_{31} coefficient of the piezoelectric, the film/substrate stack will attempt to increase the bow/radius of curvature. A stiffer substrate will resist the shape change more than one with a lower elastic modulus. Presumably this clamping of the film, imposed by the substrate, pins domains by increasing the activation energies in the energy landscape. Thus, it follows that by changing the elastic properties of the substrate, the propensity for field-induced domain reorientation should also change.

However, there are relatively few studies in the literature which focus on ferroelectric properties as a function of the elastic properties in the underlying materials stack. It has been reported that PZT bilayers demonstrated an increase in piezoelectric properties when a tetragonal PZT thin film when fabricated on top of a rhombohedral PZT; this was proposed to decouple the film from the mechanical boundary constraints of the substrate [20].

Even beyond the utilization for different elastic layers, there are no studies which investigate the role of ferroelastic reorientation for films on different substrates. Thus, to provide more information about how the elastic constraints of the substrate affect domain wall motion,

two films were prepared on substrates with different elastic properties. *In situ* XRD was then used to assess how the substrate effected the ability of the domains to reorient. This was then linked to ferroelectric and piezoelectric properties of the films.

3.3.2 Solution Processing on Silicon and Glass Substrates

In order to study the effect of the elastic properties of the substrate on domain reorientation, 950 nm thick films of CSD PZT30/70 doped with 1% Mn were deposited on two platinized substrates, silicon and Corning Eagle glass. A thermally oxidized silicon substrate (NOVA Corporation) was selected and a bottom electrode of 30 nm Ti/100 nm Pt was sputter deposited on the two substrates at 150 °C. This method has been shown to produce bottom electrodes with good adhesion to the glass substrate. Following this, the PZT solution was spun onto the wafers using the process described in Chapter 3. The same number of solution layers was used for both substrates.

The lower thermal conductivity of the glass sample required minor alternations in the thermal cycle experienced between the two films. The film grown on silicon had two five minute pyrolysis steps and a 1 minute crystallization step, identical to the thermal cycles used for the above experiments. Due to the lower thermal conductivity of the glass substrate, however, the pyrolysis steps were increased to 10 minutes each to ensure good density. While this was enough to densify the films, it was found this thermal treatment, with only a 1 minute crystallization step, did not vaporize excess Pb as efficiently in the films on glass. As a result, these films experienced increased leakage and lower breakdown fields. Increasing the crystallization time to 2 minutes reduced this problem and made the films suitable for testing. Top down and cross-sectional FESEM micrographs, Figure 3.20, show phase pure PZT films with good density. Both films were crystallized at the same temperature, 650 °C.

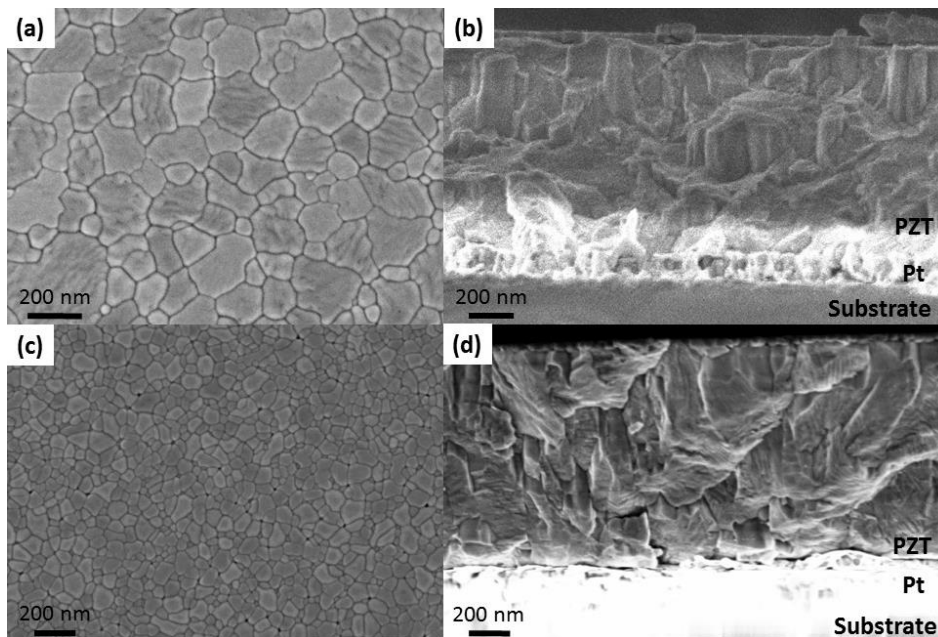


Figure 3.20. FESEM micrographs of the film on glass (a, b) and on silicon (c, d)

The films were not fully textured although both show predominately 101/110 peaks, as shown in Figure 3.20. The difference in film texture will give rise to a difference in the intergranular stress experienced upon application of electric field. This stress will provide a restoring force upon release of field in addition to the restoring force provided by the substrate. Intergranular stress has previously been shown to contribute to the field dependence of the piezoelectric strain in polycrystalline ceramics; as one grain strains upon actuation, it puts a stress on neighboring grains of different orientations [59], [60]. Here, both films are fiber textured, so this effect should be reduced compared to bulk ceramics. As the film on silicon has a larger distribution of grain orientations, an increased field dependence of the intrinsic component would be expected for this film. The additional strain due to this stress will also be reversible and will be observed mainly at high fields. Additionally, as both films are expected to experience some degree of intergranular stress upon actuation, this effect is expected to be less important than the difference in elastic modulus between the two films.

The as-deposited films show good electrical properties on the long strip electrodes. As mentioned previously, due to the difference in Pb volatilization seen on the two substrates, the films on glass showed electrical characteristics consistent with small amounts of excess Pb. While the leakage current density was low enough to enable X-ray diffraction measurements, it was higher for the films on glass than those on silicon. However, both exhibit well saturated P–E loops with remanent polarizations $> 25 \mu\text{C}/\text{cm}^2$ and a dielectric constant of 445 (silicon) and 380 (glass) with a loss of $< 2\%$ when measured at 1 kHz with an ac signal of 30 mV. The electrical data on the as-deposited films is shown in Figure 3.21. The squarer loops for the films on glass suggest a lower residual tensile stress state.

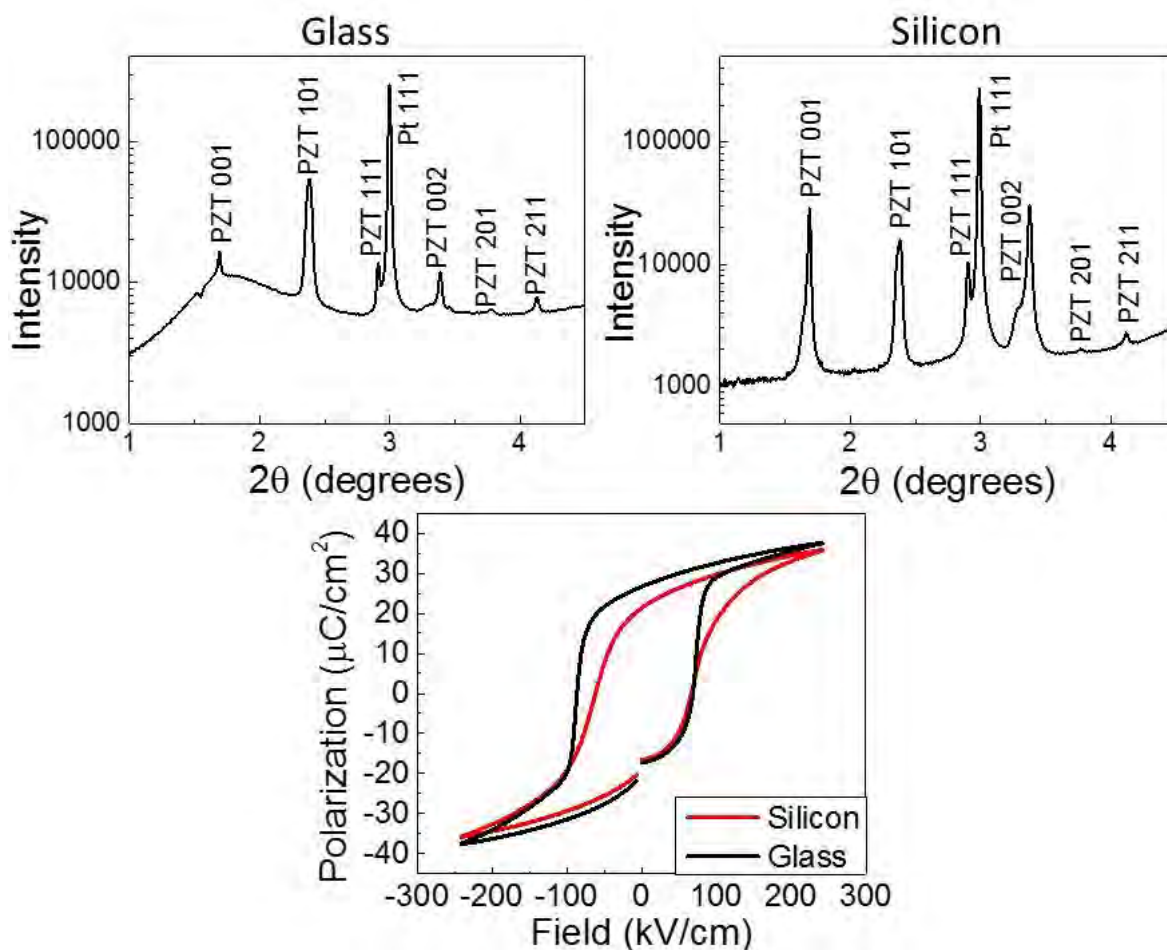


Figure 3.21. XRD plots of the films on silicon and glass (top, $\lambda=0.11798 \text{ \AA}$) and the P–E loops for both films showing slightly higher P_r and P_{max} for the film on glass.

The measurement set up at beamline 11-ID-C is the same as described previously. Because there are no released structures in this study, the two voltage cycles were not necessary. The voltage was increased in steps of $0.5 V_c$ ($V_c \sim 7 \text{ V}$, $E_c \sim 73 \text{ kV/cm}$ for the film on silicon, $V_c \sim 6 \text{ V}$, $E_c \sim 63 \text{ kV/cm}$ for the film on glass) up to $3 V_c$ and then decreased in steps of $1 V_c$, as seen in Figure 3.22. Again, the leakage current density was monitored during irradiation and remained below $\sim 10^{-5} \text{ A/cm}^2$ for all measurements.

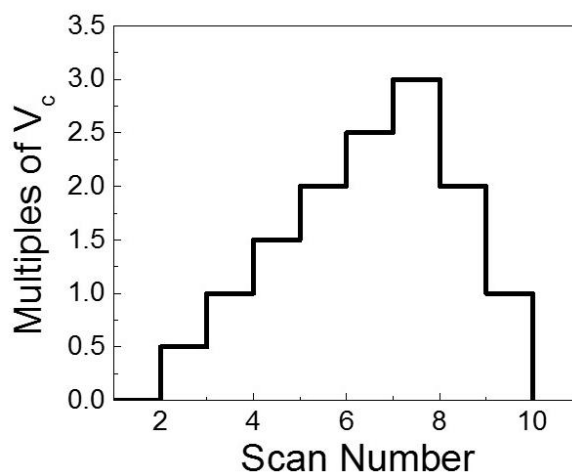


Figure 3.22. Voltage sequence experienced by the films used for investigating the role of the elastic properties of the substrate on domain reorientation with applied field.

3.3.3 Processing Raw Data for Films on Silicon and Glass Substrates

The example 2D diffraction patterns given in Figure 3.23, show the integrated sector data (parallel to the electric field) that was used for these experiments.

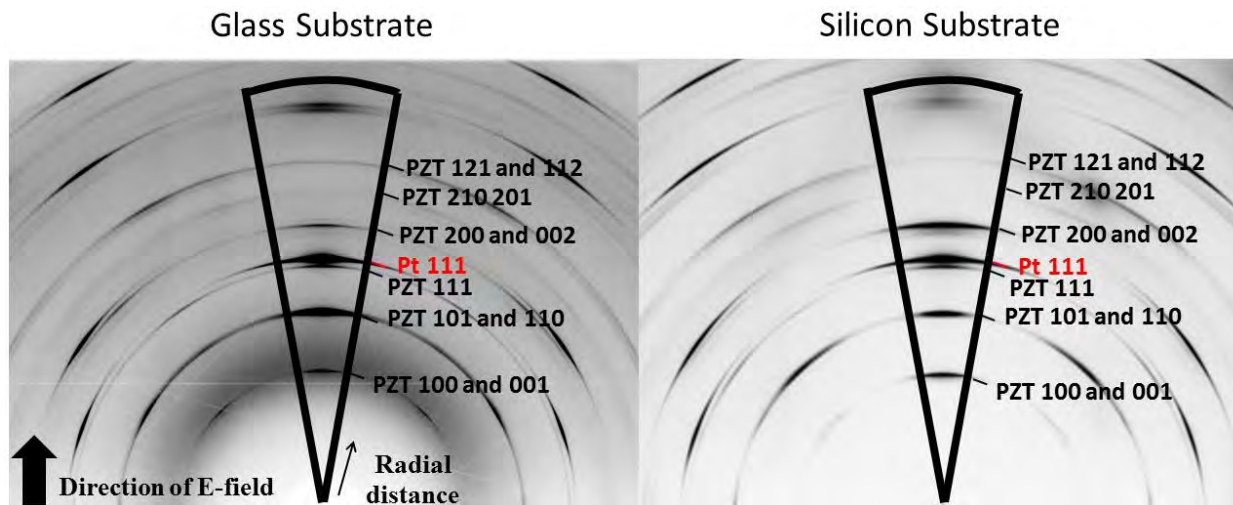


Figure 3.23. A 2D diffraction patterns for the films on glass (left) and on silicon (right). There is a larger intensity in the center of the 2D pattern for the film on glass because of the amorphous substrate. The integrated sector to create a 1D diffraction pattern is outlined and the PZT/Pt peaks are labeled.

Example line profiles from the two substrates are shown in Figure 3.24. Both films have intense 101/110 peaks and so these reflections were used for comparison. Both extracted line profiles shown in Figure 3.24 demonstrate clear domain reorientation with field.

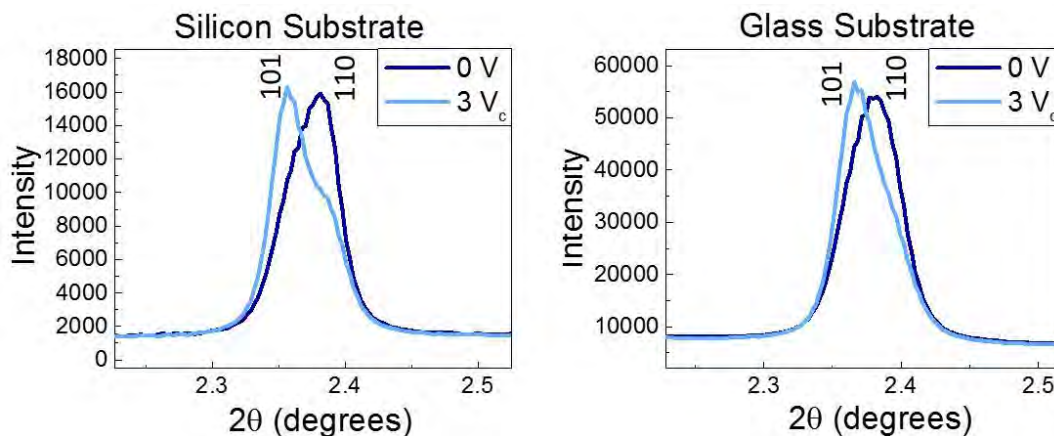


Figure 3.24. Line profiles extracted from the 2D diffraction patterns at 0 V and 3 V_c for the films on both substrates.

A comparison regarding domain reorientation in these films was performed after fitting the diffraction profiles. Several profiles were investigated using Mathematica; the best fit for both films at all voltages was achieved using two pseudo-Voigt functions in which the full width half max (FWHM) is constrained to be the same between the two reflections. As the FWHM will be dependent on the size of the coherent diffraction region, which may be a function of domain

size, rather than grain size, there is a chance that this constraint is too simplistic. However, allowing unconstrained FWHM resulted in excessive correlation of the fitting parameters. An example of one of the fits for the silicon film measured at 3 V_c is shown in Figure 3.25. To calculate domain reorientation, the fitted functions were integrated using analytical integration from $-\infty$ to $+\infty$.

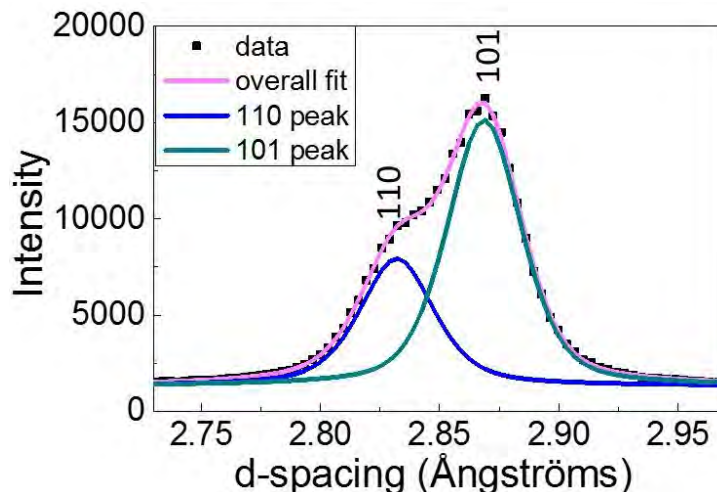


Figure 3.25. Example fitted data for the 110/101 peaks for the film on silicon measured at 3 V_c using two pseudo-Voigt functions where the FWHM is constrained to be the same.

3.3.4 Domain Reorientation in Films on Different Substrates

The volume fraction of 101/110 domains can be calculated using the same methods described in all previous sections. The equation for the volume fraction of 101 domains is shown in Equation 3.8.

Equation 3.8

$$v_{101} = \frac{2 \frac{I_{101}}{I'_{101}}}{\frac{I_{110}}{I'_{110}} + 2 \frac{I_{101}}{I'_{101}}}$$

Here, I_{hkl} is the integrated intensity while I'_{hkl} is the reference intensity from the powder diffraction file ($I'_{110} = 465$, $I'_{101} = 999$) [45]. In this case, the 101 peaks were chosen as they

increase in volume fraction as field is applied which makes the data more intuitive. Since the 101 peaks also include the 011 reflections, a factor of two is added to the numerator. This is analogous to the equation for volume fraction 200 domains shown in equation 3.2. The volume fraction for 101 reflections for the films on silicon and glass is shown in Figure 3.26. While the films have different amounts of $\{101\}$ texture, this method investigates only the intensity exchange within this family of planes. The volume fraction of 101/110 domains is calculated with respect to only the intensities of the $\{110\}$ family. It is clear (as seen in Figure 3.25) that the film on glass has a higher fraction of 101 domains compared to the film on silicon. This is expected due to the slightly higher thermal expansion coefficient of the glass substrate compared to Si, putting the film into a lower tensile stress state (see Table 3.4). However the difference is only a 2 vol% increase on 101 domains for the film on glass.

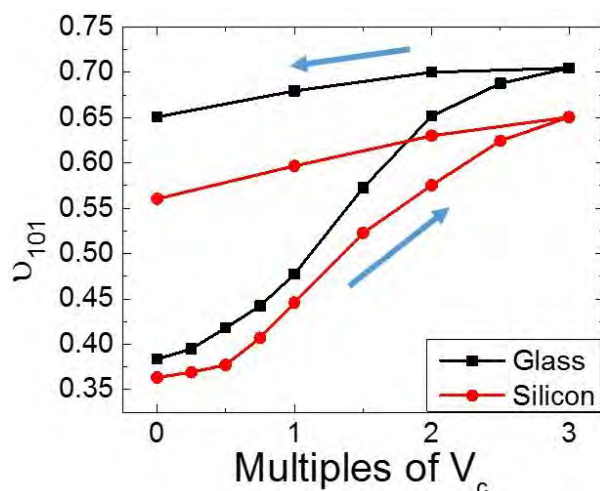


Figure 3.26. The volume fraction of 101 domains as a function of field for the films on silicon and on glass.

The difference in initial volume fraction between the two films is small, suggesting the difference in strain is similarly modest. The strain can be calculated using the difference in thermal expansion coefficients between the film and the substrate and multiplying it by the difference between the crystallization temperature and the Curie temperature. The thermal expansion coefficients for the two substrates are shown in Table 3.4. The thermal expansion

coefficient of PZT in the paraelectric phase (above the Curie temperature) is $9.4 \times 10^{-6}/K$ and can be used to calculate the thermal strain at the transition to ferroelectric PZT using the Equation 3.9 [58].

Equation 3.9

$$\varepsilon_{thermal} = \int_{375^{\circ}C}^{650^{\circ}C} (\alpha_{PZT}(T) - \alpha_{substrate}(T)) dT$$

The strain at the phase transition will influence the resulting domain state. The calculated values for thermal strain are shown in Table 3.4. As shown by Chen, these thermal strains do not differ by enough to change the equilibrium phase [61]. Due to this, the difference in initial texture of the film is expected to have a comparatively modest effect on the conclusions.

Table 3.4. Material Properties of the Substrates

Substrate	Thermal Expansion	Thermal Strain	Elastic Modulus
Silicon	$2.6 \times 10^{-6} K^{-1}$ [62]	0.00187	130 GPa [63]
Corning Eagle Glass	$3.6 \times 10^{-6} K^{-1}$ [64]	0.00160	73.6 GPa [63]

The substrates were chosen to have significantly different elastic moduli. In this case, silicon has a Young's modulus about 1.76 times the Young's modulus of Corning Eagle glass, shown in Table 3.4. Equation 3.10 was used to quantify the change in volume fraction of reoriented domains as a function of field.

Equation 3.10

$$\eta_{101} = \left(\frac{2 \frac{I_{101}}{I'_{101}}}{\frac{I_{110}}{I'_{110}} + 2 \frac{I_{101}}{I'_{101}}} \right) - \left(\frac{2 \frac{I_{101}}{I'_{101}}}{\frac{I_{110}}{I'_{110}} + 2 \frac{I_{101}}{I'_{101}}} \right)^{0 \text{ field}}$$

The volume fraction of reoriented domains as a function of field is shown in Figure 3.27 for films both on glass and on silicon. The effect of intergranular stress should be slightly enhanced in the film on silicon at high fields. However, it is seen that the films on glass show a

slight increase, approximately 3.4 vol%, in the amount of domain reorientation at applied field. Higher amounts of domain reorientation for the film on glass are due to the lower substrate elastic modulus reducing the pinning of domains and enabling increased 90° domain wall motion.

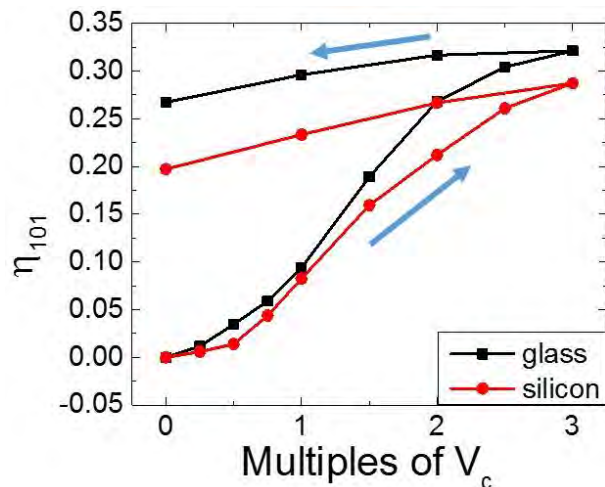


Figure 3.27. Volume fraction of reoriented 101 domains as a function of field for the films on glass and on silicon

Perhaps more interesting than the behavior at high voltage is the response of the films as field is removed. It is expected that as the restoring force for domains is removed (i.e. from the substrate), the domains should show less propensity for backswitching. This should be a function of the elastic properties of the substrate. In the film on glass, approximately 5.4 vol% of domains that reoriented to [101] with applied field relaxed back to [110] upon release of field. In films on silicon, about 9 vol% of domains switch back. From this it is clear that the response of the film on silicon is more reversible upon release of field. This is consistent with the P–E data, shown in Figure 3.21, where a steeper slope top of the loop is observed for decreasing field in the film on silicon. Interestingly, the ratio of the backswitching in films on silicon to glass is about 1.67. The similarity of this to the difference in the Young's moduli suggests that the two are related.

To better understand the response of the films after poling, the Rayleigh characteristics of the films were investigated. The films were poled at 3 V_c for 20 minutes. After 90 minutes, the

Rayleigh behavior was measured at 1 kHz; the results are shown in Table 3.5. The errors presented in the table are errors from fitting the linear region of the data.

Table 3.5. Rayleigh Behavior of Films Measured at 1 kHz

	Silicon	Glass
$\epsilon_{\text{initial}}$	457 ± 0.69	401 ± 0.25
alpha (cm/kV)	4.2 ± 0.06	2.01 ± 0.02
alpha/ $\epsilon_{\text{initial}}$ (cm/kV)	0.0969 ± 0.0014	$0.045 \pm 4 \times 10^{-4}$

The $\epsilon_{\text{initial}}$ values are slightly different, which is expected due to the difference in thermal expansion coefficients producing a higher concentration of [110] relative to [101] domains in the film on silicon. Moreover, the alpha is consistently higher in PZT films on silicon. This might seem surprising since increased 90° domain reorientation was observed in the film on glass. The higher alphas are believed to be related to the saturation of the domain alignment. In films on glass, the domains are closer to their saturated values and therefore do not contribute as much to the irreversible Rayleigh behavior during ac field cycling. Conversely, films on silicon, due to higher amounts of backswitching seen after poling, are further away from their saturated domain alignment and thus may have more mobile wall populations and higher alpha values.

To evaluate how the more saturated domain state in the glass sample affects piezoelectric properties, $e_{31,f}$ values were measured using the wafer flexure method discussed elsewhere [26], [48]. Both samples were poled just prior to the measurement. The values for $e_{31,f}$ reported in Table 3.6 are not statistically different from each other. Still, the silicon sample has a much higher {001} Lotgering factor, also shown in Table 3.6. In oriented polycrystalline bulk ceramics such as $0.72\text{Pb}(\text{Mg}_{1/3}\text{Nb}_{2/3})\text{O}_3\text{-}0.28\text{PbTiO}_3$ [65], $\text{Na}_{0.5}\text{Bi}_{0.5}\text{TiO}_3\text{-BaTiO}_3$ [66], and $\text{Sr}_{0.53}\text{Ba}_{0.47}\text{Nb}_2\text{O}_6$ [67], it was shown that, below a Lotgering factor of ~70%, there is an

approximately linear increase in the piezoelectric coefficient with {001} texture. It is believed that the increased ability to pole the film on glass enables higher piezoelectric coefficients than otherwise would have been possible with the films texture.

Table 3.6 $e_{31,f}$ and Lotgering Values for PZT on Silicon and Glass

	$e_{31,f}$ (C/m ²)	{001} Lotgering Factor
Silicon	-5.7 ± 0.6	64%
Glass	-5.9 ± 0.6	-13%

3.3.5 Summary of the Role of the Elastic Properties of the Substrate

The 101/110 reflections of PZT thin films were investigated using synchrotron X-ray diffraction to examine the changes in domain reorientation as a function of the elastic properties of the substrate. Films were deposited on silicon and glass substrates and it was found that there was a modest increase in the reorientation of 101 domains at applied field (~ 3.4 vol% at $3 V_c$) on a more compliant substrate. Furthermore, it was found that the backswitching of domains occurred in a similar ratio to the ratio of the Young's moduli of the substrate material. When piezoelectric properties of the two films were probed, $e_{31,f}$ between the films was found to be within error, despite the difference in textures. From this, it is concluded that the elastic properties of the substrate play a significant role in poling and the resulting Rayleigh characteristics of the films.

3.4 References

- [1] G. L. Smith, J. S. Pulskamp, L. M. Sanchez, D. M. Potrepka, R. M. Proie, T. G. Ivanov, R. Q. Rudy, W. D. Nothwang, S. S. Bedair, C. D. Meyer, and R. G. Polcawich, "PZT-Based Piezoelectric MEMS Technology," *J. Am. Ceram. Soc.*, vol. 95, no. 6, pp. 1777–1792, 2012.
- [2] P. Muralt, R. G. Polcawich, and S. Trolier-McKinstry, "Piezoelectric Thin Films for Sensors, Actuators, and Energy Harvesting," *MRS Bull.*, vol. 34, pp. 658–664, 2009.
- [3] S. Trolier-McKinstry and P. Muralt, "Thin Film Piezoelectrics for MEMS," *J. Electroceramics*, vol. 12, no. 1/2, pp. 7–17, Jan. 2004.
- [4] F. Griggio, S. Jesse, A. Kumar, O. Ovchinnikov, H. Kim, T. N. Jackson, D. Damjanovic, S. V. Kalinin, and S. Trolier-McKinstry, "Substrate Clamping Effects on Irreversible Domain Wall Dynamics in Lead Zirconate Titanate Thin Films," *Phys. Rev. Lett.*, vol. 108, no. 15, p. 157604 1–5, 2012.
- [5] F. Xu, S. Trolier-McKinstry, W. Ren, B. Xu, Z.-L. Xie, and K. J. Hemker, "Domain Wall Motion and its Contribution to the Dielectric and Piezoelectric Properties of Lead Zirconate Titanate Films," *J. Appl. Phys.*, vol. 89, no. 2, p. 1336, 2001.
- [6] F. Xu, F. Chu, and S. Trolier-McKinstry, "Longitudinal Piezoelectric Coefficient Measurement for Bulk Ceramics and Thin Films Using Pneumatic Pressure Rig," *J. Appl. Phys.*, vol. 86, no. 1, p. 588, 1999.
- [7] J. L. Jones, M. Hoffman, J. E. Daniels, and A. J. Studer, "Direct Measurement of the Domain Switching Contribution to the Dynamic Piezoelectric Response in Ferroelectric Ceramics," *Appl. Phys. Lett.*, vol. 89, no. 9, p. 092901, 2006.
- [8] M. Eatough, D. Dimos, B. A. Tuttle, W. L. Warren, and R. Ramesh, "A Study of Switching Behavior in PZT Thin Films Using X-ray Diffraction," *Mat. Res. Soc. Symp. Proc.*, vol. 361, pp. 111–116, 1995.
- [9] N. Bassiri-Gharb, I. Fujii, E. Hong, S. Trolier-McKinstry, D. V. Taylor, and D. Damjanovic, "Domain Wall Contributions to the Properties of Piezoelectric Thin Films," *J. Electroceramics*, vol. 19, no. 1, pp. 47–65, 2007.
- [10] F. Griggio and S. Trolier-McKinstry, "Grain Size Dependence of Properties in Lead Nickel Niobate-Lead Zirconate Titanate Films," *J. Appl. Phys.*, vol. 107, no. 2, pp. 1–8, 2010.
- [11] S. Li, W. Cao, and L. E. Cross, "The Extrinsic Nature of Nonlinear Behavior Observed in Lead Zirconate Titanate Ferroelectric Ceramic," *J. Appl. Phys.*, vol. 69, no. 10, pp. 7219–7224, 1991.

- [12] S. Trolier-McKinstry, N. B. Gharb, and D. Damjanovic, "Piezoelectric Nonlinearity due to Motion of 180° Domain Walls in Ferroelectric Materials at Subcoercive Fields: A Dynamic Poling Model," *Appl. Phys. Lett.*, vol. 88, no. 20, pp. 0–3, 2006.
- [13] R. J. Zednik, A. Varatharajan, M. Oliver, N. Valanoor, and P. C. McIntyre, "Mobile Ferroelastic Domain Walls in Nanocrystalline PZT Films: The Direct Piezoelectric Effect," *Adv. Funct. Mater.*, vol. 21, no. 16, pp. 3104–3110, 2011.
- [14] A. Kholkin, "Non-Linear Piezoelectric Response in Lead Zirconate-Titanate (PZT) Films," *Ferroelectrics*, vol. 238, no. 1, pp. 235–243, 2000.
- [15] A. L. Kholkin, M. L. Calzada, P. Ramos, J. Mendiola, and N. Setter, "Piezoelectric Properties of Ca-modified PbTiO₃ Thin Films," *Appl. Phys. Lett.*, vol. 69, no. 23, pp. 3602–3604, 1996.
- [16] K. S. Lee, Y. K. Kim, S. Baik, J. Kim, and I. S. Jung, "In Situ Observation of Ferroelectric 90° Domain Switching in Epitaxial Pb(Zr,Ti)O₃ Thin Films by Synchrotron X-ray Diffraction," *Appl. Phys. Lett.*, vol. 79, no. 15, pp. 2444–2446, 2001.
- [17] M. Kohli, P. Muralt, and N. Setter, "Removal of 90° Domain Pinning in (100) Pb(Zr_{0.15}Ti_{0.85})O₃ Thin Films by Pulsed Operation," *Appl. Phys. Lett.*, vol. 72, no. 24, pp. 3217–3219, 1998.
- [18] S. Bühlmann, B. Dwir, J. Baborowski, and P. Muralt, "Size Effect in Mesoscopic Epitaxial Ferroelectric Structures: Increase of Piezoelectric Response with Decreasing Feature Size," *Appl. Phys. Lett.*, vol. 80, no. 17, pp. 3195–3197, 2002.
- [19] V. Nagarajan, A. Stanishevsky, L. Chen, T. Zhao, B. T. Liu, J. Melngailis, A. L. Roytburd, R. Ramesh, J. Funder, Z. Yu, R. Droopad, and K. Eisenbeiser, "Realizing Intrinsic Piezoresponse in Epitaxial Submicron Lead Zirconate Titanate Capacitors on Si," *Appl. Phys. Lett.*, vol. 81, no. 22, pp. 4215–4217, 2002.
- [20] V. Anbusathaiah, S. Jesse, M. A. Arredondo, F. C. Kartawidjaja, O. S. Ovchinnikov, J. Wang, S. V. Kalinin, and V. Nagarajan, "Ferroelastic Domain Wall Dynamics in Ferroelectric Bilayers," *Acta Mater.*, vol. 58, no. 16, pp. 5316–5325, 2010.
- [21] K. Lee, K. Kim, S. J. Kwon, and S. Baik, "Two-Dimensional Planar Size Effects in Epitaxial PbTiO₃ Thin Films," *Appl. Phys. Lett.*, vol. 85, no. 20, pp. 4711–4713, 2004.
- [22] H. Morioka, K. Saito, H. Nakaki, R. Ikariyama, T. Kurosawa, and H. Funakubo, "Impact of 90° Domain Wall Motion in Pb(Zr_{0.43}Ti_{0.57})O₃ Film on the Ferroelectricity Induced by an Applied Electric Field," *Appl. Phys. Express*, vol. 2, no. 4, pp. 0414011–0414013, 2009.
- [23] T. Fujisawa, H. Nakaki, R. Ikariyama, T. Yamada, M. Ishikawa, H. Morioka, and H. Funakubo, "Crystal Structure and Electrical Property Comparisons of Epitaxial

- Pb(Zr,Ti)O₃ Thick Films Grown on (100) CaF₂ and (100) SrTiO₃ Substrates,” *J. Appl. Phys.*, vol. 105, no. 6, p. 061614, 2009.
- [24] B. A. Tuttle, J. A. Voigt, T. J. Garino, D. C. Goodnow, R. W. Schwartz, D. L. Lamppa, T. J. Headley, and M. O. Eatough, “Chemically Prepared Pb(Zr,Ti)O₃ Thin Films: The Effects of Orientation and Stress,” *ISAF '92 Proc. Eighth IEEE Int. Symp. Appl. Ferroelectr.*, 1992.
- [25] R. L. Johnson-Wilke, R. H. T. Wilke, M. Wallace, A. Rajashekhar, G. Esteves, Z. Merritt, J. L. Jones, and S. Trolrier-McKinstry, “Ferroelectric / Ferroelastic Domain Wall Motion in Dense and Porous Tetragonal Lead Zirconate Titanate Films,” *IEEE Trans. Ultrason. Ferroelectr. Freq. Control*, vol. 62, no. 1, pp. 46–55, 2015.
- [26] J. F. Shepard, P. J. Moses, and S. Trolrier-McKinstry, “The Wafer Flexure Technique for the Determination of the Transverse Piezoelectric Coefficient (d_{31}) of PZT Thin Films,” *Sensors Actuators A Phys.*, vol. 71, no. 1–2, pp. 133–138, 1998.
- [27] J. L. Jones, E. B. Slamovich, and K. J. Bowman, “Domain Texture Distributions in Tetragonal Lead Zirconate Titanate by X-ray and Neutron Diffraction,” *J. Appl. Phys.*, vol. 97, no. 3, p. 034113, 2005.
- [28] S. Wan and K. Bowman, “Modeling of Electric Field Induced Texture in Lead Zirconate Titanate Ceramics,” *J. Mater. Res.*, vol. 16, no. 08, pp. 2306–2313, 2001.
- [29] W. Zhu, I. Fujii, W. Ren, and S. Trolrier-McKinstry, “Domain Wall Motion in A and B Site Donor-Doped Pb(Zr_{0.52}Ti_{0.48})O₃ Films,” *J. Am. Ceram. Soc.*, vol. 95, no. 9, pp. 2906–2913, 2012.
- [30] Private communication Betul Akkopru-Akgun.
- [31] G. S. Wang, D. Rémiens, C. Soyer, E. Dogheche, and E. Cattan, “The Effect of LaNiO₃ Bottom Electrode Thickness on Ferroelectric and Dielectric Properties of (100) Oriented PbZr_{0.53}Ti_{0.47}O₃ films,” *J. Cryst. Growth*, vol. 284, no. 1–2, pp. 184–189, 2005.
- [32] L. Qiao and X. F. Bi, “Strain State, Microstructure and Electrical Transport Properties of LaNiO₃ Films Grown on Si Substrates,” *J. Phys. D. Appl. Phys.*, vol. 41, no. 19, p. 195407, 2008.
- [33] H. Mace, H. Achard, and L. Peccoud, “Reactive Ion Etching of Pt/PZT/Pt Ferroelectric Thin Film Capacitors in High Density DECR Plasma,” *Micron Eng.*, vol. 29, pp. 45–48, 1995.
- [34] K. P. Lee, “Dry Etching of BaSrTiO₃ and LaNiO₃ Thin Films in Inductively Coupled Plasmas,” *J. Electrochem. Soc.*, vol. 146, no. 10, p. 3778, 1999.

- [35] S. Aggarwal, S. R. Perusse, C. W. Tipton, R. Ramesh, H. D. Drew, T. Venkatesan, D. B. Romero, V. B. Podobedov, and A. Weber, "Effect of Hydrogen on Pb(Zr,Ti)O₃-based Ferroelectric Capacitors," *Appl. Phys. Lett.*, vol. 73, no. 14, p. 1973, 1998.
- [36] S. Aggarwal, S. R. Perusse, C. J. Kerr, R. Ramesh, D. B. Romero, J. T. Evans, L. Boyer, and G. Velasquez, "Recovery of Forming Gas Damaged Pb(Nb, Zr, Ti)O₃ Capacitors," *Appl. Phys. Lett.*, vol. 76, no. 7, p. 918, 2000.
- [37] H. F. Winters and J. W. Coburn, "The etching of silicon with XeF₂ vapor," *Appl. Phys. Lett.*, vol. 34, no. 1, pp. 70–73, 1979.
- [38] A. P. Hammersley, "ESRF Internal Report, ESRF97HA02T, FIT2D: An Introduction and Overview," *ESRF Intern. Rep.*, 1997.
- [39] J. E. Daniels, J. L. Jones, and T. R. Finlayson, "Characterization of Domain Structures from Diffraction Profiles in Tetragonal Ferroelastic Ceramics," *J. Phys. D. Appl. Phys.*, vol. 39, no. 24, pp. 5294–5299, 2006.
- [40] C. A. Randall, G. A. Rossetti, and W. Cao, "Spatial Variations of Polarization in Ferroelectrics and Related Materials," *Ferroelectrics*, vol. 150, pp. 163–169, 1993.
- [41] G. A. Rossetti, L. E. Cross, and J. P. Cline, "Structural Aspects of the Ferroelectric Phase Transition in Lanthanum-Substituted Lead Titanate," *J. Mater. Sci.*, vol. 30, pp. 24–34, 1995.
- [42] F. Tsai, V. Khiznichenko, and J. M. Cowley, "High-Resolution Electron Microscopy of 90° Ferroelectric Domain Boundaries in BaTiO₃ and Pb(Zr_{0.52}Ti_{0.48})O₃," *Ultramicroscopy*, vol. 45, pp. 55–63, 1992..
- [43] C.-L. Jia, K. W. Urban, M. Alexe, D. Hesse, and I. Vrejoiu, "Direct Observation of Continuous Electric Dipole Rotation in Flux-Closure Domains in Ferroelectric Pb(Zr,Ti)O₃," *Science*, vol. 331, no. 6023, pp. 1420–1423, 2011.
- [44] T. Key, J. L. Jones, W. F. Shelley, and K. J. Bowman, "Quantifying Domain Textures in Lead Zirconate Titanate Using 022:202 and 220 Diffraction Peaks," *Solid State Phenom.*, vol. 105, pp. 379–384, 2005.
- [45] International Centre for Diffraction Data, in Card 01-070-4261.
- [46] M. D. Nguyen, M. Dekkers, E. Houwman, R. Steenwelle, X. Wan, A. Roelofs, T. Schmitz-Kempen, and G. Rijnders, "Misfit Strain Dependence of Ferroelectric and Piezoelectric Properties of Clamped (001) Epitaxial Pb(Zr_{0.52}Ti_{0.48})O₃ thin films," *Appl. Phys. Lett.*, vol. 99, no. 25, pp. 0–4, 2011.
- [47] M. Wallace, R. L. Johnson-Wilke, G. Esteves, C. M. Fancher, R. H. T. Wilke, J. L. Jones, and S. Trolier-McKinstry, "In Situ Measurement of Increased Ferroelectric/Ferroelastic

- Domain Wall Motion in Declamped Tetragonal Lead Zirconate Titanate Thin Films,” *J. Appl. Phys.*, vol. 117, no. 5, p. 054103, 2015.
- [48] C. Yeager, “PZT Thin Films for Piezoelectric MEMS Mechanical Energy Harvesting,” PhD in Materials Science and Engineering, The Pennsylvania State University, 2015.
- [49] G. Esteves, M. Wallace, R. Johnson-Wilke, C. M. Fancher, R. H. T. Wilke, S. Trolier-McKinstry, and J. L. Jones, “Effect of Mechanical Constraint on Domain Reorientation in Predominantly {111} Textured Lead Zirconate Titanate Films,” *J. Am. Ceram. Soc.*, 2016.
- [50] T. Yamada, J. Yasumoto, D. Ito, O. Sakata, Y. Imai, T. Kiguchi, T. Shiraishi, T. Shimizu, H. Funakubo, M. Yoshino, and T. Nagasaki, “Negligible Substrate Clamping Effect on Piezoelectric Response in (111)-Epitaxial Tetragonal Pb(Zr, Ti)O₃ films,” *J. Appl. Phys.*, vol. 118, no. 7, pp. 072012–6, 2015.
- [51] V. Nagarajan, A. Roytburd, A. Stanishevsky, S. Prasertchoung, T. Zhao, L. Chen, J. Melngailis, O. Auciello, and R. Ramesh, “Dynamics of Ferroelastic Domains in Ferroelectric Thin Films,” *Nat. Mater.*, vol. 2, no. 1, pp. 43–47, 2003.
- [52] A. J. Fox, B. Drawl, G. R. Fox, B. J. Gibbons, and S. Trolier-McKinstry, “Control of Crystallographic Texture and Surface Morphology of Pt/TiO₂ Templates For Enhanced PZT Thin Film Texture,” *IEEE Trans. Ultrason. Ferroelectr. Freq. Control*, vol. 62, pp. 56–61, 2015.
- [53] G. A. C. M. Spierings, G. J. M. Dormans, W. G. J. Moors, and M. J. E. Ulenaers, “Stresses in Pt/Pb(Zr,Ti)O₃/Pt Capacitors Stacks for Integrated Ferroelectric Capacitors,” *J. Appl. Phys.*, vol. 78, no. 3, pp. 1926–1933, 1995.
- [54] C. Ottermann, J. Otto, U. Jeschkowski, O. Anderson, M. Heming, and K. Bange, “Stress of TiO₂ Thin Films Produced by Different Deposition Techniques,” *Mat. Res. Soc. Symp. Proc.*, vol. 308, pp. 69–75, 1993.
- [55] S. C. H. Lin, “Local Stress Measurement in Thin Thermal SiO₂ Films on Si Substrates,” *J. Appl. Phys.*, vol. 43, no. 1, p. 119, 1972.
- [56] D. M. Marincel, H. R. Zhang, J. Britson, A. Belianinov, S. Jesse, S. V. Kalinin, L. Q. Chen, W. M. Rainforth, I. M. Reaney, C. A. Randall, and S. Trolier-McKinstry, “Domain Pinning Near a Single-Grain Boundary in Tetragonal and Rhombohedral Lead Zirconate Titanate Films,” *Phys. Rev. B*, vol. 91, no. 13, pp. 1–12, 2015.
- [57] D. A. Schwartz, T. L. Aldcroft, J. A. Bookbinder, V. Cotroneo, W. N. Davis, W. R. Forman, M. D. Freeman, S. McMuldroch, P. Reid, H. Tananbaum, A. Vikhlinin, S. Trolier-McKinstry, D. Wilke, and R. Johnson-Wilke, “The Square Meter Arcsecond Resolution X-ray Telescope: SMART-X,” *Proc. SPIE*, vol. 8503, p. 850308, 2012.

- [58] C. H. Hsueh, "Thermal Stresses in Elastic Multilayer Systems," *Thin Solid Films*, vol. 418, no. 2, pp. 182–188, 2002.
- [59] D. A. Hall, A. Steuwer, B. Cherdhirunkorn, T. Mori, and P. J. Withers, "A High Energy Synchrotron X-ray Study of Crystallographic Texture and Lattice Strain in Soft Lead Zirconate Titanate Ceramics," *J. Appl. Phys.*, vol. 96, no. 8, pp. 4245–4252, 2004.
- [60] A. Pramanick, D. Damjanovic, J. E. Daniels, J. C. Nino, and J. L. Jones, "Origins of Electro-Mechanical Coupling in Polycrystalline Ferroelectrics During Subcoercive Electrical Loading," *J. Am. Ceram. Soc.*, vol. 94, no. 2, pp. 293–309, Feb. 2011.
- [61] L. Q. Chen, "Phase-Field Method of Phase Transitions/Domain Structures in Ferroelectric Thin Films: A Review," *J. Am. Ceram. Soc.*, vol. 91, no. 6, pp. 1835–1844, 2008.
- [62] R. L. Johnson-Wilke, R. H. T. Wilke, V. Cotroneo, W. N. Davis, P. B. Reid, D. A. Schwartz, and S. Trolier-McKinstry, "Improving Yield of PZT Piezoelectric Devices on Glass Substrates," *Proc. SPIE* vol. 8503, p. 85030A, 2012..
- [63] R. H. T. Wilke, R. L. Johnson-Wilke, V. Cotroneo, S. Mcmudroch, P. B. Reid, D. A. Schwartz, and S. Trolier-McKinstry, "Fabrication of Adjustable Cylindrical Mirror Segments for the SMART-X Telescope," *IEEE Trans. Ultrason. Ferroelectr. Freq. Control*, vol. 61, no. 8, pp. 1386–1392, 2014.
- [64] Corning, "Eagle 2000 Material Information," *Material Information*, 2005. [Online]. Available: [http://www.delta-technologies.com/downloads/Eagle 2000.pdf](http://www.delta-technologies.com/downloads/Eagle%2000.pdf). [Accessed: 01-Jan-2015].
- [65] K. H. Brosnan, "Processing, Properties, and Application of Textured $0.72\text{Pb}(\text{Mg}_{1/3}\text{Nb}_{2/3})\text{O}_3$ - 0.28PbTiO_3 Ceramics," PhD in Materials Science and Engineering, The Pennsylvania State University, 2007.
- [66] H. Yilmaz, "Texturing of $\text{Na}_{1/2}\text{Bi}_{1/2}\text{TiO}_3$ - BaTiO_3 Ceramics by Templated Grain Growth," PhD in Materials Science and Engineering, The Pennsylvania State University, 2002.
- [67] C. Duran, "Fabrication and Electrical Properties of Textured $\text{Sr}_{0.53}\text{Ba}_{0.47}\text{Nb}_2\text{O}_6$ Ceramics Prepared by Templated Grain Growth," PhD in Materials Science and Engineering, The Pennsylvania State Univeristy, 2001.

Chapter 4 PZT Thin Films on a Polymer Substrate

4.1 Introduction to Flexible Piezoelectrics

Flexible piezoelectrics are currently of interest for ultrasound, energy harvesting, and pressure sensing applications [1]–[3] as the mechanical flexibility enables higher sensitivity [4], and, specifically for energy harvesting, lower resonance frequencies for wearable applications [2]. Additionally, using a flexible substrate would enable fabrication of detectors which can conform to surfaces [3], [5].

Where flexible substrates for piezoelectrics are being investigated, many groups utilize piezoelectric materials with low processing temperatures, such as ZnO or polymer piezoelectrics [1], [5]. While the low thermal budgets of these materials provide a wider latitude in choosing substrates, it comes at the price of lower piezoelectric coefficients. For applications in which high sensitivity is critical, materials such as PZT, with large piezoelectric properties, are preferred.

PZT can be deposited on certain flexible substrates, such as Ni foil, without sacrificing the high temperatures which are necessary for crystallization [6]. While PZT films on Ni foils show excellent properties and are useful materials for mechanical energy harvesters, these substrates can be difficult to work with, particularly in a university laboratory setting, due to the propensity for plastic deformation when handled [6], [7]. In addition to flexible Ni foils, there has also been work using thinned silicon substrates to enable good mechanical flexibility for bending radii of 5 mm [8]. A flexible non-volatile PZT memory was fabricated on Si by Kosel *et al.* which was then thinned down to 40 μm , thereby becoming flexible, using dry etching [8].

Polymers are, on the other hand, of interest as passive elastic layers with piezoelectric films, because of their large compliance constants [9]. However, PZT deposition on a polymer

substrate is complicated due to the high crystallization temperatures (typically around 650 °C or higher). Despite these difficulties, several groups have reported measurement of PZT on a flexible, polymer substrate [2], [4], [9]–[11]. Because of difficulties in depositing PZT on a polymer, in these cases, the PZT thin films was first fabricated on a separate substrate, e.g. silicon, MgO, or sapphire, and subsequently transferred to a polymer.

Several approaches have been used including etching (wet or dry) of the substrate or sacrificial layers. Qi *et al.* transferred nanoribbons of PZT from an MgO substrate to ~2 mm of PMDS using a phosphoric acid etch [4]. While this proved successful for nanoribbons, phosphoric acid will etch PZT and releasing large area PZT from MgO substrates using phosphoric acid has been shown to be difficult by other groups [2]. Additionally, Bakaul *et al.* released thin films (40-100 nm) single crystal $\text{PbZr}_{0.20}\text{Ti}_{0.80}\text{O}_3$ from a SrTiO_3 growth substrate onto a polymer film using a 20 nm thick sacrificial etch layer of lanthanum strontium manganite (LSMO) [12]. The LSMO was etched for 12 hours in a solution of potassium iodide, hydrochloric acid and water before being completely released onto a 250 nm thick film of PMMA [12]. No properties were measured. However, post transfer to the silicon substrate it was observed that there was no degradation in the film properties or microstructure [12].

In related work, other groups have fabricated flexible ferroelectrics (other than PZT) using wet or dry etching [13], [14]. In one study, a sacrificial TiO_2 layer was used to transfer BaTiO_3 structures from a silicon substrate to a polymer substrate using a buffered oxide etch (BOE) [15]. Dielectric measurements were performed and ϵ_r was reported to decrease after release. In addition, the losses increased from < 5% on the silicon substrate to almost 20% at 100 Hz on the polymer. One potential reason for this increase in the loss tangent was damage to the BaTiO_3 structures by the aggressive BOE [15]. Jang *et al.* deposited 400 nm and 600 nm

thick BiFeO₃ thin films on silicon substrates [13]. After measurement of the properties, the films were bonded to a polymer membrane and the Si was removed using a dry etching process. P–E loops of released electrodes were compared to the response from electrodes on the silicon substrate. Upon release, films showed 25%-30% lower E_c values, a slight increase in remanent polarization and lower leakage current densities [13]. (Na_{0.5}K_{0.5})NbO₃ (NKN) films fabricated on silicon were transferred to a polyimide substrate by etching away the silicon in a KOH bath [14]. Although the base damaged the film, reducing E_c , P_r , and leakage current density, upon release the material underwent a structural change from pseudocubic to orthorhombic which increased the measured $d_{33,f}$ value from 74 ± 11 pm/V to 120 ± 18 pm/V [14]. Lee *et al.* reported fabricating flexible PZT/graphene based FeFETs by first depositing PZT nanoribbons in silicon and then subsequently removing the ferroelectric by undercutting the silicon using a dry etch. The devices showed good retention values with on/off current ratios differing by approximately a factor of two, even with the flexible film bent to 13% strain [10].

Another popular method for transferring ferroelectric films to polymer substrates is laser lift off (LLO) [9], [11], [16], [17]. Park *et al.* transferred a PZT thin film onto a 125 μm polyethylene terephthalate substrate using this method. The PZT was fabricated on a sapphire substrate and a XeCl laser was used to modify the interface between the PZT and sapphire to enable release [9]. The process was successful and released the PZT with no mechanical degradation or cracks reported. Other groups have also reported using the LLO process on sapphire, glass, or MgO growth substrates, although with damage to the film surface in the absence of a buffer/sacrificial layer [11], [16], [17].

While these methods enable measurements on released films, it would be useful to develop a simple, flexible process to transfer PZT onto a polymer substrate without restricting growth substrate or subjecting the PZT to chemicals which can degrade properties.

Additionally, a comparison of material response between clamped and released films would provide further insight into the role of the substrate. As described in Chapter 3, better knowledge of how clamping by the substrate affects the piezoelectric coefficients should result in the ability to design piezoelectric MEMS devices with increased functionality. Presently, there are no published reports of the d_{33} of a PZT film released from the substrate. Thus, it would be useful to have a measurement of a thin film d_{33} unencumbered by the substrate (e.g. d_{33} , rather than $d_{33,f}$). In particular, this would quantify the magnitude of clamping by the substrate to the reduction of the d_{33} coefficient from bulk to films. It is known that domain wall motion is significantly clamped by the substrate [18], [19]. Moreover, Lefki *et al.* derived a formula for the d_{33} coefficient of films, seen in Equation 3 [20].

$$d_{33,f} = d_{33} - 2d_{31} \frac{s_{13}^E}{s_{11}^E - s_{12}^E}$$

where d_{31} represents the transverse piezoelectric coefficient and s_{11} , s_{12} , and s_{13} are the elastic coefficients of the film. As the second part of the $d_{33,f}$ equation is typically positive, the measured d_{33} of the film is reduced by substrate clamping [20]. Developing a process for release of the film onto the polymer should enable measurements of the true film d_{33} coefficient.

This chapter focuses on developing a process to transfer a PZT thin film, initially deposited on a silicon substrate, onto a thin polymer substrate. The film is deposited on a sacrificial ZnO buffer layer and is released from the substrate using an acetic acid etch to undercut the ZnO. This enabled electrical measurements on clamped and released portions of the

same film and illuminated important processing factors for transferring the ceramic film to a polymer.

4.2 Process for Transfer of PZT onto a Polymer

A schematic illustrating the process flow is shown in Figure 4.1. In short, thin films of Pt electrode/PZT were deposited on a platinized/ Al_2O_3 / ZnO / SiO_2 /silicon substrate. Then a polymer, polyimide PI-2611, was deposited on top of the stack via spin coating. The PZT is deposited in reverse (i.e. what will ultimately become the top-electrode is deposited first) then transferred to the 5 μm thick polymer layer via etching away the ZnO sacrificial layer. That is, after the deposition of the polymer, the ZnO is removed via wet etching, thereby freeing the film/polymer from the silicon substrate. ZnO was chosen as it is readily etched in acetic acid which should not affect the PZT [21]. The process is described in detail below.

A ZnO sacrificial etch layer approximately 50 nm thick was deposited using plasma-enhanced atomic layer deposition (PEALD) onto a thermally oxidized silicon substrate using processing conditions described elsewhere [22]. Following this, a thin film (~5 nm) of PEALD deposited Al_2O_3 was grown. The buffer Al_2O_3 was found to be necessary in order to prevent the ZnO from diffusing into the PZT upon crystallization. While the ZnO will not diffuse through the electrode, it will intermix with PZT in areas without Pt, essentially removing the sacrificial release layer in these regions.

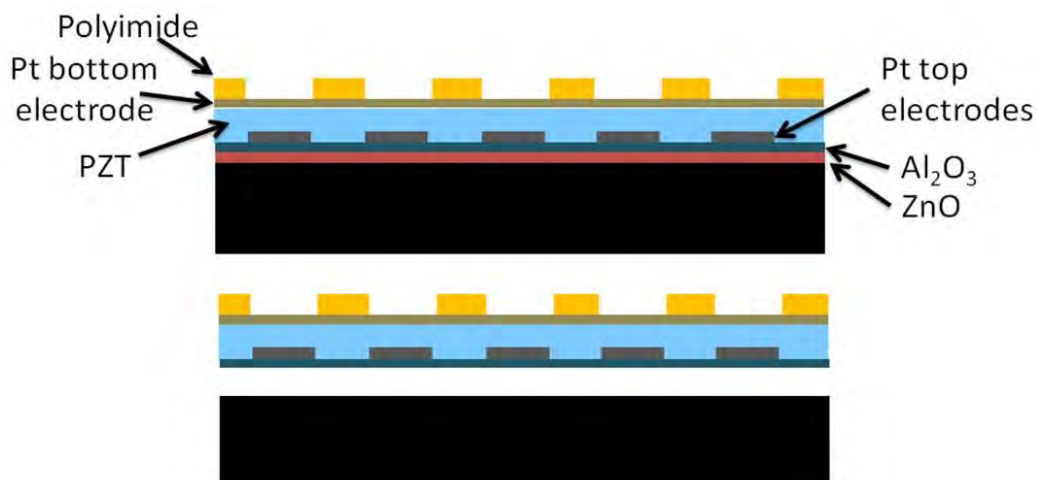


Figure 4.1. A schematic showing the transfer of a thin film of PZT from a silicon substrate to a thin polymer. The metal/PZT/metal stack is deposited on a sacrificial ZnO layer. After fabrication the ZnO is removed via wet etching, freeing the film onto the polymer.

One goal of this experiment was to compare properties of films clamped to a silicon substrate and films in a released state on a thin polymer. In order to keep microstructural variation (such as grain size, defect concentrations, orientation etc.) to a minimum, the same substrate was used to deposit the PZT for both the clamped and released states.

To begin fabrication of the capacitor, 100 nm of Pt was sputter deposited on the $\text{Al}_2\text{O}_3/\text{ZnO}/\text{SiO}_2/\text{silicon}$ stack. A schematic of the Pt design is shown in Figure 4.2 where Pt regions are shown in blue. In the center of the substrate is lithographically patterned Pt (Region A). These circular regions ultimately serve as the top electrode for the released sections. At the edges of the substrate there is blanket Pt which serves as the bottom electrode for the clamped films (Region B).

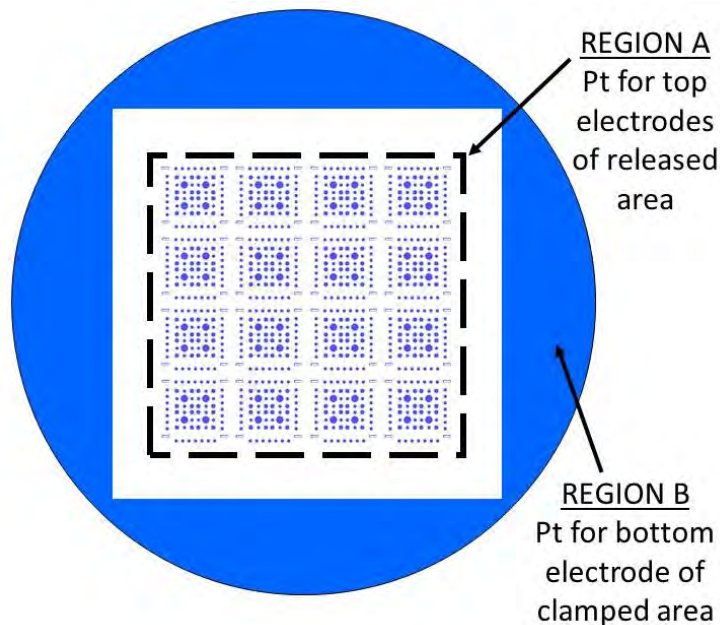


Figure 4.2. Schematic showing the Pt pattern (in blue) for these samples. The center of the wafer has a top electrode pattern, accessible after release, for measurements of the PZT on polymer (Region A). The edges of the wafer has blanket Pt for a common bottom electrode for measurements of clamped PZT (Region B).

Following the Pt deposition, 850 nm of $\text{Pb}(\text{Zr}_{0.52}\text{Ti}_{0.48})_{0.98}\text{Nb}_{0.02}\text{O}_3$ was deposited using CSD (solution batched with 10% excess PbO) in the same manner as described in Chapter 1. Top down and cross-sectional FESEM micrographs of the PZT are shown in Figure 4.3. The as-deposited film shows no evidence of cracking. Next, the area designated for clamped PZT (Region B) was cleaved off. Circular top electrodes were lithographically defined in lift-off resist and 100 nm of Pt was sputter deposited. The rest of the substrate (Region A) is the area designated for released PZT. 100 nm of blanket Pt was sputter deposited on Region A to serve as the bottom electrode.

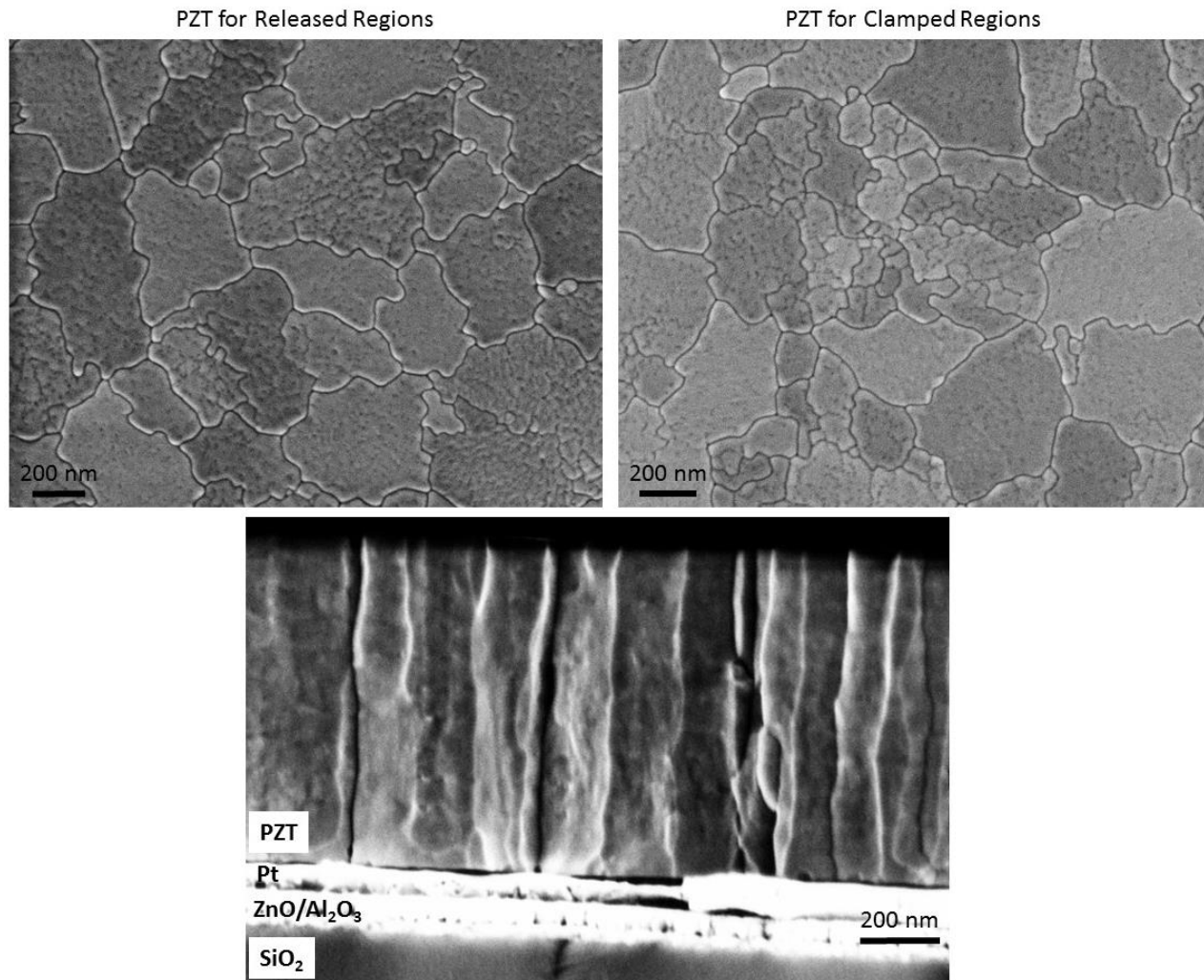


Figure 4.3. Top down and cross sectional FESEM micrographs of the as-deposited film on a silicon substrate. PZT from the regions to be released and from the regions which remained clamped are both phase-pure and crack free. The cross-sectional micrograph, representative of both regions, shows good density and columnar grains. The subtle mottling observed in the top down FESEM is likely the result of small PZT grains boundaries. What appears as more defined grain boundaries in the top-down view is likely to be cluster boundaries.

Finally, 5 μm of polyimide, PI-2611 (HD Microsystems), was spun onto the Si/ZnO/Al₂O₃/Pt/PZT/Pt stack using the following recipe: 300 rpm for 20 seconds, 1000 rpm for 30 seconds and finally 3000 rpm for 40 seconds. The soft bake was done at 80 °C for 5 minutes and the layer was cured at 300 °C (ramp rate of 180 °C/hour) for > 10 hours (overnight) in air [23]. After the polyimide was cured, the samples were diced into small, $\sim 1 \text{ cm}^2$ pieces. The

dicing provided flexibility to try different release procedures. The help of J. I. Ramirez is gratefully acknowledged for the PEALD depositions and polyimide deposition.

The next fabrication steps were to etch the polyimide away from underneath the electrodes, and then to release the film. The polyimide “windows,” shown in the schematic in Figure 4.1 and outlined in Figure 4.4, allow measurement of the capacitor with no substrate. The polyimide was etched in a PlasmaTherm 720 in an oxygen and argon plasma with 200 nm of titanium serving as an etch mask. 15 nm of Pt was deposited on the backside of the polyimide to increase the stiffness and prevent the film from curling to release tensile stress.

The final step in this process was to put the film into a warm ($\sim 110\text{ }^{\circ}\text{C}$) acetic acid bath. The acetic acid easily etches the ZnO, however it should not harm the PZT. This process takes several days even for cm^2 samples such as the ones discussed here since only a small amount of ZnO is exposed to the etchant at a time.

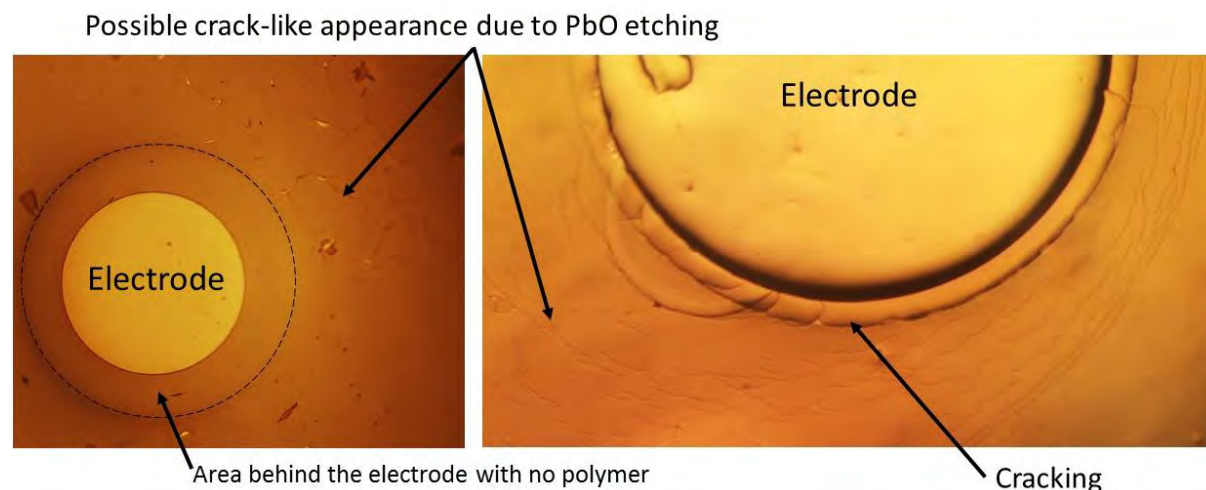


Figure 4.4. Optical microscope pictures of cracking observed on the released film.

The method presented here enabled successful transfer of PZT thin films to polymer substrates. However, it was also found that the films were cracked post release process. Optical microscope images of the cracking can be found in Figure 4.4. The cracks are populated across

the entire film, but are most severe in the areas immediately around electrodes at the boundary of backside polymer (Figure 4.6). Even in films which were not exposed to mechanical bending after release, the cracks were present. Since the films were not cracked prior to release, it is assumed that the slow etch process produced the cracking. Figure 4.5 shows, in a large area sample, the release process as it evolves in solution.

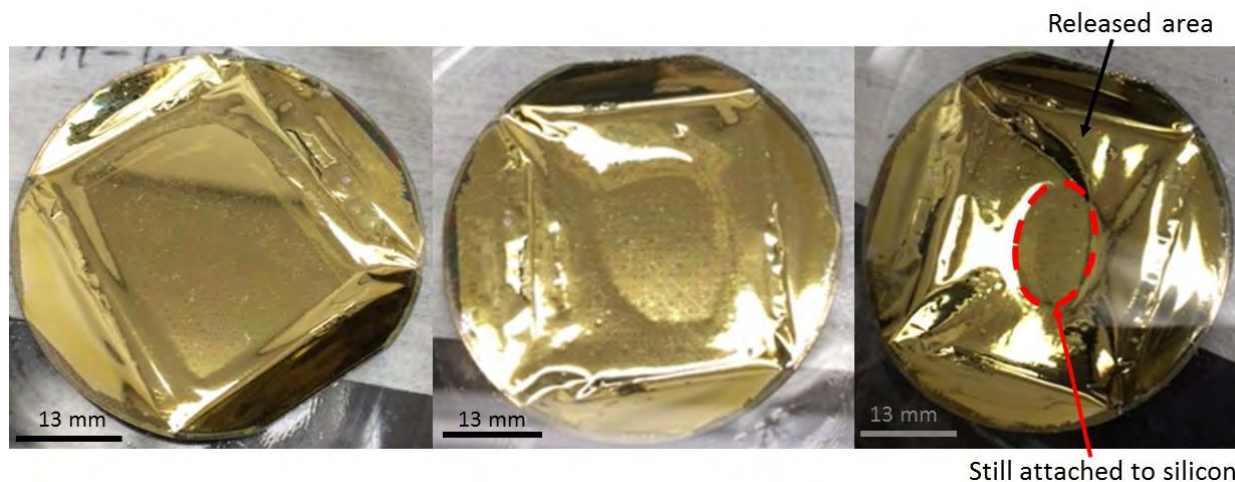


Figure 4.5. Pictures showing the evolution of the film as it is released from the silicon substrate in an acetic acid bath.

There is a large amount of deformation present in the released film, especially at the boundary between material that is released and film still attached to the silicon substrate. It is likely this produces cracks during the release process which propagate with further handling. However, it is also possible the extensive etch in acetic acid dissolved excess PbO which was present in only a few grain boundaries. This would result in grooved grain boundaries with the appearance of cracks. While this might be the case for some of the thinner-looking cracks, there is also definite cracking, shown in Figure 4.6.

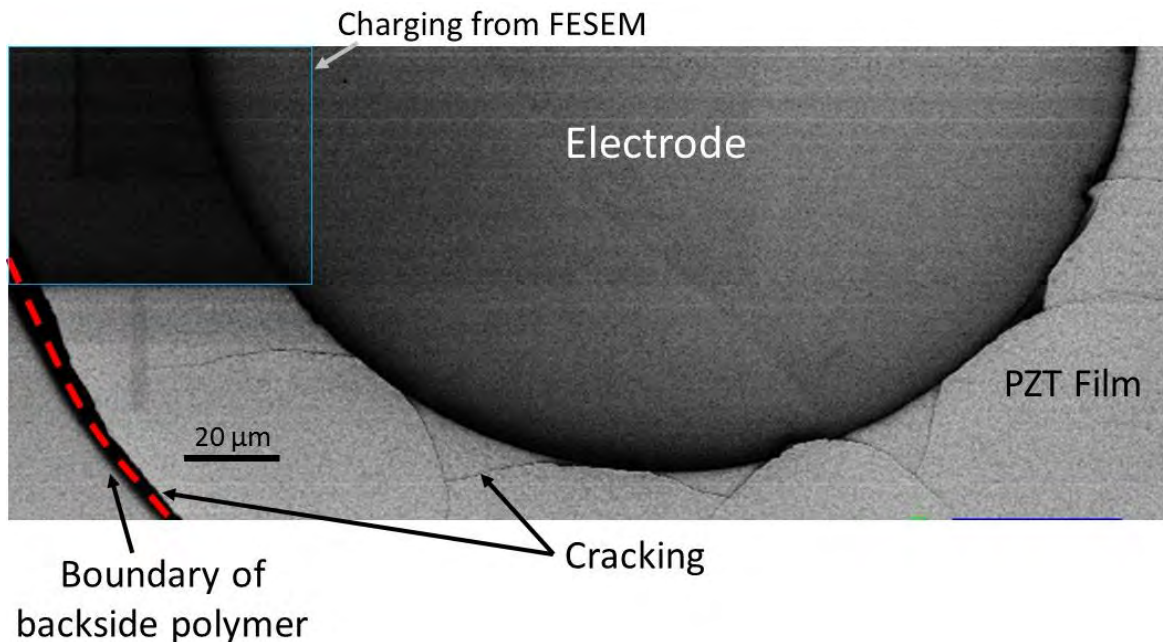


Figure 4.6. FESEM micrograph of an electrode showing cracking. The dark area to the left of the electrode (outlined in blue) is a result of charging from the electron beam. The excessive cracking near the boundary of the backside polymer is highlighted with a red dashed line.

To investigate if the electrodes themselves exhibited the extensive microcracking observed elsewhere on the film, samples were investigated in the FESEM. The electrodes did not show the levels of cracking seen in the unelectroded film in Figure 4.4. This is potentially due to the Pt top electrode, which has a higher stiffness and could reduce the mechanical deformation which caused the cracking. While some of the electrodes did exhibit minor cracking, these types of cracks were observable in the optical microscope and could be avoided when selecting electrodes for measurement. As such, it is believed that the electrical characterization described in the next section represents an uncracked film in clamped and released states. While further improvements in the release process are needed, the dielectric and ferroelectric measurements provide a baseline for the response expected from PZT films released in this manner.

4.3 Characterization of Clamped and Released Films

When measured at 1 kHz with a 30 mV ac signal the clamped film had a dielectric constant of 1075 ($\tan\delta = 0.02$) and the released film had a dielectric constant of 950 ($\tan\delta =$

0.016). Since the films are essentially identical, the difference in dielectric constant can be attributed to the release process. Zednick *et al.* showed that when films are stressed, domain reorientation takes place [24]. In these released films, there is no restoring force from the substrate to cause domains to switch to the in-plane direction imposed by the substrate during fabrication. As such, when the material is deformed, as described above and shown in Figure 4.5, it is possible that domain reorientation takes place, producing more out of plane polarization.

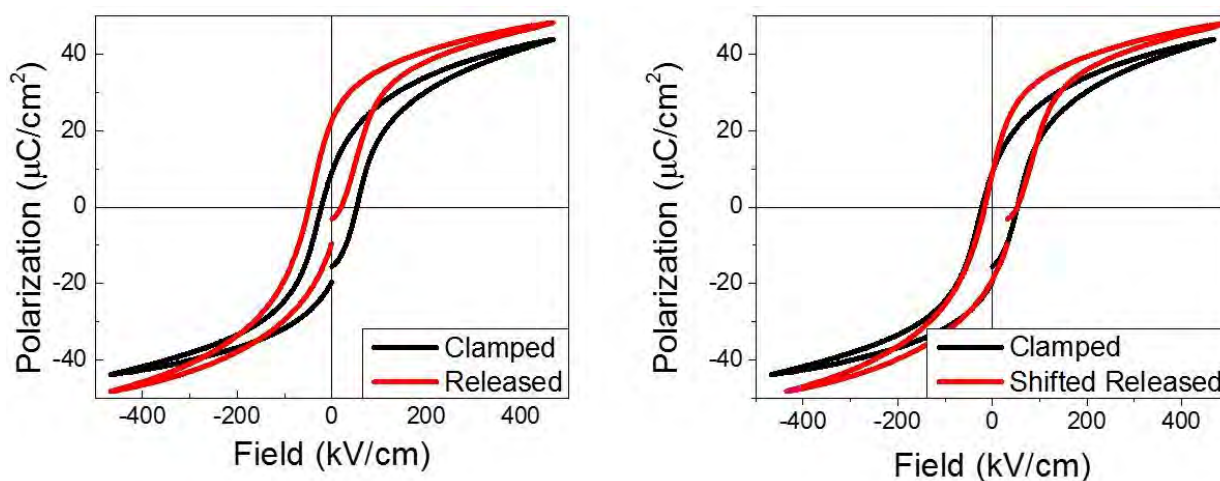


Figure 4.7. Polarization versus field loops for the clamped and released states of the film. The P–E loop on the left represents unaltered data while the released data in the P–E loop on the right has been shifted by the difference in imprint between the two films. The shifted loops shows similar remanent polarizations and coercive fields.

To assess whether this is a realistic possibility, the polarization versus field curves were investigated, as is seen in Figure 4.7. At high fields, the maximum polarization in the released film is higher than in the clamped. Values for the maximum polarization at positive fields are shown in Table 4.1. The increase in polarization is expected as domains should be easier to reorient in declamped samples [19]. Additionally, the P–E loops of released electrodes show both a negative imprint and higher positive remanent polarization compared to clamped electrodes. As such, to compare values for remanent polarization, the average remanent polarization (the average of the positive and negative P_r) is used. Table 4.1 shows these average

values for the clamped and released states measured for a 400 kV/cm field excursion. These numbers are expected to increase at higher fields although the released electrodes crack at fields > 400 kV/cm.

Table 4.1. P-E Characteristics for Clamped and Released Films

	Clamped	Released
P_{max}^+	44 $\mu\text{C}/\text{cm}^2$	48 $\mu\text{C}/\text{cm}^2$
P_r^{avg}	14.3 $\mu\text{C}/\text{cm}^2$	16.3 $\mu\text{C}/\text{cm}^2$
E_c^{avg}	37 kV/cm	34 kV/cm

The average remanent polarization for the released film is slightly larger than for the clamped. This was found to be related, at least in part, to a change in the imprint on release. The imprint seen in the clamped film, approximately 31 kV/cm, is almost identical to the amount of imprint seen in the released films -29 kV/cm, *but in the opposite direction*. While the definitive cause of this shift is unknown, there are a two possibilities. First, the imprint could possibly be from defect dipoles in the film which, due to their small field, align surrounding dipoles, shifting the coercive field slightly. Garten *et al.* showed that imposing a strain gradient greater than 1.3 m^{-1} on a thin film of $\text{Ba}_{0.7}\text{Sr}_{0.3}\text{TiO}_3$ resulted in an imprint of 9.2 kV/cm and that the direction of the imprint was shown to be related to the direction of the applied strain gradient. Furthermore, it was found that the imprint imposed by the strain gradient remained even after the strain was removed [25]. As it is hypothesized that these films experience large amounts of strain during the release process, it is possible this is why the imprint shifts. However, if movement of defects (e.g. oxygen vacancies) are the result of this shift, the imprint should be switchable upon electrical poling. Released films were poled at $3 V_c$ for 20 minutes at 75 °C. This poling

procedure is expected to be aggressive enough to reorient defects such as oxygen vacancies. However, as the P–E data in Figure 4.8 shows, poling at 75 °C does not shift the P–E loop.

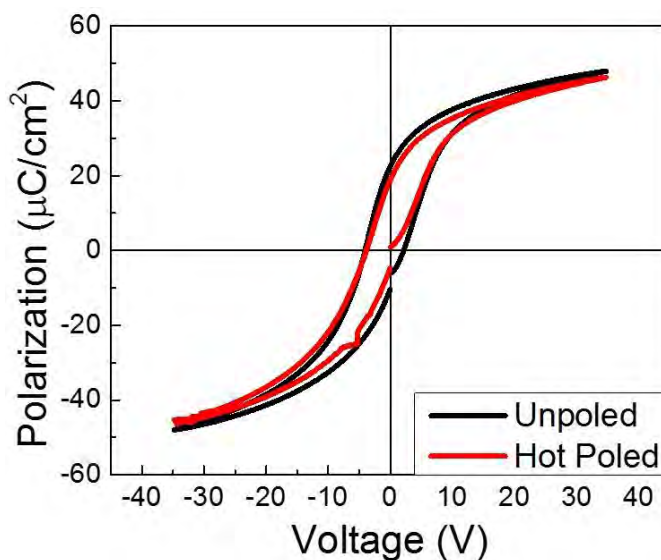


Figure 4.8. P–E loops of an unpoled released electrode and a released electrode which was poled at 3 V_c for 20 minutes at 75 °C. The imprint in the released film does not change with poling.

Considering this, a more likely scenario is that the shift is caused by some kind of compositional gradient in the PZT at the electrode interface it was grown on. As it is known that Pb diffuses into the bottom electrode during heat treatment [26], [27], it is hypothesized that there may be a small compositional difference between the top and bottom electrodes. This could introduce defect dipoles which are more resistant than oxygen vacancies towards migration upon poling. In the clamped case, the area near the bottom electrode would have the compositional gradient whereas in the released case, it would be the area near the top electrode. This seems to be the most likely possibility to explain the differences in imprint.

Interestingly, after shifting the loops to account for the differences in imprint, as seen in the right hand plot in Figure 4.7, the remanent polarization of the released film nearly matches that of the clamped film. While the released film still shows higher amounts of maximum polarization and a squarer loop for high positive fields, at lower fields, the P-E loops show

similar slopes and remanent polarizations. Thus the increase in remanent polarization observed is more a function of the change in imprint and less a function of a changed strain state due to release.

This was unexpected due to the absence of any kind of stiff substrate which might restrict the bending of the film to relieve this stress. In order to better understand the response of the released film, its strain state, and domain response, the Rayleigh behavior was investigated. Both the clamped and released samples were poled at $3 V_c$ for 20 minutes before performing Rayleigh analysis at 1 kHz. The released film had lower values for both ϵ_{init} and α , as seen in Table 4.2.

Table 4.2. Rayleigh Characteristics for Clamped and Released States

The errors shown are from fitting.

	Clamped	Released
ϵ_{init}	1063 ± 1.5	1006 ± 1.3
α (cm/kV)	21.2 ± 0.5	19.2 ± 0.4
α/ϵ_{init} (cm/kV)	$0.0199 \pm 4.7 \times 10^{-4}$	$0.0190 \pm 4 \times 10^{-4}$

Due to the lower Young's modulus of the polymer substrate, it was expected that domain reorientation should be facilitated by the film being free to bend. However the alpha coefficients exhibited by the released films are lower than the alpha coefficients of the clamped film.

Additionally, the α/ϵ_{init} values are within error, suggesting that this is not the case. The as-measured positive remanent polarization in the released films is approximately twice as large as the as-measured positive remanent polarization in the clamped films. From this it can be surmised that domains in the released film have a lower driving force to backswitch upon release in field. As a result, the domain state in the released film after poling should be more saturated. With more domains already aligned with the direction of applied field, the released films have smaller irreversible domain wall contributions and thus lower alpha coefficients.

If the lowered Rayleigh coefficients are due to a difference in the polarization state induced by poling, and not, for instance, a small difference in film thickness between the clamped and released regions, then the Rayleigh coefficients of unpoled films should provide a better understanding of the result of release and how it might affect domain wall motion. This was also investigated. To eliminate any effect of aging on the experiments, P-E loops were performed on both clamped and released electrodes. Starting at 400 kV/cm, the maximum field of the loop was systematically reduced in steps of ~ 25 kV/cm until the films experience only minor loops [28]. This should electrically deage the films (thermal aging was not an option due to the polymer in the released film stack). The Rayleigh characteristics are found in Table 4.3. The released film shows lower ϵ_{init} values, as expected. However, since the films are not poled, the released film was expected to have a higher α . This was not the case, as seen in Table 4.3.

Table 4.3. Rayleigh Characteristics for Unpoled Clamped and Released Samples
The errors shown are from fitting.

	Clamped	Released
ϵ_{init}	1146 ± 1.7	1086 ± 1.7
α (cm/kV)	26.8 ± 0.5	25.1 ± 0.5
$\alpha / \epsilon_{\text{init}}$ (cm/kV)	$0.0234 \pm 4.4 \times 10^{-4}$	$0.0231 \pm 4.6 \times 10^{-4}$

The films on polymer in this work were expected to be free to deform (globally released) and thus function similar to globally released PZT in other reports [2], [18], [29]. In these previous studies, it was shown that when films were free to deflect upon actuation, increased domain reorientation was enabled. Griggio *et al.* showed a greater than 12-fold increase in the alpha coefficient in globally released electrodes [29]. While Yeager *et al.* only measured a 28% increase in alpha of globally released films, it is suggested that the geometry of the released regions played a role in suppressing irreversible domain wall motion [2].

The samples in this study did not behave similarly to previous work on globally released samples. Instead, their behavior was closer to a ferroelectric films which was only locally released. In a locally released structure, such as a taut diaphragm, the substrate is removed from below the electrode but the film is not free to deform. The Rayleigh behavior of locally released electrodes in previous work is summarized in Table 4.4. While Griggio shows an increase in the ϵ_{init} and α , the difference in the ratio of $\alpha/\epsilon_{\text{init}}$ between the clamped and locally released electrodes is not statistically significant [29].

Table 4.4. Rayleigh Parameters Reported in Previous Work

		Clamped	Locally Released
Yeager <i>et al.</i> [2]	ϵ_{init}	1082	1051
	α (cm/kV)	26.06	24.09
	$\alpha/\epsilon_{\text{init}}$ (cm/kV)	0.0241	0.0229
Griggio <i>et al.</i> [29]	ϵ_{init}	1005 ± 0.6	1865 ± 215
	α (cm/kV)	11.7 ± 0.04	20.5 ± 2.5
	$\alpha/\epsilon_{\text{init}}$ (cm/kV)	0.0116 ± 0.0004	0.0110 ± 0.0018

The Rayleigh behavior in this work suggests that these released films act more similarly to locally released structures, where the average stress state of the film has the largest effect on the released properties, not local interface clamping. This is counterintuitive, as the released films presented here should offer no resistance to bending and thus reorient domains fairly easily. Locally released diaphragms, as shown in Chapter 3, are dominated by in plane stress and will not deform much upon actuation. It is possible that the reason these films behave more similarly to locally released structures is associated with the electrical probing used for the measurements. When the probe tip is in contact, it depresses the top electrode to the point of deformation. In other words, the pressure from the probe tip causes the electrode to cup instead of being flat. In this geometry, the film will have a higher stiffness and be more resistant to

bending [30], [31]. Future work on pieces fabricated with contact pads away from the primarily electrode would be helpful in determining whether this plays a major role.

It is difficult to compare the electrical properties of the released films discussed here to other PZT thin films transferred to polymer in literature as there are no other reports which discuss the change (or lack thereof) in Rayleigh behavior and P-E response after release only polymer.

Previous work of BiFeO₃ thin films on polymer showed an increase in P_r and decrease in E_c which is expected upon declamping the ferroelectric. While this was not seen here, this is thought to be due to the change in stiffness induced by the probe tip, discussed above. Future work will focus on reducing the influence of the probe tip to enable more representative measurements.

Bakaul *et al.* demonstrated that transfer of PZT to a polymer via a buffer layer which is sacrificially etched away is possible without microstructural damage (such as cracking) occurring in the PZT [12]. While this was for thin layers of PZT (< 100 nm) [12], PZT films as thick as 700 have been reportedly released without cracking [11]. However, in all of the previous work referenced here, the release process occurred at a much faster rate than the films described in this thesis. Particularly, this is an advantage of the LLO process. Although a laser is needed, the material can be released as fast as the complete interface between PZT and substrate can be vaporized [9]. While release via etching of a sacrificial layer enables deposition on a variety of substrates, one of the disadvantages to the wet etching approaches described in literature is that many of the etchants used to remove sacrificial layers (e.g. solutions containing KOH, phosphoric acid, or HCl) also etch PZT which can lead to a degradation in properties such as remanent polarization [2], [14].

d_{33,f} measurement

While the motivation and design of these films was to measure a $d_{33,f}$ value using a double beam interferometer, it was ultimately unfeasible. An important part of the double beam laser interferometer (DBLI) is having a clear laser signal from both surfaces of the film. Though the backside of the film appeared free of residue and reflective enough for the laser, a low signal provided noisy data. One likely possibility is that the released film is not flat with a probe tip in contact, as mentioned above, and the curvature scatters the laser beam.

4.4 Summary of the Behavior of Films on Polymer

While there is still progress to be made developing the process for the transfer of a PZT film to a polymer substrate, to eliminate cracking, this work presents a promising avenue as well as insight into how the properties of the film change upon release. It was important to correct for changes in imprint associated with asymmetry of the two electrodes. It was found that the film on polymer shows a slight increase in maximum and average remanent polarization values. Drawing parallels to the behavior of PZT thin films deposited on glass, it is likely this results in a better poled sample and a more saturated domain state. As a result, alpha of the released film was about 9% lower than the alpha measured in the clamped film. However it was also demonstrated that the overall stress state in the film is more similar to taut diaphragms which do not show large increases in remanent polarization or alpha. While the ultimate cause of this behavior is still under investigation, it is suggested that it could be the result of the probe tip mechanically bending the electrode prior to measurements.

4.5 References

- [1] Y. Kato, T. Sekitani, Y. Noguchi, T. Yokota, M. Takamiya, T. Sakurai, and T. Someya, "Large-Area Flexible Ultrasonic Imaging System with an Organic Transistor Active Matrix," *IEEE Trans. Electron Devices*, vol. 57, no. 5, pp. 995–1002, 2010.
- [2] C. Yeager, "PZT Thin Films for Piezoelectric MEMS Mechanical Energy Harvesting," Ph. D. Thesis in Materials Science and Engineering, The Pennsylvania Univeristy, 2015.
- [3] T. Someya, T. Sekitani, S. Iba, Y. Kato, H. Kawaguchi, and T. Sakurai, "A Large-Area, Flexible Pressure Sensor Matrix with Organic Field-Effect Transistors for Artificial Skin Applications," *Proc. Natl. Acad. Sci. U. S. A.*, vol. 101, no. 27, pp. 9966–9970, 2004.
- [4] Y. Qi, J. Kim, T. D. Nguyen, B. Lisko, P. K. Purohit, and M. C. McAlpine, "Enhanced Piezoelectricity and Stretchability in Energy Harvesting Devices Fabricated from Buckled PZT Ribbons," *Nano Lett.*, vol. 11, no. 3, pp. 1331–1336, 2011.
- [5] H. Gullapalli, V. S. M. Vemuru, A. Kumar, A. Botello-Mendez, R. Vajtai, M. Terrones, S. Nagarajaiah, and P. M. Ajayan, "Flexible Piezoelectric ZnO-Paper Nanocomposite Strain Sensor," *Small*, vol. 6, no. 15, pp. 1641–1646, 2010.
- [6] H. G. Yeo and S. Trolrier-McKinstry, "{001} Oriented Piezoelectric Films Prepared by Chemical Solution Deposition on Ni Foils," *J. Appl. Phys.*, vol. 116, no. 1, p. 014105, 2014.
- [7] Private communication with Hong Goo Yeo.
- [8] J. Kosel and K. N. Salama, "Thin PZT-Based Ferroelectric Capacitors on Flexible Silicon for Nonvolatile Memory Applications," *Adv. Electron. Mater.*, vol. 1, p. 1500045 1–10, 2015.
- [9] K. I. Park, J. H. Son, G. T. Hwang, C. K. Jeong, J. Ryu, M. Koo, I. Choi, S. H. Lee, M. Byun, Z. L. Wang, and K. J. Lee, "Highly-Efficient, Flexible Piezoelectric PZT Thin Film Nanogenerator on Plastic Substrates," *Adv. Mater.*, vol. 26, no. 16, pp. 2514–2520, 2014.
- [10] W. Lee, O. Kahya, C. T. Toh, B. Özyilmaz, and J.-H. Ahn, "Flexible Graphene–PZT Ferroelectric Nonvolatile Memory," *Nanotechnology*, vol. 24, no. 47, p. 475202, 2013.
- [11] C. H. Lee, S. J. Kim, Y. Oh, M. Y. Kim, Y. J. Yoon, and H. S. Lee, "Use of Laser Lift-Off for Flexible Device Applications," *J. Appl. Phys.*, vol. 108, no. 10, pp. 1–6, 2010.
- [12] S. R. Bakaul, C. R. Serrao, M. Lee, C. W. Yeung, A. Sarker, S.-L. Hsu, A. Yadav, L. Dedon, L. You, A. I. Khan, J. D. Clarkson, C. Hu, R. Ramesh, and S. Salahuddin, "Single Crystal Functional Oxides on Silicon," *Nat. Commun.*, vol. 7, pp. 1–5, 2015.

- [13] H. W. Jang, S. H. Baek, D. Ortiz, C. M. Folkman, C. B. Eom, Y. H. Chu, P. Shafer, R. Ramesh, V. Vaithyanathan, and D. G. Schlom, "Epitaxial (001) BiFeO₃ Membranes with Substantially Reduced Fatigue and Leakage," *Appl. Phys. Lett.*, vol. 92, p. 062910 1–3, 2008.
- [14] B.-Y. Kim, I.-T. Seo, Y.-S. Lee, J.-S. Kim, S. Nahm, C.-Y. Kang, S.-J. Yoon, J.-H. Paik, and Y.-H. Jeong, "High-Performance (Na_{0.5}K_{0.5})NbO₃ Thin Film Piezoelectric Energy Harvester," *J. Am. Ceram. Soc.*, vol. 98, no. 1, pp. 119–124, 2015.
- [15] K.-I. Park, S. Y. Lee, S. Kim, J. Chang, S.-J. L. Kang, and K. J. Lee, "Bendable and Transparent Barium Titanate Capacitors on Plastic Substrates for High Performance Flexible Ferroelectric Devices," *Electrochem. Solid-State Lett.*, vol. 13, p. G57, 2010.
- [16] L. Tsakalakos and T. Sands, "Epitaxial Ferroelectric (Pb, La)(Zr, Ti)O₃ Thin Films on Stainless Steel by Excimer Laser Liftoff," *Appl. Phys. Lett.*, vol. 76, no. 2, p. 227, 2000.
- [17] L. Tsakalakos and T. Sands, "Excimer Laser Liftoff of Epitaxial Pb(Zr,Ti)O₃ Thin Films and Heterostructures," *MRS Proc.*, vol. 596, p. 549, 2011.
- [18] F. Griggio, S. Jesse, A. Kumar, O. Ovchinnikov, H. Kim, T. N. Jackson, D. Damjanovic, S. V. Kalinin, and S. Trolier-McKinstry, "Substrate Clamping Effects on Irreversible Domain Wall Dynamics in Lead Zirconate Titanate Thin Films," *Phys. Rev. Lett.*, vol. 108, no. 15, p. 157604 1–5, 2012.
- [19] M. Wallace, R. L. Johnson-Wilke, G. Esteves, C. M. Fancher, R. H. T. Wilke, J. L. Jones, and S. Trolier-McKinstry, "In Situ Measurement of Increased Ferroelectric/Ferroelastic Domain Wall Motion in Declamped Tetragonal Lead Zirconate Titanate Thin Films," *J. Appl. Phys.*, vol. 117, no. 5, p. 054103, 2015.
- [20] K. Lefki and G. J. M. Dormans, "Measurement of Piezoelectric Coefficients of Ferroelectric Thin Films," *J. Appl. Phys.*, vol. 76, pp. 1764–1767, 1994.
- [21] D. G. Yoo, S. H. Nam, M. H. Kim, S. H. Jeong, H. G. Jee, H. J. Lee, N. E. Lee, B. Y. Hong, Y. J. Kim, D. Jung, and J. H. Boo, "Fabrication of the ZnO Thin Films Using Wet-Chemical Etching Processes on Application for Organic Light Emitting Diode (OLED) Devices," *Surf. Coatings Technol.*, vol. 202, no. 22–23, pp. 5476–5479, 2008.
- [22] D. Zhao, D. A. Mourey, and T. N. Jackson, "Fast Flexible Plastic Substrate ZnO Circuits," *IEEE Electron Device Lett.*, vol. 31, no. 4, pp. 323–325, 2010.
- [23] H. Microsystems, "PI-2600 Series – Low Stress Applications," 2009.
- [24] R. J. Zednik, A. Varatharajan, M. Oliver, N. Valanoor, and P. C. McIntyre, "Mobile Ferroelastic Domain Walls in Nanocrystalline PZT Films: The Direct Piezoelectric Effect," *Adv. Funct. Mater.*, vol. 21, no. 16, pp. 3104–3110, 2011.

- [25] L. M. Garten, "Residual Ferroelectricity, Piezoelectricity, and Flexoelectricity in Barium Strontium Titanate Tunable Dielectrics," Ph. D. Thesis in Materials Science and Engineering, The Pennsylvania State University, 2014.
- [26] J. L. Jones, J. M. Lebeau, J. Nikkel, A. A. Oni, J. H. Dycus, C. Cozzan, F. Lin, A. Chernatynskiy, J. C. Nino, S. B. Sinnott, S. Mhin, G. L. Brennecka, and J. Ihlefeld, "Combined Experimental and Computational Methods Reveal the Evolution of Buried Interfaces during Synthesis of Ferroelectric Thin Films," *Adv. Mater. Interfaces*, vol. 2, p. 1500181 1–10, 2015.
- [27] R. Keech, S. Shetty, K. Wang, and S. Trolier-McKinstry, "Management of Lead Content for Growth of {001}-Oriented Lead Magnesium Niobate - Lead Titanate Thin Films," *J. Am. Ceram. Soc.*, vol. Accepted, 2016.
- [28] P. V. Lambeck and G. H. Jonker, "The Nature of Domain Stabilization in Ferroelectric Perovskites," *J. Phys. Chem. Solids*, vol. 47, no. 5, pp. 453–461, 1986.
- [29] F. Griggio, "Local Piezoelectric Behavior in PZT-Based Thin Films for Ultrasound Transducers," Ph. D. Thesis in Materials Science and Engineering, The Pennsylvania State University, 2011.
- [30] N. S. Trahair, *Flexural-Torsional Buckling of Structures*. USA: CRC Press, 1993.
- [31] G. Leipold, "Tape Measure," Patent EP0009823 A1, 1980.

Chapter 5 – Conclusions and Future Work

5.1 Conclusions

This thesis was directed towards increasing both the understanding of the factors that affect the performance of PZT based MEMS devices, and the functionality of piezoelectric MEMS. This was pursued via two different avenues: integration of ZnO based electronics with PZT actuators and determining the influence of mechanical boundary constraints on PZT film properties.

$\text{Pb}(\text{Zr}_{0.52}\text{Ti}_{0.48})_{0.98}\text{Nb}_{0.02}\text{O}_3$ thin films were deposited on silicon substrates using chemical solution deposition and patterned using RIE into discrete capacitors. ZnO based thin film transistors (TFTs) were then integrated alongside the PZT elements. A procedure to enable co-processing was developed. As the thermal budget of PZT crystallization is higher, the PZT was deposited first. Following this, ZnO TFTs were fabricated using a PEALD process; the dielectric (Al_2O_3) and semiconducting (ZnO) layers were deposited at 200 °C. TFTs deposited alongside or on top of PZT had comparable mobilities (~ 24 cm/Vs) to TFTs deposited on glass. As the precursors for the dielectric and semiconducting materials (trimethylaluminium and diethylzinc) both contain hydrogen which can degrade ferroelectric properties, the PZT was tested before and after integration. It was found that remanent polarization and dielectric constant were unaffected by the co-processing procedure, remaining > 22 $\mu\text{C}/\text{cm}^2$ and 1130 with a loss of $< 3\%$ at 1 kHz, respectively. Additionally, leakage current density before and after TFT processing remained on order of 10^{-8} A/cm² at 3 V_c. Furthermore, charging/discharging studies were performed, using the TFTs to turn on and off the PZT capacitors. The voltage drop over the capacitor was measured using an oscilloscope and it was found that the TFT could be used to

charge the 0.0026 cm^2 capacitor in $< 3 \text{ ms}$ with the PZT capacitor taking longer than 70 seconds to discharge.

This technology was then applied to $\text{Pb}(\text{Zr}_{0.52}\text{Ti}_{0.48})_{0.98}\text{Nb}_{0.01}\text{O}_3$ actuator arrays fabricated on Corning Eagle glass substrates. The PZT was deposited using RF magnetron sputtering at room temperature with a post deposition crystallization anneal in a box furnace in air at $585 \text{ }^\circ\text{C}$ for 18 hours. ZnO based thin film transistors (TFTs) were then integrated into the array in a row-column addressing scheme for an adaptive optics application. While there was some electrical connection between the TFTs, either from a wafer breakage or processing errors, which caused multiple TFTs to respond when only one was actuated, moderate control of the wafer shape was demonstrated. It was found that when actuated at 10 V, a gain of approximately $1.5 \text{ }\mu\text{m}$ above background was achieved in the region of actuation. Additionally, the amount of deflection imposed on the wafer and whether the PZT cell is turned on or off were both shown to be controllable with the ZnO TFT array. The integration of PZT and ZnO electronics is expected to also be applicable to other technologies such as piezoelectric transducer arrays and energy harvesting.

Studies were also performed investigating the effect of mechanical boundary constraints on the reorientation of ferroelastic domains. For these experiments, solution deposited tetragonal $\text{PbZr}_{0.30}\text{Ti}_{0.70}\text{O}_3$ films, doped with 1% Mn, was chosen for *in situ* synchrotron X-ray diffraction. Thicknesses of the films probed ranged from 950 nm to $1.9 \text{ }\mu\text{m}$. As field was applied to the samples, intensity exchanges in symmetry-related peaks were monitored, providing a direct measurement of ferroelastic domain wall motion.

Domain switching was compared for untextured 950 nm thick PZT 30/70 films on Pt-coated Corning Eagle glass and silicon wafers, to assess what effect different substrate elastic

constants might have on domain reorientation. The 101/110 reflections in the film on the more elastically compliant glass showed approximately 3.4 vol% more domain reorientation at 3 V_c than films on Si. Furthermore, the amount of backswitching the films experienced upon release in field scaled with the difference in elastic modulus. Because of the better-saturated domain alignment in films on glass, the irreversible Rayleigh coefficient measured ($\alpha \sim 2$ cm/kV) was smaller than the α of the film on silicon (~ 4.2 cm/kV). Additionally, while the higher {001} texture in the film on silicon predisposed the film to have a higher $e_{31,f}$ than the film on glass, it was found that due to the higher remanence in the film on glass, comparable piezoelectric coefficients between the two films were measured ($e_{31,f}^{glass} \sim -5.9$, $e_{31,f}^{silicon} \sim -5.7$).

In other *in situ* XRD studies investigating the role of the substrate in clamping domain wall motion, the silicon substrate was removed from beneath the LaNiO₃ bottom electrode of the {001} oriented PbZr_{0.30}Ti_{0.70}O₃ with 1% Mn film in an elongated diaphragm geometry. It was found that as the underlying Si was removed, domains have an increased ability to reorient. In films where 75% of the film was not bound to the substrate, more than a six fold increase in domain reorientation was observed relative to fully clamped films. The maximum amount of domain reorientation, approximately 26%, approaches values for bulk ceramics and suggests that piezoelectric coefficients would also be enhanced upon declamping. Furthermore, electrodes with >50% released regions showed smaller amounts of domains backswitching upon release of field.

To better compare these results on elongated diaphragms to other geometries of released electrodes in the literature, circular diaphragms were also investigated. It was found investigating an untextured 1.77 μm thick PZT 30/70 film that the geometry of the released structures played an important role in the amount of domain reorientation observed. The elongated diaphragms

showed increased levels of domain reorientation compared to the circular diaphragms for electrodes both locally released (taut) and globally released (free to deform) from the substrate. In the locally released case, the electrode released via circular diaphragms showed the same amount of domain reorientation in 112/211 reflections as a clamped electrode. In comparison, the electrode released via elongated diaphragms showed twice the amount of domain reorientation compared to the clamped electrode at $1.5 V_c$. This was shown through finite element models to be due to the presence of in-plane stress in the circular diaphragms which was not fully relieved upon the removal of the Si substrate. Due to the larger perimeter of released boundary condition in the elongated diaphragms, this geometry was able to relax more, enabling increased domain reorientation compared to the circular geometry. In globally released films, 3 vol% more domains were reoriented in the *clamped film* compared to the amount of reorientation expressed by the electrode released via circular diaphragms. In contrast, in the electrode released via elongated diaphragms, approximately 20vol% more domains reoriented at $3 V_c$ than in the clamped electrode. This work demonstrates the importance of release geometry, in-plane stress, and its effect on domain reorientation.

Declamping of PZT thin films was further investigated by transferring a CSD deposited $\text{Pb}(\text{Zr}_{0.52}\text{Ti}_{0.48})_{0.98}\text{Nb}_{0.02}\text{O}_3$ film from a silicon substrate, where it was grown, to a polymer substrate. A process was developed to do this using a PEALD deposited ZnO sacrificial etch layer. While the method provided released electrodes, the release process produced cracking in the films, specifically in areas without a top electrode. In spite of this, it was found that the film on polymer showed a slight increase in maximum and average remanent polarization relative to the film on Si. Drawing parallels to the behavior of PZT thin films deposited on glass, it is likely this results in a better poled sample and a more saturated domain state. As a result, the dielectric

irreversible Rayleigh coefficient (α) of the released film was approximately 19 cm/kV, about 9% lower than the α measured in the clamped film, 21 cm/kV. Also, it was found that the overall stress state of the film on polymer seems to be much closer to the circular diaphragm geometry than the more released beam geometry. When unpoled Rayleigh coefficients were probed, there was no increase in the α term for the released film. The reason for this is unknown, although it is possibly related to an increase in the stiffness from the depression of the probe tip on the top electrode. While further work is needed to develop an improved process for the transfer of a PZT film to a polymer substrate, this work presents a promising avenue as well as insight into how the properties of the film change upon release.

5.2 Future Work

5.2.1. *In Situ* X-Ray Diffraction Studies on Elastic Layers

The results presented in the thesis provide quantitative information on domain reorientation for two different substrates, however there are still unanswered questions. While it is clear that the elastic properties of the substrate influence the response of the ferroelectric, a more complete data set on elastic layers should be performed. It is anticipated that such a study could provide insight into the differences reported between the work in this thesis on globally released circular diaphragms and the work of Griggio *et al.* [1] and Yeager *et al.* [2]. Griggio *et al.* showed that globally releasing circular diaphragms resulted in a 114% increase in the irreversible Rayleigh coefficient, α , compared to clamped electrodes [1]. Similarly, Yeager *et al.* showed approximately 40% higher α in globally released films compared to clamped [2]. In contrast, work presented in this thesis showed globally released circular diaphragms showed *less* domain reorientation than clamped electrodes at 3 V_c. One possibility for this disagreement is the difference in thickness in elastic layers between the different works. The 30/70 films investigated

in this thesis had a thicker SiO₂ layer which may play a role in clamping the domain reorientation. It would be useful to have an *in situ* diffraction study, to illuminate the role of an elastic layer. Thus, it is suggested that domain switching should be studied in clamped and released {001} oriented tetragonal PZT thin films with different thicknesses of SiO₂ elastic layers. Samples of clamped and released electrodes would be fabricated with varying thickness of the elastic layer (100 nm to 2 μm). The following questions should be answered:

- 1) Clamped films: Can a thicker elastic layer (with a lower Young's Modulus than Si, such as SiO₂) be used to reduce the effect of the substrate clamping domain wall motion?
- 2) Released films: Does the thickness of the elastic layer in the released section influence domain reorientation, for instance, by changing the stiffness of the released section?

In particular, the elastic layer is expected to perform different functions in released and clamped films. In a clamped film, it is the substrate which resists bending the most. By depositing thicker layers of SiO₂, the clamping due to the stiffness of the substrate is expected to be reduced, enabling greater amounts of domain reorientation. In the released film, it is the elastic layer which resists bending the most. In this context, it is expected that a thicker SiO₂ layer will *decrease* domain reorientation. The films should be released with a XeF₂ etch in an elongated diaphragm geometry used in Chapter 3 in order to be certain of the diaphragm state when globally released. Circular diaphragms are known to break into anywhere from 2-4 different sections. As this affects the ultimate mechanical boundary constraints in film, this geometry should be avoided. In contrast, the elongated diaphragms exclusively break into two sections.

In addition to large signal measurements, *in situ* XRD with cyclic sub-coercive field, or stroboscopic, measurements on these films are recommended, particularly on the released films. Changing the thickness of the elastic layer should change the restoring force for domains to

backswitch upon release in field. If the restoring force is smaller, for example in released films with thin layers of SiO₂, the domains are expected to backswitch to a smaller extent than in films released on thicker layers of SiO₂. This would leave films with thinner SiO₂ layers with a more saturated domain alignment after poling. Films with more saturated domain alignments have been shown in this thesis to be correlated with lower irreversible Rayleigh coefficients. It was hypothesized that this was due to fewer 90° domains available to reorient irreversibly. A direct measurement of the 90° domain wall motion would be useful to have a quantitative measure of how a more saturated domain state effects low field Rayleigh behavior. Beamline 11-ID-C has the capability to apply low voltages (<10 V) at low frequencies (0.1 Hz).

In addition to *in situ* studies, Rayleigh behavior on the released and clamped films should also be performed. This would provide a consistent set of Rayleigh responses which would be especially useful for comparison to the referenced works.

5.2.2. Released Film Process Development

While a process for chemically releasing PZT films onto a polymer substrate has been presented, increased development is still necessary. Additionally, modifying the procedure to eliminate cracking and depression of the electrode upon actuation could enable measurements to provide solid answers for remaining questions.

Film transfer using a sacrificial layer is attractive as it allows a wide range of substrate sizes and materials. However, the method presented in Chapter 4, due to the considerable time the sacrificial etch took, resulted in cracking around the electrodes. As cracks will tend to propagate, it would be useful to develop a procedure in which this does not occur. Additionally, $d_{33,f}$ measurements are needed in released films.

There are several possible ways that the release process can be improved to eliminate the cracking in the brittle PZT film. The first is to keep the film from cracking. In the beginning of the etch, the deformation of the film does not appear as extreme when compared to the end of the etch, as shown in Figure 5.1. If there were more access points to the ZnO, for instance, in tiny holes drilled into the material stack to expose the substrate, the ZnO etch would both be faster and would eliminate the puckering which is the likely cause of cracking. Using RIE, holes could be patterned into the polymer and underlying Pt/PZT/Pt/Al₂O₃ to expose the ZnO.

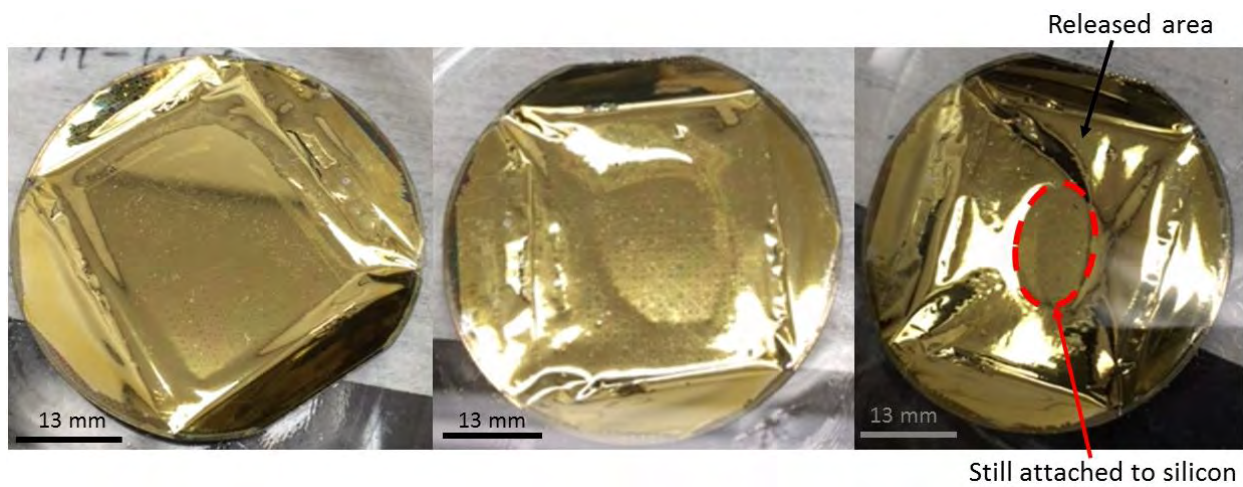


Figure 5.1. Pictures showing the evolution of the film as it is released from the silicon substrate in an acetic acid bath.

If this process still produces cracks, then a vapor etch process should be pursued. In the final stages of the release process, the parts of the film which are already released float in the liquid acid. It is possible that the currents in the acid pull on the released film in a way which exacerbates the deformation. If this is the case, moving completely away from a wet etch process could help. Typically, HF vapor etch processes have been used to release MEMS structures [3]. While HF will attack the PZT, the backside should be protected by the 100 nm of Pt and 5 μ m of polyimide. On the frontside there will be a barrier of conformal PEALD deposited Al₂O₃

between the ZnO and the PZT. The ZnO should etch faster than the Al₂O₃ in HF, however it is possible another buffer layer might be necessary to protect the PZT if this method is employed.

A final option would be to use as exfoliation layer as shown by Shimoda *et al.* [4]. The general idea behind this method is to fabricate the material on an amorphous silicon layer on a transparent substrate. The substrate is then irradiated using a XeCl laser which will crystallize the amorphous silicon, changing the interface between the exfoliation layer and the buffer layer, and enabling separation of the film [4]. A schematic demonstrating the removal process is shown in Figure 5.2 [4]. A similar method was used by Park *et al.* to release a 2 μm thick PZT film onto a 125 μm thick polyethylene terephthalate (PET) substrate [5].

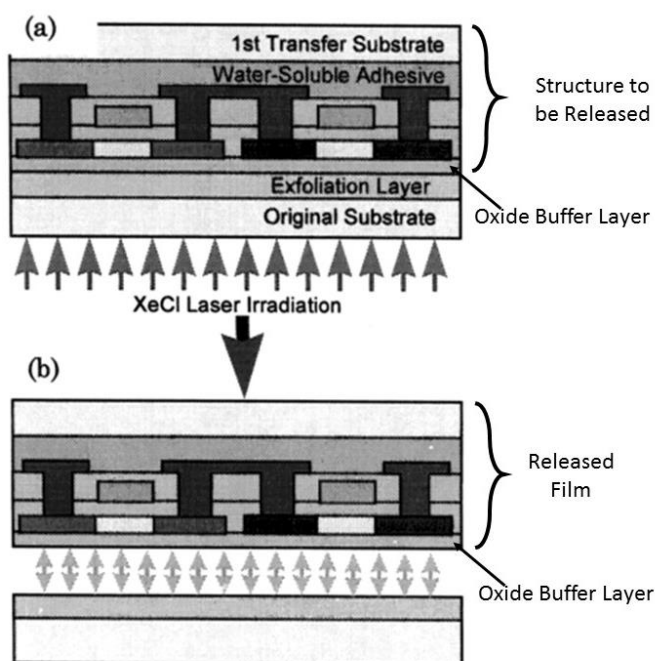


Figure 5.2. Schematic showing the process of releasing a film from its substrate through the use of an exfoliation layer. The exfoliation layer interface is modified with XeCl laser irradiation causing a weaker connection to the substrate.

Once the release process is fully developed, a $d_{33,f}$ measurement should be taken. To eliminate beam scattering from an indentation of the probe tip, leads from the electrode to a contact pad on the side should be integrated into the design. Additionally, by integrating leads, measurement on flat capacitors can be made. This would also allow the hypothesis on probe-induced deflections limiting domain wall motion to be assessed.

Additionally, once the process is perfected, it would be interesting to take an *in situ* measurement of domain reorientation on a polymer substrate. For this study, $\text{Pb}(\text{Zr}_{0.30}\text{Ti}_{0.70})\text{O}_3$ is necessary as the beamline at 11-ID-C is not able to resolve the independent peaks in the MPB composition. It would be interesting to compare the domain reorientation measured in a sample with essentially no substrate with the results from the studies of films on glass and silicon, described in Chapter 3.

5.2.3. Integrating TFTs onto PZT on Curved Substrates

Proof of concept experiments for control of X-ray optics with integrated ZnO electronics and a piezoelectric layer were performed on flat glass wafers. Ultimately, the TFT array must be integrated with the conical mirror pieces. This presents a challenge as contact mask aligners do not have a large enough field of view to enable precision in feature size on a curved substrate with the radii of curvature required [6]. Fabricating TFTs on a flat, flexible substrate (such as polyimide) would allow for the micron feature size lithography steps to be done with conventional contact lithography. As the pixels for TFT control are large ($\sim 1 \text{ cm}^2$), the alignment of the flexible TFTs to the substrate could be done by eye and metal contacts on either side could be bonded using one of several different kinds of bonds. Gold diffusion bonding, anisotropic conductive film (ACF), tape automated bonding (TAB) and wire bonding should be investigated

to determine which is most suitable in conjunction with the glass mirrors. Stress from the bonding must not induce cracking or excessive mirror deformation.

It will be important to choose the bonding method which imparts the smallest (both in magnitude and area) deformation on the glass substrate/mirror. A Shack-Hartmann wave-front sensor (WFS) should be used to assess the changes to the mirror shape due to the different bonding methods. Flat glass wafers should be prepared for bonding by deposition of metal and insulating bonding layers. The specific materials and methods are discussed below. A baseline shape for the wafer will be measured using the WFS. This characterization method requires that the wafer be bonded to a holder which positions the wafer. The wafer cannot be removed from the holder after the initial measurement, so a support will be needed for the subsequent bonding. Several bonding methods (tape automated, anisotropic conductive film and gold diffusion) should be performed individually on previously measured glass wafers. The effect of the bonding on the mirror profile would then be quantified using the WFS and compared to the initial measurement.

After identifying the best bonding method, a transition to curved substrates should be investigated. This will be a key engineering challenge. It will be necessary to develop a method which allows the pressures from the bonding to be uniformly distributed across the mirror without damaging the glass. In an attempt to provide sufficient support to the curved glass piece, a mandrel used for slumping the glass could be used.

Au Diffusion Bond

Au diffusion bonding, sometimes referred to as cold welding, has been demonstrated to be achievable at small loads and ambient temperatures on compliant elastomers, making this method of bonding a good choice for bonding a flexible substrate of TFTs onto a curved

substrate [7]–[9]. The elastomeric stamp allows for a thousand fold decrease in the pressures needed to achieve a gold-gold bond due to the ability to conform the two surfaces to each other [8]. Ferguson *et al.* demonstrated gold-gold bonding with low electrical resistance ($< 0.4 \Omega/\text{cm}^2$) between thin gold films deposited on PDMS at small loads ($< 0.1\text{--}0.2 \text{ g}/\text{cm}^2$). This study supports the claim that elastic substrates allow the Au layers to conform to each other which will increase the Au-Au surface contact area, facilitating bonding [7]. Kim *et al.* using a similar process (with one elastomeric substrate) demonstrated an Au-Au bond on a glass substrate at a pressure of approximately 500 g over a contact area of 0.28 cm^2 . The low pressures needed allow for bonding on a brittle substrate [8]. Diffusion bonds have also been demonstrated to be appropriate for arrays [9].

Preliminary tests have been conducted to determine the feasibility of Au diffusion bonds with the materials in question for this study. Au coated polyimide was placed in contact with a piece of Au coated glass. The samples were placed in a platen press heated to $100 \text{ }^\circ\text{C}$ for two minutes while a pressure of 2100 psi was applied. The bond was electrically conductive (2Ω measured via a multimeter) and so demonstrated a successful diffusion bond at low pressures. However, further testing is required to determine the durability of the bonds and the stress induced by this bonding process. It is anticipated that a mandrel will be used to keep the curved substrate in compression.

Anisotropic Conductive Film (ACF)

Anisotropic conductive film (ACF) is another bonding option to electrically connect the TFT array to the PZT pixels. ACF bonding is widely used in flip-chip and display technologies due to the high reliability and low cost of the ACF bonds. A typical ACF bond is achieved by placing an ACF adhesive between a flexible (flex cable) and a rigid substrate (the sample). A

cycle of heating and cooling is applied under pressure, resulting in a connection where the electrical conductivity is limited to the z-direction.

Anisotropic conductive film generally is composed of a matrix of epoxy containing conductive particles. The particles typically have a polymer core coated with nickel-gold and a very thin polymer insulating coating. Where heat and pressure are applied, the epoxy flows, enabling the contacts to be pushed away from the thin polymer coating, allowing the flow of electricity vertically. The epoxy hardens upon cooling, which holds the spheres in their conducting state [10]. ACF bonding has already been demonstrated to be compatible with the materials in question. It is currently used to make electrical connection between the control electronics and the monolithically fabricated TFT array. What is not known is whether this deforms the glass locally.

Tape Automated Bonding (TAB)/Wirebonding

TAB bonding was created as an alternative to wire bonding and has been reported for integration of liquid crystal display driver circuits. It is suggested that in order to assess the viability of this method for the X-ray optics application, a gold bump could be electroplated onto the surface of the glass substrate. This would be connected directly to leads attached to the PZT. The idea is similar to the diffusion bond, however this method incorporates some ultrasonic excitation which helps the bond to form at lower pressures. Z. Preiskorn at PSU calculated that a 150 °C bonding temperature and local pressure of 70 N/mm² will be suitable for the bond.

5.3 References

- [1] F. Griggio, S. Jesse, A. Kumar, O. Ovchinnikov, H. Kim, T. N. Jackson, D. Damjanovic, S. V. Kalinin, and S. Troler-McKinstry, "Substrate Clamping Effects on Irreversible Domain Wall Dynamics in Lead Zirconate Titanate Thin Films," *Phys. Rev. Lett.*, vol. 108, no. 15, p. 157604 1–5, 2012.
- [2] C. Yeager, "PZT Thin Films for Piezoelectric MEMS Mechanical Energy Harvesting," Ph.D. thesis in Materials Science and Engineering, The Pennsylvania State University 2015.
- [3] Y. I. Lee, K. H. Park, J. Lee, C. S. Lee, H. J. Yoo, C. J. Kim, and Y. S. Yoon, "Dry Release for Surface Micromachining with HF Vapor-phase Etching," *J. Microelectromechanical Syst.*, vol. 6, no. 3, pp. 226–233, 1997.
- [4] T. Shimoda, S. Inoue, and S. Utsunomiya, "Polysilicon TFT on Plastics," *SPIE Flat Panel Disp. Technol. Disp. Metrol. II*, vol. 4295, pp. 52–59, 2001.
- [5] K. Il Park, J. H. Son, G. T. Hwang, C. K. Jeong, J. Ryu, M. Koo, I. Choi, S. H. Lee, M. Byun, Z. L. Wang, and K. J. Lee, "Highly-Efficient, Flexible Piezoelectric PZT Thin Film Nanogenerator on Plastic Substrates," *Adv. Mater.*, vol. 26, no. 16, pp. 2514–2520, 2014.
- [6] D. Radtke, M. Stumpf, and U. D. Zeitner, "Advances in Lithography on Non-Planar Surfaces," *Proc. SPIE*, vol. 7716, no. 0, p. 77160Z–77160Z–9, 2010.
- [7] G. S. Ferguson, M. K. Chaudhury, G. B. Sigal, and G. M. Whitesides, "Contact Adhesion of Thin Gold Films of Elastomeric Supports: Cold Welding Under Ambient Conditions," *Science*, vol. 253, no. 5021, pp. 776–778, 1991.
- [8] C. Kim and S. R. Forrest, "Fabrication of Organic Light-Emitting Devices by Low-Pressure Cold Welding," *Adv. Mater.*, vol. 15, no. 6, pp. 541–545, 2003.
- [9] C. Kim, P. E. Burrows, and S. R. Forrest, "Micropatterning of Organic Electronic Devices by Cold-Welding," *Science*, vol. 288, no. 5467, pp. 831–833, 2000.
- [10] M. J. Yim, C. K. Chung, and K. W. Paik, "Effect of Conductive Particle Properties on the Reliability of Anisotropic Conductive Film for Chip-on-Glass Applications," *IEEE Trans. Electron. Packag. Manuf.*, vol. 30, no. 4, pp. 306–312, 2007.

Appendix – Photoresist recipes

Table A.1 Shipley SPR 955 2.1

Photoresist Recipe: Shipley SPR 955 2.1	
Wafer Preparation	Bake the wafer at ~105 °C to remove excess water from the surface
Spin Photoresist	Each Layer: 2000 rpm for 45 seconds *Spin speed was optimized to produce a coating that was both thick (~3 μm) and uniform
Bake steps sequence	Layer 1: 105 °C for 10 minutes Layer 2: 105 °C for 5 minutes Layer 3: 105 °C for 5 minutes Layer 4: 105 °C for 2 minutes
Exposure Sequence	10 s exposure, 30 s wait, repeated 5 times at 8 mW/cm ²
Develop	CD-26 for 3-4 minutes * Once the wafer is removed from the developer, rinsed, and dried, the resist will not develop further

Shipley SPR 955 2.1 photoresist was used as a mask for features to be etched with RIE. The sequence below is for a resist stack that was typically 12 μm thick in total. For applications which do not require such thick resists, the number of layers can be modified. A spin speed of 2000 rpm was found to be the lower limit in producing uniform layers of resist. Additionally, longer initial soft-bake times and multiple exposures with wait times were both employed to reduce bubbles that might be introduced due to nitrogen outgassing during the exposure step. After exposure, it is critical to keep the sample in the developer until the pattern has finished developing. Otherwise, once rinsed and dried, the resist will no longer develop. With very small features and such thick resist, develop times of different sized structures can vary. Because of this, often large area alignment marks were used to gauge when the develop was almost finished, keeping the wafer submerged for ~ 30 seconds after these larger features are finished developing.

Table A.2 Shipley SPR 3012

Photoresist Recipe: Shipley SPR 3012	
Wafer Preparation	For double layer lithography, spin LOR 5A first
Spin Photoresist	Using dynamic dispensing, apply photoresist and spin at 4000 rpm for 45 seconds
Soft-bake	95 °C for 1 minute
Exposure	7 seconds at 8 mW/cm ² (Hard Contact)
Develop	CD-26 for 1 minute, single layer CD-26 for 2 minutes, double layer

Shipley 3012 was used primarily as the patterned resist for double layer lithography or for some steps where only one layer of resist was needed and sample sensitivity to developer was not an issue.

Table A.3 LOR 5A

Photoresist Recipe: LOR 5A	
Wafer Preparation	Remove particulates using nitrogen air gun
Spin Photoresist	Using dynamic dispensing, apply photoresist and spin at 4000 rpm for 45 seconds
Soft-bake	180 °C for 2 minutes
Exposure	
Develop	CD-26

LOR5A is used as a lift off resist for double layer lithography where the sample is not sensitive to tetramethylammonium hydroxide (TMAH), the active component in CD-26 developer.

Table A.4 Microposit S1813

Photoresist Recipe: Microposit S1813	
Wafer Preparation	Remove particulates using nitrogen air gun
Spin Photoresist	Using dynamic dispensing, apply photoresist and spin at 4000 rpm for 45 seconds
Soft-bake	Bake at 105 °C for 90 seconds
Exposure	4 second exposure
Develop	Water and 351 (ratio: 3:1, water:351) for 1 minute

S1813 photoresist was used for patterning of ZnO and Al₂O₃ and for electrodes deposited on these materials. Both ZnO and Al₂O₃ are sensitive to the TMAH in CD-26 developer and will etch

away in its presence. Neither material is volatile in 351 so a dilute solution is prepared for developing on these materials.

Table A.5 Double layer lithography with PMMA 950 A3

Photoresist Recipe: Double layer lithography with PMMA 950 A3	
Wafer Preparation	Remove particulates using nitrogen air gun
Spin Photoresist	Using dynamic dispensing, apply photoresist and spin at 4000 rpm for 45 seconds 1 st – PMMA 2 nd – 1811 (diluted version of 1813 provided by the Jackson Lab)
Soft-bake	PMMA – 180 °C, 10 minutes 1811 – 90 °C, 1 minute
Exposure	2 second exposure
Develop	1811 – 4:1 water:351, ~45 seconds Oxygen plasma etch of intermix layer that forms between 1811 and PMMA for 4 minutes Expose PMMA to UV light source for 3 minutes flowing nitrogen Develop PMMA in toluene squirt bottle for 1 minute. Important to continually refresh the toluene on the surface

This double layer lithography is used for the source and drain contacts for TFTs since a reactive developer is not needed for these resists. If the PMMA is exposed in air, it is likely that ozone will be created, reacting with the PMMA, and resulting in non-uniform development of the resist.

Inhibition Layer Lift off Profile

Depositing thin, uniform layers of photoresist using conventional spin processes is complicated on curved substrates. As such, a USI Prism 300 spray coater was investigated to deposit a single layer resist with a lift off profile. Initial experiments were conducted on flat pieces although it is expected that the process should translate to curved pieces as well.

It was found that typical resists for double layer lithography (PMMA or LOR) were not easily compatible with the spray coater. Instead, to create the proper photoresist profile, a

technique is used where exposure to the developer, CD-26, creates an inhibition layer at the surface of the photoresist. This layer has lower solubility in the developer and so upon development, an overhang exists [1].

The general process is to spray coat 2 microns of AZ4999 and let sit 30 minutes. Then, dip the wafer in CD-26 (TMAH) for 40 seconds. Soft bake at 105 °C for 90 seconds, expose for 10 seconds and develop for 75 seconds. Figure 3.5.2 shows a FESEM micrograph example of the photoresist profile from this process. One important note about this process is that the heating profile is important in achieving the correct shape of the resist.

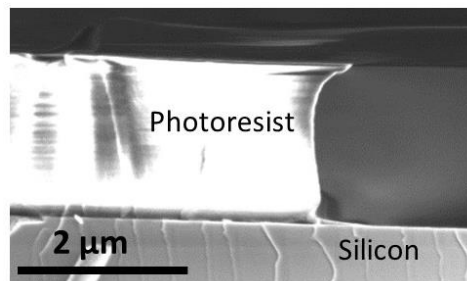


Figure A.1. The photoresist profile of AZ4999 when developed using a surface inhibition layer.

- [1] R. Redd, D. Maurer, and L. S. Klingbeil, “Revitalization of Single Layer Lift-Off for Finer Resolution and Challenging Topography,” in *2001 GaAs MANTECH Conference. Digest of Papers*, 2001, pp. 99–101.

VITA
Margeaux Wallace

Margeaux was born and raised in New Jersey. From there she went to Cornell University to study Materials Science and Engineering and frequently break into song with her choir or a cappella group. After graduating with her bachelor of science in 2011, Margeaux went straight to graduate school at Penn State, advised by Prof. Susan Troler-McKinstry. Interestingly, Penn State, Cornell and her parents' home in New Jersey form an equilateral triangle of 3.5 hour drives. Aside from research, Margeaux enjoys walking her two cats, singing, and board games. Upon graduation she will start work at GE Global Research in upstate NY.